Politecnico di Bari

Repository Istituzionale dei Prodotti della Ricerca del Politecnico di Bari

Design of a drift chamber with radiation-hard composite materials for high energy physics and aerospace applications

This is a PhD Thesis

Original Citation:
Design of a drift chamber with radiation-hard composite materials for high energy physics and aerospace applications / Procacci, Francesco Massimiliano. - ELETTRONICO. - (2026).

Availability:
This version is available at http://hdl.handle.net/11589/300660 since: 2026-05-05

Published version
DOI:

Publisher: Politecnico di Bari

Terms of use:

(Article begins on next page)

14 May 2026

Politecnico
di Bari

Department of Mechanics, Mathematics and Management
MECHANICAL AND MANAGEMENT ENGINEERING
Engineering and Aerospace Science Ph.D. Program

SSD: FIS/01 - Experimental Physics
ING-IND/14 – Advanced Mechanical Design

Final Dissertation

Design of a Drift Chamber with Radiation-Hard Composite Materials for High Energy Physics and Aerospace Applications

---

by

Francesco Massimiliano Procacci

Supervisors:
Prof. Marcello Abbrescia
Prof.ssa Claudia Barile
Ch.ma Prof.ssa Caterina Casavola
Prof. Nicola De Filippis
Prof. Giovanni Pappalettera

Coordinator of Ph.D. Program:
Ch.ma Prof.ssa Caterina Ciminelli

Course n° 38, 01/11/2022–31/10/2025

Politecnico di Bari

Department of Mechanics, Mathematics and Management
MECHANICAL AND MANAGEMENT ENGINEERING
Engineering and Aerospace Science Ph.D. Program
SSD: ING-IND/14 – Advanced Mechanical Design

Final Dissertation

Design of a Drift Chamber with Radiation-Hard Composite Materials for High Energy Physics and Aerospace Applications

by

Francesco Massimiliano Procacci

Referees:
Prof. Giuseppe Lacidogna
Prof. Fabrizio Palla

Supervisors:
Prof. Marcello Abbrescia

Prof.ssa Claudia Barile

Ch.ma Prof.ssa Caterina Casavola

Prof. Nicola De Filippis

Prof. Giovanni Pappalettera

Coordinator of Ph.D. Program:
Ch.ma Prof.ssa Caterina Ciminelli

Course n° 38, 01/11/2022–31/10/2025

Contents

1 Challenges for an experiment at the future circular collider 1
1.1 FCC-ee and CEPC: two ideas, similar purposes . . . 2
1.1.1 The FCC-ee collider overview . . . 3
1.1.2 The case of CEPC: comparison and implications . . . 4
1.2 An experiment for future colliders: the IDEA detector . . . 6
1.2.1 Machine–detector interface and beam pipe . . . 8
1.2.2 Vertex detector (VTX). . . . 8
1.2.3 Silicon wrapper and timing layers . . . 8
1.2.4 Magnet system . . . 9
1.2.5 Electromagnetic calorimeter (ECAL) . . . 9
1.2.6 Hadronic calorimeter (HCAL) . . . 9
1.2.7 Muon system . . . 9
1.2.8 A promising experiment for FCC-ee . . . 10
1.3 Operating principle of the drift chamber . . . 11
1.3.1 Particles through matter . . . 11
1.3.2 Electromagnetic interactions and energy loss . . . 11
1.3.3 Main principles of a gas detectors . . . 12
1.3.4 Electron and ions mobility . . . 13
1.3.5 The avalanche multiplication and gas choice . . . 14
1.4 From Multi-wire proportional chambers to drift chamber . . . 15
1.4.1 Drift chamber detector . . . 16
1.5 Scope of the thesis and original contributions . . . 17

2 The IDEA experiment core: the INTREPID drift chamber 19
2.1 Proposal for a new drift chamber . . . 19
2.2 Layout of the INTREPID drift chamber . . . 20
2.3 The INTREPID wire scheme . . . 21
2.3.1 Drift cell configuration . . . 23
2.4 INTREPID Gas mixture choice . . . 23
2.5 Design challenges for the INTREPID drift chamber . . . 25
2.5.1 Momentum and angular resolutions . . . 25
2.5.2 Wire-tension constraints . . . 27
2.5.3 Wire positioning . . . 27
2.5.4 Load constraints . . . 28
2.5.5 Material budget . . . 28
2.6 Mechanical constraints study plan . . . 29

3 Mechanical design of the INTREPID drift chamber 33
3.1 Global mechanical architecture and design requirements . . . 33
3.1.1 Design requirements and acceptance criteria . . . 34
3.2 Mechanical design workflow . . . 35
3.3 3D CAD modeling: INTREPID full chamber . . . 36
3.3.1 Full-length prototype . . . 38
3.4 Mechanical Design and Finite Element Analyses of the INTREPID Drift Chamber Endplate . . . 39
3.4.1 Preliminary design and modelling . . . 40
3.4.2 Advanced cross-section design (manufacturing convergence) . . . 43
3.4.3 Conclusions . . . 51

4 The CEPC drift chamber 53
4.1 An alternative drift chamber proposal . . . 53
4.2 The Drift Chamber for CEPC . . . 55
4.3 The drift chamber for CEPC: mechanical design . . . 56
4.3.1 Overall design . . . 57
4.3.2 Wire tension . . . 57
4.3.3 Finite Element Analysis . . . 59
4.4 Endplate optimization . . . 59
4.4.1 Thickness optimization . . . 61
4.4.2 New version of the endcap . . . 63
4.4.3 Ongoing R&D on primary ionization counting in the CEPC framework . . . 65
4.5 Next developments . . . 66

5 Mechanical Characterization of Ultra-Thin Wires for Drift Chambers 69
5.1 Introduction . . . 69
5.2 Mechanical Model . . . 70
5.2.1 Stress–strain definitions . . . 70
5.2.2 Mechanical properties extracted from the tensile curve . . . 71
5.2.3 Tension and sagitta constraint . . . 71
5.3 Experimental Setup . . . 71
5.3.1 Specimen preparation (tabbing) . . . 72
5.3.2 Loading system and alignment . . . 72
5.3.3 Data processing and property extraction . . . 73
5.4 Results . . . 74
5.4.1 Rate-study and choice of the test velocity . . . 74
5.4.2 Stress–strain response and extracted properties . . . 75
5.4.3 Carbon monofilament as a low-mass field-wire candidate . . . 76
5.5 Limitations of the tensile-test campaign . . . 77
5.6 Conclusions . . . 77

6 Non-destructive Evaluation of UV-Induced Damage in Fiber-Reinforced Benzoxazine Composites **79**
6.1 Acoustic-based methods for damage detection . . . 80
6.2 Experimental campaign . . . 80
6.3 Pencil Lead Break test . . . 82
6.3.1 PLB AEwin features . . . 82
6.3.2 PLB Waveform-processing strategy . . . 84
6.3.3 PLB test results . . . 86
6.3.4 Conclusion of PLB test . . . 90
6.4 Acousto-Ultrasonic test . . . 91
6.4.1 AU AEwin features . . . 92
6.4.2 AU Waveform-processing strategy . . . 94
6.4.3 Conclusion of AU test . . . 95
6.5 Limitations and interpretation of the UV-ageing study . . . 97
6.6 Summary . . . 97

7 Cluster Counting for Particle Identification: A Key Feature of the INTREPID Drift Chamber **99**
7.1 From $\mathrm{d}E/\mathrm{d}x$ to $\mathrm{d}N/\mathrm{d}x$: the cluster-counting technique . . . 100
7.1.1 Analytical expectations for particle identification . . . 102
7.2 Beam-test campaign for the experimental validation of cluster counting 102
7.2.1 Beam-test campaign and scan strategy . . . 104
7.2.2 Preparation, commissioning, and operation of the beam-test setup . . . 105
7.2.3 Experimental setup and readout system . . . 107
7.2.4 Signal conditioning and gas-gain calibration . . . 108
7.2.5 Peak-finding algorithms and clusterization . . . 109
7.2.6 Dependence on operating parameters . . . 110
7.2.7 Comparison between $\mathrm{d}E/\mathrm{d}x$ and $\mathrm{d}N/\mathrm{d}x$ . . . 111
7.2.8 Resolution improvements: waveform cleaning and time-dependent corrections . . . 113
7.3 Implications for the INTREPID drift chamber . . . 113

A Detailed Acoustic and Acousto-Ultrasonic Data **121**

List of Figures

1.1 Target instantaneous luminosity as a function of the center-of-mass energy for the main proposed future e^+e^- colliders. Circular machines such as FCC-ee and CEPC provide very high luminosity at the Z, WW and Higgs operating points, defining the rate and precision environment that drives the detector-performance requirements discussed in this chapter. 3

1.2 Schematic layouts of the two circular lepton-collider infrastructures considered in this thesis: FCC-ee at CERN (left) and CEPC in China (right). Both machines are designed as high-luminosity e^+e^- factories, but their different tunnel dimensions, machine parameters and implementation choices lead to different detector boundary conditions. 5

1.3 Full IDEA detector concept for a future circular e^+e^- collider. The figure shows the nested detector architecture, from the innermost vertex detector and central drift chamber to the calorimeters, solenoid, return yoke and muon system. The large-volume drift chamber is the central tracking element addressed in this thesis. 6

1.4 Cross-sectional view of the IDEA detector layout, showing the relative position of the vertex detector, central drift chamber, silicon wrapper, solenoid, calorimeters and muon system. The figure highlights the radial envelope available for the ultra-light drift chamber and its integration with the surrounding detector subsystems. 7

1.5 Mass stopping power for positive muons in copper as a function of $\beta\gamma$. The curve illustrates the minimum-ionizing region, the relativistic rise and the approach to the Fermi plateau, which provide the physical basis for ionization-based particle identification in tracking detectors. 13

1.6 Schematic layout of a multi-wire proportional chamber (MWPC). Parallel anode wires are placed between cathode electrodes; ionization electrons drift toward the high-field region around the anodes, where avalanche multiplication produces detectable signals. 15

1.7 Schematic representation of a drift-chamber wire layer. Alternating anode and field wires define the drift cells and shape the electric field, allowing the charged-particle position to be reconstructed from the electron drift time to the nearest anode wire. 16

1.8 Single drift-cell geometry illustrating the conversion of drift time into a distance from the sense wire. The calibrated time-to-distance relation depends on the gas mixture, electric and magnetic fields, pressure, temperature and local cell geometry. 17

2.1 Schematic three-dimensional view of the INTREPID drift chamber concept. The detector consists of a large cylindrical wire volume closed by two endplates and supported by a low-mass mechanical structure designed to minimize material while preserving wire-position stability. 21

2.2 Mechanical concept of the INTREPID endplate. Left: wire-bearing PCB stacks alternated with spacers and inserted between adjacent radial spokes, following the feed-through-less construction approach developed for MEG II. Right: stay-based wire-tension recovery scheme, in which the radial spokes are supported by tensioned stays that redirect the cumulative wire load toward the outer support structure. . . 22

2.3 Geometrical definition of the stereo-wire configuration. The two wire ends are attached to azimuthally shifted sectors on opposite endplates, producing a stereo angle ϵ_i and a hyperboloidal wire envelope. The difference between the endplate radius r_i and the central radius r_{i0} determines the radial evolution of the wire position along z. 22

2.4 Projected wire distribution for the stereo layout near the inner chamber radius (left) and near the outer chamber radius (right). The changing apparent wire density reflects the hyperboloidal geometry generated by the full-stereo configuration. 23

2.5 Stereo-cell organization of the INTREPID drift chamber. Left: schematic view of one super-layer with alternating wire layers. Right: arrangement of drift cells with positive and negative stereo angles, defining the U and V projective views required for three-dimensional track reconstruction. 24

2.6 Summary of the main INTREPID drift-chamber layout parameters, including radial dimensions, active length, number of layers, number of sectors, cell-size range and wire configuration. These values define the baseline geometry used in the mechanical and detector-performance studies. 24

2.7 Complete MEG II drift-chamber wire cage. The visible twist of the wire layers illustrates the stereo geometry that inspired the feed-through-less wiring and full-stereo design strategy adopted for the INTREPID drift chamber. 24

2.8 Conceptual transverse cross-section of the drift chamber in a solenoidal magnetic field B_0. The effective lever arm L_0 and the number of measured space points determine the measurement contribution to the transverse-momentum resolution, while the material budget controls the multiple-scattering term. 26

2.9 Material-budget breakdown of the drift-chamber concept, expressed in fractions of radiation length X_0. The barrel contribution is dominated by gas, wires and thin walls, while the forward region includes additional contributions from wire supports, endplate structures, front-end electronics, cables and services. 29

3.1 Full three-dimensional CAD model of the INTREPID drift chamber used to define the global mechanical architecture, integration envelopes and interfaces for finite-element modelling. The model includes the endcaps, radial spokes, support rings, representative PCB volumes, stay-routing regions and segmented barrel structure. 36

3.2 CAD details of the spoke-to-ring interfaces. The spoke includes dedicated inserts and mating features for connection to the inner and outer support rings, providing the reference geometry for subsequent endplate assembly. 37

3.3 CAD details of the endplate integration region, showing PCB stacks, spacers, gas-distribution openings and stay-routing features. These elements define the local mechanical interfaces that must simultaneously provide wire positioning, gas distribution and structural load transfer. 37

3.4 CAD representation of the stay anchoring concept at the outer ring. The adjustable stay connection enables controlled tension recovery and provides the mechanical path through which the cumulative wire load is redirected from the radial spokes to the external support structure. 38

3.5 CAD concept of the proposed full-length prototype with reduced azimuthal coverage. The prototype preserves the full chamber length while instrumenting a limited number of sectors, allowing wiring, electrostatic stability, gas distribution, mechanical integration and readout concepts to be validated under realistic longitudinal conditions. . 38

3.6 Finite-element modelling workflow adopted in ANSYS Workbench with Composite PrepPost (ACP). The workflow links composite lay-up definition, mesh generation, structural analysis and post-processing of deformation, stress and composite failure indices. 40

3.7 Finite-element mesh of the preliminary endplate model. Left: full endplate mesh including rings, spokes and stay geometry. Right: mesh detail of a representative spoke, where the composite lay-up is discretized through the thickness to improve the accuracy of stress and deformation predictions. 41

3.8 Concept-level load and pretension modelling adopted in the preliminary endplate FEM analysis. Top: radially varying equivalent pressure applied to the spokes to represent the distributed wire-tension load. Bottom: thermal contraction applied to the stays to simulate pretension and evaluate its effect on endplate deformation. 42

3.9 Preliminary full-endplate FEM results without stay pretension. From top to bottom: directional deformation along the chamber axis, directional stress along the spoke axis, and inverse reserve factor evaluated with the adopted Maximum Stress/Strain criterion. The large axial deformation identifies the need for an active tension-recovery strategy. 44

3.10 Preliminary full-endplate FEM results with stay pretension introduced through thermal contraction. From top to bottom: axial directional deformation, spoke-axis directional stress and inverse reserve factor. The comparison with the non-pretensioned case shows the ability of the stay system to reduce deformation and homogenize the stress distribution. 45

3.11 Refined double-T spoke concept developed for improved stiffness and manufacturability. Top: cross-section and composite ply distribution, including the central carbon–epoxy core, skin plies and additional unidirectional flange reinforcement. Bottom: interlocking-mold concept proposed for manufacturing and dimensional control of the composite spoke. 46

3.12 Refined single-spoke finite-element model. Top: spoke model with attached portions of the inner and outer rings and bonded composite interfaces. Bottom: updated radially varying pressure distribution applied to the spoke to reproduce the equivalent integrated wire load in the refined design stage. 48

3.13 Directional axial deformation of the refined single-spoke FEM model under the equivalent wire load. Top: configuration without stays, used as a limiting compliance case rather than as a realistic detector option. Bottom: configuration with 15 tension-recovery stays, showing the reduction of the maximum axial deformation to approximately 0.19 mm. 49

4.1 Reference mechanical concept of the CEPC drift chamber. The detector consists of a carbon-fiber barrel structure closed by two aluminum endcaps with a stepped profile and a regular hole pattern for wire installation and tensioning. 54

4.2 Conceptual layout of the CEPC detector, showing the main tracking and calorimeter subsystems. The drift chamber is integrated within the tracking system to enhance charged-particle identification through ionization and cluster-counting measurements. 56

4.3 Carbon-fiber material configuration adopted for the CEPC drift-chamber barrel support. The figure illustrates the layered composite structure and the main material parameters used to define the mechanical model of the cylindrical frame. 57

4.4 CEPC drift-chamber barrel structure and composite lay-up detail. The barrel is composed of longitudinal and annular carbon-fiber beams together with thin inner and outer carbon-fiber cylinders, providing a lightweight support for the large wire volume. 58

4.5 Quarter-section profile of the CEPC drift chamber with main geometrical dimensions. The drawing shows the barrel envelope, stepped aluminum endcap, central opening and radial regions used for wire anchoring and mechanical optimization. 58

4.6 Finite Element Analysis results for the mechanical structure under wire tension and self-weight: (a) von Mises stress distribution in the endplates, (b) total displacement magnitude of the endplates, (c) von Mises stress distribution in the carbon-fiber support frame, and (d) axial displacement (U_3) of the carbon-fiber frame. The results show moderate stress levels and limited deformations, confirming the mechanical stability of the overall assembly. 60

4.7 Baseline stepped endcap geometry used for the CEPC thickness-optimization study. The views show the overall aluminum endcap design and the detailed stepped profile, which determines both the mechanical stiffness and the available wire-routing area. 61

4.8 Static FEM results for the CEPC stepped aluminum endcap with a thickness of 20 mm. Top: equivalent elastic-strain distribution. Bottom: equivalent von Mises stress distribution. The results are used to assess the mechanical response of the reference geometry under the equivalent wire-tension load. 62

4.9 Dependence of maximum equivalent elastic strain and maximum von Mises stress on CEPC endcap thickness. Both quantities decrease strongly between 15 and 20 mm, while further thickness increases provide only marginal improvement, indicating a diminishing-return regime. 63

4.10 Proposed concave CEPC endcap geometry. The design replaces the stepped profile with a continuous surface in order to improve active-area coverage and redistribute stiffness more efficiently while maintaining compatibility with the global endcap envelope. 64

4.11 Static FEM results for the proposed concave CEPC endcap with a uniform thickness of 15 mm. The equivalent elastic strain and von Mises stress fields indicate improved global stiffness and lower stress levels with respect to the stepped geometry of the same thickness, within the assumptions of the simplified model. 64

4.12 Multilayer drift-chamber prototype developed within the CEPC primary-ionization-counting R&D programme. Top: mechanical layout of the reduced-scale prototype. Bottom: wire scheme of the first two layers, showing the arrangement of sense wires and field wires used to study cluster-counting signal formation. 66

4.13 Experimental setup used for commissioning and preliminary cosmic-ray tests of the CEPC multilayer prototype. The setup includes the drift chamber, trigger scintillators, front-end electronics, digitization chain and data-acquisition system used to validate stable detector operation. 67

4.14 Preliminary waveform-quality measurements obtained with the CEPC multilayer prototype during commissioning. The distributions show baseline noise (left), signal rise time (center) and signal amplitude (right), confirming that the acquired waveforms are suitable for subsequent signal and cluster-reconstruction studies. 67

5.1 Copper-clad PET tab used for single-filament tensile testing. The central circular window defines the free gauge length of the wire specimen, while the copper-clad regions provide controlled attachment points and reduce direct handling of the ultra-thin filament. 72

5.2 Experimental setup for tensile testing of ultra-thin drift-chamber wires. Left: complete setup including digital dynamometer, custom gripping system, mounted tab and three-axis piezoelectric actuation stage. Right: close-up of the actuator and tab region used to impose controlled displacement while maintaining alignment of the wire specimen. 73

5.3 Rate-dependence study performed on 20 μm W–Au wires. The average ultimate tensile strength (left) and Young's modulus (right) are shown as a function of crosshead velocity, indicating stable quasi-static mechanical response in the tested velocity range. 74

5.4 Representative engineering stress–strain curves for 20 μm W–Au wire (left) and Mo–Au wire (right). The plots show the linear elastic fit used to extract Young's modulus, the 0.1% offset construction used to determine the proof-stress yield value, and the ultimate tensile strength at rupture. 75

5.5 Representative engineering stress–strain curve for the tested carbon monofilament. The abrupt fracture and limited plastic deformation indicate a brittle-like response, for which the yield tensile strength is effectively coincident with the ultimate tensile strength within the experimental uncertainty. 76

5.6 High-power impulse magnetron sputtering (HiPIMS) system considered for metallic coating of carbon monofilaments. Left: schematic representation of the physical-vapor-deposition process. Right: photograph of the sputtering apparatus. Such coatings are relevant for improving electrical conductivity, solderability and detector compatibility of carbon field-wire candidates. 77

6.1 PLB test: amplitude spectra of the acoustic waveforms recorded for specimens 41–44 in configuration B, where the acoustic source and the receiving sensor are located on opposite surfaces of the specimen. For each specimen, the pre-irradiation spectrum is compared with the spectra measured after 40 h and, where available, 80 h of UV exposure. The comparison highlights irradiation-induced changes in the transmitted frequency content, especially in the high-frequency region. 87

6.2 PLB test: heat maps of the damage indices extracted from the waveform analysis. The upper panel summarizes the shape pipeline, based on normalized spectral descriptors (f_c, BW and R), while the lower panel summarizes the physics pipeline, based on amplitude-preserving quantities (E, RMS and R_E). Values close to unity indicate little variation with respect to the pre-irradiation state, whereas values significantly above or below unity indicate UV-induced changes in spectral distribution or transmitted acoustic energy. 88

6.3 AU test: representative frequency spectrum of the pulser excitation used in the active transmission measurements. The observed spectral content motivates the adopted analysis band of 200–750 kHz and the choice of 300 kHz as the threshold separating low- and high-frequency components in the H/L and R_E indicators. 94

6.4 AU test: heat maps of the waveform-based damage indices obtained from the active transmission measurements. The upper panel reports the shape-pipeline indices, which describe changes in spectral morphology, while the lower panel reports the physics-pipeline indices, which preserve amplitude information and quantify changes in transmitted energy. The comparison between configurations A and B allows the sensitivity of surface and through-thickness propagation paths to UV-induced degradation to be assessed. 96

7.1 Garfield++ simulation of the energy-loss distribution for a muon crossing 200 drift cells of 1 cm length filled with a 90/10 He–iC_4H_{10} gas mixture. The asymmetric Landau-like tail illustrates the intrinsic limitation of charge-based dE/dx estimators and motivates the use of cluster counting. 101

7.2 Principle of the cluster-counting method in a drift cell. Left: charged-particle track crossing the gas volume and producing discrete primary-ionization clusters. Right: corresponding waveform at the sense wire, where temporally resolved peaks can be associated with individual ionization electrons and grouped into primary clusters. 102

7.3 Analytical expectation for particle-separation power in a 90/10 He–iC_4H_{10} gas mixture. Top: comparison between cluster-counting separation power (solid curves) and optimized truncated-mean dE/dx separation power (dashed curves). Bottom: ratio between the two methods, showing the expected gain obtained from the more favourable statistics of primary-cluster counting. 103

7.4 Beam-test momentum coverage superimposed on a representative Bethe–Bloch curve. The CERN SPS and PS campaigns probe complementary $\beta\gamma$ regions, including the relativistic-rise and Fermi-plateau domains relevant for validating cluster counting as a particle-identification technique. 105

7.5 Preparation infrastructure for the drift-tube beam-test campaign. Left: set of brass drift tubes with different cell sizes and sense-wire configurations used to scan cluster-counting performance. Right: portable gas system used to monitor and regulate the He–iC_4H_{10} mixture supplied to the tubes during commissioning and data taking. . . 106
7.6 Electrical-connection scheme of the beam-test drift tubes. The sense wire is biased through the high-voltage distribution board, while the signal is extracted from the opposite side through a high-voltage decoupling board and transmitted to the waveform digitization chain. . 106
7.7 Experimental setup used for the cluster-counting beam-test campaign, viewed from the downstream side. The main components include the drift-tube array, trigger scintillators, gas distribution, high-voltage connections and waveform readout system used to acquire the fast signals required for peak and cluster reconstruction. 107
7.8 Example of electron-peak and cluster identification in a recorded drift-tube waveform for a 1 cm cell with a 20 μm sense wire, a 45° track angle, a 90/10 He–iC_4H_{10} gas mixture and a sampling rate of 2 GSa/s. The top panel shows the Running Template Algorithm (RTA), while the bottom panel shows the derivative-based algorithm (DERIV); red arrows indicate individual electron peaks and blue arrows indicate reconstructed clusters [15]. 110
7.9 Ionization-resolution scaling with effective track length for conventional charge-based dE/dx and cluster-counting dN/dx estimators. The fitted trends follow approximately $L^{-0.37}$ for the truncated-mean dE/dx method and $L^{-1/2}$ for dN/dx, confirming the more favourable Poisson-like statistical behaviour of primary-cluster counting. 112

List of Tables

1.1 Global design parameters used for the FCC-ee/CEPC comparison. FCC-ee values refer to the updated layout ($C \simeq 91.2$ km) and parameter set in Table 2 of Ref. [6]. CEPC values refer to Table 1 and text of Ref. [7]. 5
1.2 Key beam parameters at the four operating points for FCC-ee and CEPC in the 2-IP configuration. 6
1.3 Baseline IDEA detector layout parameters. 8

2.1 Connection between detector-performance requirements and the R&D studies presented in this thesis. 30

3.1 Baseline mechanical quantities driving the endcap support design (design-level estimates). 34
3.2 Summary of the main results obtained from the concept-level endcap FEM analysis. 43

4.1 Comparison of the main design features of the FCC-ee and CEPC drift chamber concepts. 55
4.2 Wire tension summary by step. 59
4.3 Maximum equivalent elastic strain and maximum equivalent (von Mises) stress as a function of the endplate thickness, as obtained from the ANSYS static structural analysis. 62
4.4 Comparison of the maximum equivalent elastic strain and maximum equivalent (von Mises) stress for the two endplate versions. 65

5.1 Tensile test results for 20 μm W-wire: ultimate tensile strength (UTS) and Young's modulus (E) as a function of crosshead velocity. 74
5.2 Summary results of the tensile-test campaign for W–Au, Mo–Au and carbon monofilament wires. 75

6.1 PLB test: waveform analysis results - Shape Damage Indices 87
6.2 PLB test: waveform analysis results - Physics Damage Indices 87
6.3 Summary of the main PLB damage signatures observed after UV exposure. 91
6.4 AU test: damage index based on transmission loss 93
6.5 AU test: damage Index on the transmission loss post/pre. 95
6.6 Summary of the main AU damage signatures observed after UV exposure. 97

A.1 PLB test: AEWin features for each configuration. 122
A.2 PLB test: waveform analysis results - AE Shape features 123
A.3 PLB test: waveform analysis results - AE Physics features 123
A.4 AU test: global transmission loss for each feature. 124
A.5 AU test: shape pipeline AE Loss features. 124
A.6 AU test: physics pipeline AE Loss features. 125

Introduction

The next generation of particle-physics experiments will require tracking detectors with unprecedented precision, low material budget, and long-term stability under demanding operating conditions. In particular, future high-luminosity electron–positron colliders conceived as Higgs factories will rely on detector systems capable of delivering excellent momentum resolution, efficient pattern recognition, and advanced particle-identification performance, while preserving the highest possible transparency to traversing particles. Within this framework, drift chambers remain a highly attractive solution for charged-particle tracking, owing to their excellent spatial resolution, large active volume, low mass, and consolidated operating principles.

The development of such detectors is inherently interdisciplinary, as it lies at the interface between high-energy physics, mechanical design, and materials engineering. This research activity is situated precisely at that intersection. Its primary goal is the design, construction, and validation of innovative drift chambers for future collider experiments, with special focus on ultra-light mechanical solutions and on the behavior of candidate materials in radiation-intensive environments. In this sense, the work is not limited to detector development alone, but also contributes to a complete characterization of lightweight and radiation-resistant structures, which are of potential interest in other engineering fields, including aerospace applications.

The present research addresses three closely connected themes. The first concerns the mechanical and structural design of the chamber. A large drift chamber consists of two endplates connected by several hundred thousand thin wires, whose cumulative tension generates a substantial mechanical load on the supporting structure. Ensuring sufficient stiffness while keeping a very low material budget is therefore a major design challenge. In this work, particular attention is devoted to the optimization of endplate geometries based on lightweight composite solutions, developed with CAD tools such as *SolidWorks* and assessed through finite-element simulations performed in *ANSYS*. The mechanical design is influenced by the need to limit deformations under load while minimizing multiple scattering and preserving detector transparency.

The second theme concerns the study of ultra-thin wires, which are a fundamental element of drift-chamber operation. Sense wires provide gas amplification and signal formation, while field wires shape the electric field and guarantee the proper operation of the drift cells. Their mechanical properties are crucial, since wire material and diameter affect positioning accuracy, electrostatic stability, robustness during assembly, and long-term reliability. A systematic mechanical characterization of candidate filaments is therefore necessary to identify suitable materials and

define safe operating conditions for detector construction.

The third theme concerns the performance of materials under radiation exposure. The materials employed in the chamber structure must retain their mechanical integrity and functional properties over long periods of operation. In particular, polymers and composite materials may undergo degradation when exposed to ultraviolet radiation, cosmic rays, or other environmental agents. For this reason, the present work combines experimental investigations and numerical analyses to study damage mechanisms and to develop strategies for performance prediction and mitigation.

Alongside these mechanical and material aspects, the detector concept must also satisfy stringent physics requirements. The optimization of drift-cell electrostatics, the choice of gas mixture, and the implementation of advanced readout strategies are essential for figuring out the final tracking and particle-identification performance. In this context, particular importance is given to the *cluster counting* technique, which exploits the identification of individual primary-ionization clusters to improve particle identification and enhance the intrinsic measurement capability of the chamber.

The work presented in this thesis is developed in the context of R&D activities for future lepton-collider detectors, with particular reference to the IDEA detector concept proposed for FCC-ee and to conceptually related drift-chamber solutions under study for CEPC. In both cases, the drift chamber is regarded as a promising central tracker because of its capability to combine excellent momentum resolution, low material budget, and particle-identification potential. This thesis therefore contributes to that broader international effort by addressing the mechanical feasibility, material robustness, and prototype-oriented validation of such detectors.

The research plan also includes prototype activities aimed at validating the design choices under realistic conditions. Cosmic-ray muons provide a natural source for detector testing and make it possible to investigate both the mechanical stability of the system and the performance of the readout chain. These activities are carried out in collaboration with the Polytechnic University of Bari, the University of Salento, and the INFN sections of Bari and Lecce.

This thesis is organized as follows.

- Chapter 1 introduces the physics and detector context of future lepton colliders, with an emphasis on the FCC-ee and CEPC programmes and on the IDEA detector concept.

- Chapter 2 presents the IDEA drift chamber and its operating principles.

- Chapter 3 describes the mechanical design studies and the finite-element simulations performed on the chamber and on the prototype structures.

- Chapter 4 is devoted to the test-beam activities carried out to validate the cluster-counting technique and to quantify its impact on the detector particle-identification capability.

- Chapter 5 presents the scientific contribution to the CEPC drift chamber studies, including simulation studies of the proposed detector concept and structural analyses of the related prototype.

- Chapter 6 reports the results of the mechanical characterization of ultra-thin wires for drift-chamber applications.
- Chapter 7 discusses the aging and degradation studies carried out on composite materials intended for use in the detector structure.
- Chapter 8 summarizes the main results of the thesis and outlines possible future developments.

By combining detector physics, structural mechanics, and materials science, this research aims to contribute to the development of next-generation tracking detectors and to advance the design of ultra-light, high-performance systems for future particle-physics experiments.

Chapter 1

Challenges for an experiment at the future circular collider

The field of high–energy particle physics has been transformed in recent decades by successive generations of colliders, culminating in the Large Hadron Collider (LHC) at CERN (European Organization for Nuclear Research), a 27 km circular proton–proton collider that enabled the discovery of the Higgs boson in 2012 and continues to probe the Standard Model (SM) with ever increasing precision. Despite its tremendous success, the SM leaves several fundamental questions unanswered, including the nature of dark matter [1], the mechanism behind the matter–antimatter asymmetry of the Universe, the origin of neutrino masses [2], and the stability of the Higgs potential at high energies. These open problems motivate both precision studies of known phenomena and exploration at higher energy scales unreachable by current instruments, going beyond the standard model [3].

To deal with these challenges, the high–energy physics community has proposed future colliders capable of extending both the energy and luminosity frontiers. Among these, the *Future Circular Collider* (FCC) at CERN represents one of the most ambitious initiatives to follow the LHC, once the High-Luminosity phase (HL-LHC) is completed in 2041. The FCC study envisions a new circular research infrastructure with a circumference of approximately 91 km that would host two subsequent collider stages: first, an electron–positron collider (FCC–ee) optimized for high–precision measurements, followed by a proton–proton collider (FCC–hh) reaching center–of–mass energies up to 100 TeV, significantly exceeding the LHC's energy reach [4]. The FCC–ee stage is designed to provide extremely precise measurements of Higgs boson properties and electroweak observables, operating at multiple center of mass energies $\sqrt{s}$, producing 10^{13} Z bosons, 10^8 WW pairs, 10^6 Higgs bosons, and over 10^6 $t\bar{t}$ pairs. Whereas FCC–hh wants to explore the energy frontier directly, with energies capable of producing more than 10^{10} Higgs bosons in the total operability period, offering unprecedented discovery potential for phenomena beyond the SM and the ability to produce heavy new states if they exist.

In parallel, the *Circular Electron–Positron Collider* (CEPC) proposal, developed by the Chinese high–energy physics community, seeks to establish a dedicated "Higgs factory" in a circular tunnel of approximately 100 km circumference. The CEPC baseline design foresees operation at multiple center–of–mass energies, including

91.2 GeV (the Z pole), 160 GeV (WW threshold), and around 240–250 GeV for Higgs production, with the potential to accumulate millions of Higgs bosons over the course of several years. The CEPC design also anticipates a future upgrade to a *Super Proton–Proton Collider* (SPPC) in the same tunnel, extending the search for new physics to multi–ten TeV energies [5].

The scientific logic for these large–scale facilities is fundamentally twofold. First, precision measurements at electron–positron colliders such as FCC–ee and CEPC provide stringent tests of the SM, probing quantum effects and possible deviations due to new physics at scales beyond direct reach. For example, measurements of Higgs couplings, rare decays, and electroweak parameters at per–mille level precision can reveal subtle hints of physics beyond the SM through effective field theory frameworks. Second, achieving higher center–of–mass energies, as proposed for FCC–hh and SPPC, dramatically increases discovery potential for heavy new particles predicted in various beyond–the–Standard–Model (BSM) scenarios, including supersymmetry, heavy gauge bosons, dark matter candidates, and phenomena associated with extra dimensions.

These physics goals translate directly into stringent requirements on the experimental apparatus: excellent momentum resolution and vertexing, robust particle identification, highly granular calorimetry, and long-term operational stability under sustained high event rates.

Achieving this performance is not a simple extrapolation of current detector technologies. The combination of extreme luminosity, large integrated statistics, and demanding systematic control introduces a set of coupled challenges spanning machine-detector interface, backgrounds and radiation environment, mechanical integration, alignment and calibration strategies, data acquisition, and computing. In addition, the scale of the detectors implied by a very large collider ring imposes constraints on material budget, service routing, thermal management, and maintainability that become central design drivers rather than secondary engineering details. A further, often under-emphasized aspect is that mechanical design becomes a first-order contributor to physics performance: for large tracking systems, the stability of load-bearing structures (endplates, support frames, tie-rods, cryostats and service supports) rules the time-dependence of alignment constants and can induce systematic biases through deformations and stress relaxation. In this regime, mechanical engineering choices are therefore part of the detector response model and must be co-optimized with calibration and reconstruction.

The FCC and CEPC proposals reflect the willingness of the international high-energy physics community to advance both the precision and energy frontiers to address unanswered questions of the Standard Model and explore the fundamental structure of the Universe. These projects build on the results of the LHC and aim to extend our knowledge of fundamental physics processes.

1.1 FCC-ee and CEPC: two ideas, similar purposes

The following section summarizes the machine parameters that are most relevant for detector design. FCC-ee and CEPC share the same conceptual role as circular e^+e^- precision factories, but their reference parameter sets imply different experimental

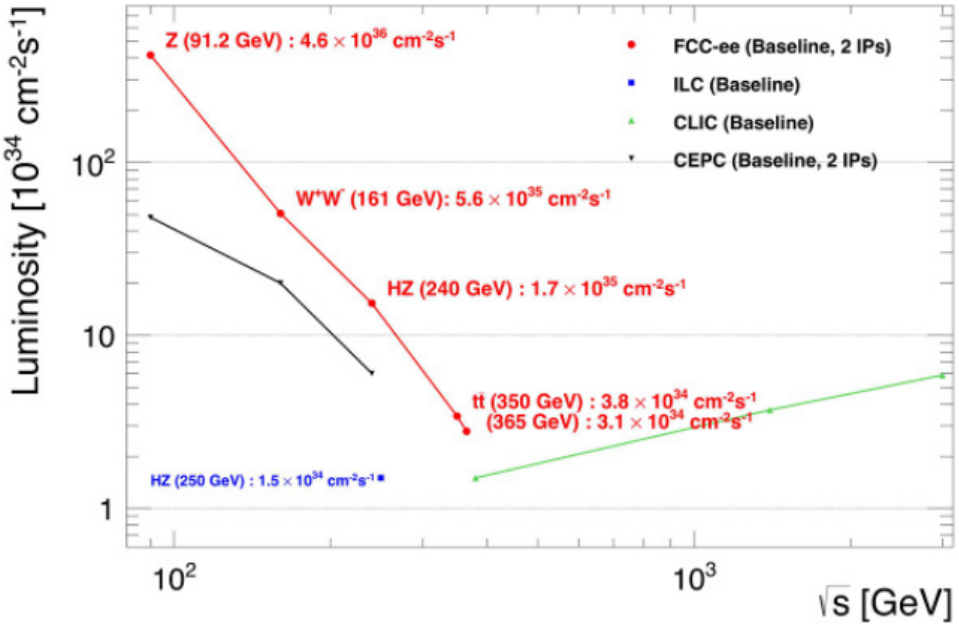

Figure 1.1: Target instantaneous luminosity as a function of the center-of-mass energy for the main proposed future e^+e^- colliders. Circular machines such as FCC-ee and CEPC provide very high luminosity at the Z, WW and Higgs operating points, defining the rate and precision environment that drives the detector-performance requirements discussed in this chapter.

boundary conditions in terms of bunch structure, beam current and achievable luminosity at the key energy points. Both colliders are designed to deliver very large integrated luminosities at multiple center-of-mass energies, with machine parameters that vary strongly with energy to satisfy synchrotron-radiation (SR) power and beam-dynamics constraints. Luminosity is an important indicator of the performance of an accelerator: it is proportional to the number of collisions that occur in a given amount of time. The higher the luminosity, the more data the experiments can gather to allow them to observe rare processes. Figure 1.1 depicts the difference between the main future colliders in terms of the luminosity. FCC provides the highest data rates.

1.1.1 The FCC-ee collider overview

The FCC integrated program has been proposed as a staged facility in a large tunnel in the Geneva basin, starting with an e^+e^- collider (FCC-ee) and followed by a 100 TeV hadron collider (FCC-hh) reusing the same civil infrastructure and benefiting from CERN's existing injector chain.

FCC-ee is a double-ring storage collider (see Figure 1.2 - left), with electrons and positrons circulating in separate rings, allowing a very large number of bunches to be stored simultaneously and thus increasing the collision rate. It foresees compatibility with up to four interaction points (IPs). The reference operating points are the Z pole ($\sqrt{s} \simeq 91$ GeV), the WW threshold ($\sqrt{s} \simeq 160$ GeV), the Higgsstrahlung maximum ($\sqrt{s} \simeq 240$ GeV), and the $t\bar{t}$ threshold ($\sqrt{s} \simeq 365$ GeV) [6]. In the

updated parameter set, FCC-ee operation at the Z pole (2-IP scenario) involves 12 000 bunches per beam, a beam current of 1.28 A, and a luminosity per IP of $L_{\mathrm{IP}} = 193 \times 10^{34}\,\mathrm{cm}^{-2}\,\mathrm{s}^{-1}$, whereas at the top threshold the regime shifts to 40 bunches and 5 mA, with $L_{\mathrm{IP}} = 1.31 \times 10^{34}\,\mathrm{cm}^{-2}\,\mathrm{s}^{-1}$ [6]. At the IP, the beams collide with a small horizontal crossing angle (of order 30 mrad in the present concept), and the machine is operated flexibly by adjusting the bunch pattern and current as a function of energy [6].

In a leptonic circular collider, two effects must be taken into account to design the machine: the synchrotron-radiation (SR) and the *bremsstrahlung* (BS) effect. The first one is the radiation emitted when leptons are bent by magnets, and the second effect is due to the collision-induced radiation in the strong electromagnetic field of the opposing bunch. For this FCC-ee adopts an SR power cap of 50 MW per beam (100 MW total), which directly constrains the allowable beam current and the longitudinal beam dynamics across the energy stages [6]. Consistently, the energy loss per turn increases from $U_0 \simeq 0.039$ GeV at the Z pole to $U_0 \simeq 10$ GeV at the $t\bar{t}$ threshold [6]. The radio-frequency (RF) system is staged with energy: the reference set combines 400 MHz SRF (up to 4 GV) with an additional 800 MHz voltage (7.25 GV) for the highest-energy operation [6]. For this reason, FCC-ee explicitly reports longitudinal parameters both from SR alone and including bremsstrahlung at collision (SR+BS), quantifying the increase in bunch length and relative energy spread at the interaction point [6].

To keep the beam current and luminosity close to their peak values during data taking, FCC-ee relies on continuous top-up injection, enabled by a dedicated booster synchrotron in the collider tunnel [6]. A key operational point is maintaining the electron and positron bunch intensities equal within a few percent to avoid beam–beam flip-flop; when restarting from zero, a dedicated *bootstrapping* injection scheme with alternating injections into the two collider rings is foreseen to prevent large charge imbalances [6].

For the electroweak programme, FCC-ee exploits transverse polarization and resonant depolarization for an accurate calibration of the centre-of-mass energy at $\sqrt{s} \approx 91$ and 160 GeV, with calibration targets at the level of $\mathcal{O}(100\ \mathrm{keV})$ for m_Z and $\mathcal{O}(300\ \mathrm{keV})$ for m_W in the FCC-ee framework [6].

1.1.2 The case of CEPC: comparison and implications

Both FCC-ee and CEPC are circular e^+e^- storage colliders with a double-ring structure designed to deliver very large integrated luminosities at multiple center-of-mass energies, with machine parameters that vary strongly with energy to satisfy synchrotron-radiation (SR) power and beam-dynamics constraints.

Although FCC-ee and CEPC share the same role, their baseline parameter sets imply different experimental boundary conditions, particularly at the Z pole, where the combination of large bunch number and high current drives detector time structure and occupancy. Those differences are summarized in Table 1.1 and in Table 1.2. Figure 1.2 depicts the structure of the two future circular colliders.

A central difference is the synchrotron-radiation (SR) power model: FCC-ee adopts a cap of 50 MW per beam (100 MW total), whereas CEPC quotes a 30 MW

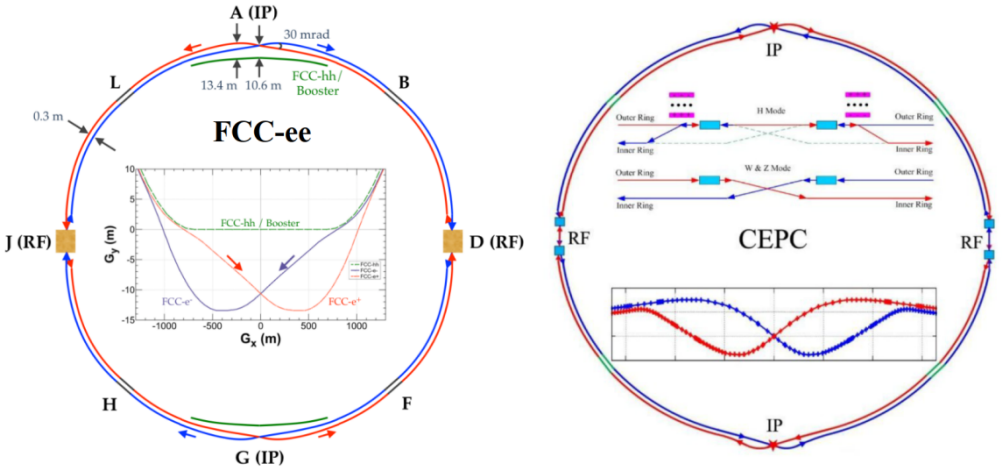

Figure 1.2: Schematic layouts of the two circular lepton-collider infrastructures considered in this thesis: FCC-ee at CERN (left) and CEPC in China (right). Both machines are designed as high-luminosity e^+e^- factories, but their different tunnel dimensions, machine parameters and implementation choices lead to different detector boundary conditions.

baseline with an upgrade path to 50 MW for higher luminosity. At the Z pole (45–46 GeV/beam), the FCC-ee 2-IP set stores 12 000 bunches per beam with a beam current of 1.28 A and reaches $L_{\mathrm{IP}} = 193 \times 10^{34}\,\mathrm{cm}^{-2}\,\mathrm{s}^{-1}$ per IP, while the CEPC set has 11 951 bunches, 0.804 A and $L_{\mathrm{IP}} = 115 \times 10^{34}\,\mathrm{cm}^{-2}\,\mathrm{s}^{-1}$.

At the Higgs point (120 GeV/beam), FCC-ee quotes 272 bunches, 26.7 mA and 7.73×10^{34} per IP, compared to CEPC 249 bunches, 16.7 mA and 5.0×10^{34} per IP; at the top threshold region the reference luminosities differ more markedly (FCC-ee: 40 bunches, 5.0 mA, 1.31×10^{34}; CEPC: 35 bunches, 3.3 mA, 0.5×10^{34}). The RF strategies differ: FCC-ee combines 400 MHz RF cavities for high-intensity operation at lower energies (up to 4 GV) with additional 800 MHz voltage for the highest-energy operation, whereas CEPC adopts 650 MHz RF and a staged RF configuration; these choices, together with *bremsstrahlung* (explicitly tabulated in FCC-ee via "SR" versus "SR+BS" bunch length and energy spread), set different conditions for time structure, energy spread and ultimately detector calibration and reconstruction.

Table 1.1: Global design parameters used for the FCC-ee/CEPC comparison. FCC-ee values refer to the updated layout ($C \simeq 91.2$ km) and parameter set in Table 2 of Ref. [6]. CEPC values refer to Table 1 and text of Ref. [7].

Parameter	FCC-ee	CEPC
Collider type	double-ring storage collider	(partial/full) double-ring compatible
Circumference C [km]	~ 91.2	100
Baseline IPs	2 (option 4)	2
Main energy points (beam energy) [GeV]	45.6, 80, 120, 182.5	45, 80, 120, 180
SR power (collider)	50 MW/beam (100 MW total)	30 MW baseline (upgrade to 50 MW)
RF frequency	400 MHz (+800 MHz for $t\bar{t}$)	650 MHz

Table 1.2: Key beam parameters at the four operating points for FCC-ee and CEPC in the 2-IP configuration.

	FCC-ee (2 IP)				CEPC (2 IP)			
Mode	Z	W	ZH	$t\bar{t}$	Z	W	Higgs	top
Beam energy E_b [GeV]	45.6	80	120	182.5	45	80	120	180
Bunches/beam	12000	880	272	40	11951	1297	249	35
Beam current [mA]	1280	135	26.7	5.0	803.5	84.1	16.7	3.3
Luminosity/IP [10^{34} cm^{-2} s^{-1}]	193	22.0	7.73	1.31	115	16	5.0	0.5
β_x^* at IP [m]	0.10	0.20	0.30	1.00	0.13	0.21	0.33	1.04
β_y^* at IP [mm]	0.8	1.0	1.0	1.6	n/a	1.0	1.0	2.7
RMS bunch length [mm]	$12.1^{(\mathrm{SR+BS})}$	$7.06^{(\mathrm{SR+BS})}$	$5.12^{(\mathrm{SR+BS})}$	$2.56^{(\mathrm{SR+BS})}$	$8.7^{(\mathrm{total})}$	$4.9^{(\mathrm{total})}$	$3.9^{(\mathrm{total})}$	$2.9^{(\mathrm{total})}$

1.2 An experiment for future colliders: the IDEA detector

Among the detector concepts proposed for future circular lepton colliders, IDEA (Innovative Detector for an Electron-positron Accelerator) is a promising option and is explicitly discussed as a detector concept compatible with FCC-ee and CEPC running conditions [8], [9]. The IDEA experiment is introduced here as a response to the machine boundary conditions summarized above.

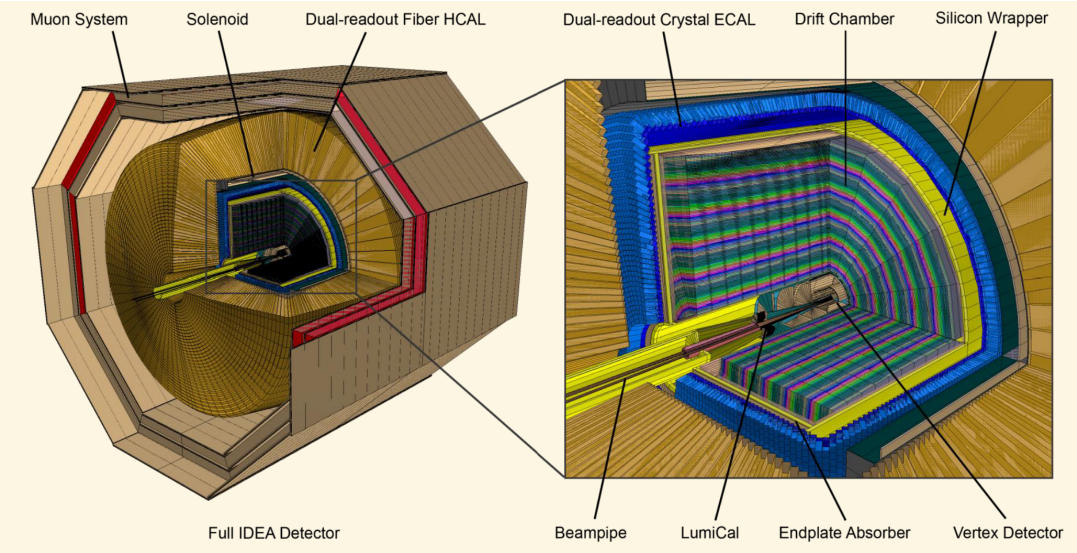

Figure 1.3: Full IDEA detector concept for a future circular e^+e^- collider. The figure shows the nested detector architecture, from the innermost vertex detector and central drift chamber to the calorimeters, solenoid, return yoke and muon system. The large-volume drift chamber is the central tracking element addressed in this thesis.

IDEA is a detector concept designed to study electron–positron annihilation over a wide range of center-of-mass energies. The detector is organized as a measurement chain in which tracking, timing, and calorimetry provide complementary constraints on event kinematics and particle identification. Figure 1.3 presents the full IDEA detector concept with its shell structure and Figure 1.4 shows a cross-section overview of the detector layout. The detector is built around a high-performance tracking system and it consist of a high-resolution silicon pixel vertex detector, a large-volume ultra-low-mass drift chamber acting as the central tracker and providing particle identification, and an outer silicon wrapper that improves pattern

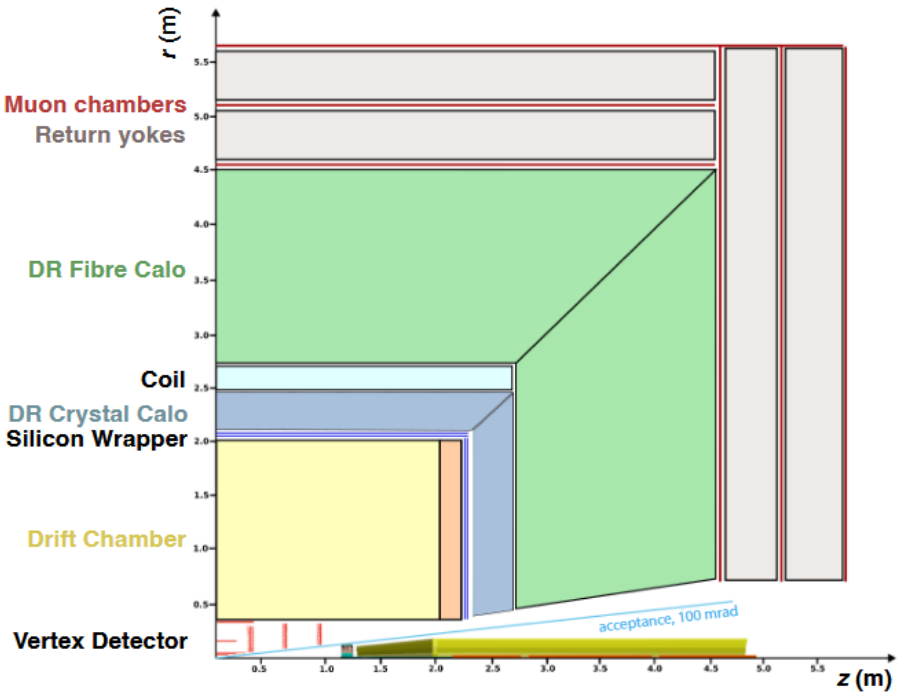

Figure 3: Overview of the IDEA detector layout.

Figure 1.4: Cross-sectional view of the IDEA detector layout, showing the relative position of the vertex detector, central drift chamber, silicon wrapper, solenoid, calorimeters and muon system. The figure highlights the radial envelope available for the ultra-light drift chamber and its integration with the surrounding detector subsystems.

recognition. Electrons and photons are measured in a finely segmented crystal dual-readout (DR) electromagnetic calorimeter housed inside a low-mass superconducting solenoid with a magnetic field of 2T. Outside the solenoid, a DR fiber calorimeter provides hadronic energy measurements, and the detector is completed by a muon system installed in the iron yoke that returns the magnetic flux. Table 1.3 list the baseline detector parameters.

Vertex technology	Silicon
Vertex inner/outer radius	1.7 cm / 34 cm
Tracker technology	Drift chamber + silicon wrapper
Tracker half length/outer radius	2.0 m / 2.0 m
Solenoid bore radius/half length	2.1 m / 3.0 m
Preshower/calorimeter absorber	Lead / lead
Preshower inner/outer radius	2.4 m / 2.5 m
DR calorimeter inner/outer radius	2.5 m / 4.5 m
Overall height/length	11 m / 13 m

Table 1.3: Baseline IDEA detector layout parameters.

The detector subsystems are briefly reviewed in order to define the experimental context for the drift-chamber studies discussed in the following chapters.

1.2.1 Machine–detector interface and beam pipe

The machine–detector interface (MDI) and the beam pipe define the innermost mechanical envelope and the background conditions in the forward region. They set the available radius for vertexing, the local material budget near the interaction point, and the constraints on forward instrumentation and shielding.

1.2.2 Vertex detector (VTX).

The silicon pixel vertex detector provides high-granularity space points close to the interaction point. The main components are based on $50\mu m$ thick Monolithic Active Pixel Sensors (MAPS) [8]. The detector includes two subsystems:

- an inner vertex detector, located close to the beam pipe, at radii between 13.7 and 35.6 mm, covering an angular acceptance of about $|cos(\theta)| < 0.99$;
- an outer vertex detector, located at larger radii between 130 and 315 mm, composed of a barrel section and forward disks.

Its primary role is the reconstruction of primary and secondary vertices and the measurement of impact parameters for heavy-flavor tagging, while maintaining low material to limit multiple scattering and secondary interactions [10].

1.2.3 Silicon wrapper and timing layers

A silicon wrapper surrounds the drift chamber ($|z| < 2.25$ m and $r < 2$ m), covering an area of more than $100m^2$, to provide an external precision reference surface. It

strengthens pattern recognition and stabilizes the momentum measurement, especially in the forward region. The sensor technology for the Silicon Wrapper has not been fixed yet. In case fast-timing sensors (e.g. low gain avalanche diode - LGAD) are adopted, the goal would be to reach a time resolution per track of $\mathcal{O}(100$ ps) for time-of-flight particle identification which, together with the cluster counting from the drift chamber, ensures a $K - \pi$ separation power of more than three sigma up to momenta of 30 GeV/c [8].

1.2.4 Magnet system

A superconducting solenoid, 5 m long and with an inner diameter of 4.2 m, provides the magnetic field for momentum reconstruction. With a 2 T field and the proposed compact geometry, the total thickness of the magnet package can be kept at about 30 cm. For these dimensions, an iron return yoke thinner than 100 cm is sufficient to fully confine the magnetic flux while providing the required shielding and mechanical support for the muon chambers. The return yoke serves as both an absorber and a mechanical support for the outer detectors.

1.2.5 Electromagnetic calorimeter (ECAL)

Electrons and photons are measured in a high-granularity electromagnetic calorimeter based on dense crystals. The concept supports longitudinal segmentation and, in the dual-readout approach, separation of scintillation and Cherenkov components (via wavelength and/or timing discrimination) to constrain early hadronic components and improve linearity and stability of the response. The IDEA Dual-Readout Crystal calorimeter section is designed to achieve an electromagnetic energy resolution better than $3\%/\sqrt{E} \bigoplus 1\%$ and includes the simultaneous readout of scintillation and Cherenkov photons which, integrated with the DR fiber hadronic calorimeter section, can provide a hadronic energy resolution of about $30\%/\sqrt{E} \bigoplus 3\%$ [11], [12].

1.2.6 Hadronic calorimeter (HCAL)

Hadronic showers are measured in a dual-readout fibre calorimeter with independent scintillation and Cherenkov readout. Their combination provides an event-by-event estimator of the electromagnetic shower fraction, enabling compensation and reducing fluctuations that dominate hadronic energy resolution, with direct impact on jet measurements.

1.2.7 Muon system

Muon identification is performed by tracking stations integrated in or placed outside the yoke (baseline technologies include micro-pattern gaseous detectors such as μ-RWELL), which combine high tracking efficiency with precise spatial resolution for muon-hit coordinates ($200-300\mu m$) and good timing performance. This technology also enables a substantial cost reduction when instrumenting the very large surfaces required outside the calorimeter [13].

1.2.8 A promising experiment for FCC-ee

The concept of the IDEA experiment is promising because its detector architecture is matched to the dominant constraints of a high-luminosity circular e^+e^- collider, in particular FCC-ee: it targets ultra-low material in the tracking volume, robust particle identification (PID) in the few-GeV momentum range, and stable jet measurements with reduced sensitivity to intrinsic hadronic shower fluctuations. A critical operating point is the Z *pole*, i.e. running at a center-of-mass energy $\sqrt{s} \simeq m_Z \simeq 91.2$ GeV, where the collider delivers extremely large event samples and therefore shifts the limiting factor from statistics to detector systematics and calibration stability. In this regime, tracking performance is strongly affected by multiple Coulomb scattering, which scales with the traversed material expressed in units of radiation length X_0; therefore, the quantity x/X_0 of the tracker and its supports becomes a first-order term in the momentum and impact-parameter error budgets.

IDEA addresses this problem by adopting an ultra-light central tracker based on a large-volume drift chamber complemented by an external silicon wrapper, ensuring a significant reduction in the material budget of the barrel region (central pseudorapidity) [14]. This choice is particularly effective in the FCC-ee baseline magnetic-field regime (about $B \simeq 2$ T at the Z pole), where the achievable momentum resolution benefits strongly from large tracking radii and minimal x/X_0.

A distinctive feature is that the drift chamber is not only a tracking device but also a PID detector. IDEA targets cluster counting/timing by reconstructing the number of primary ionization clusters per unit length, dN_{cl}/dx, from the time structure of the wire signals. Since dN_{cl}/dx fluctuations are closer to Poisson statistics than charge-based dE/dx estimators (which exhibit Landau tails), cluster counting can improve π/K separation by approximately a factor two with respect to conventional dE/dx under controlled conditions, enhancing flavour-physics performance at the Z pole. Beam-test results with long drift-chamber prototypes support the feasibility of the technique in realistic conditions and clarify practical limitations such as cluster overlap, δ-rays, and noise [15].

IDEA also treats readout and data reduction as part of the detector design. At the target event rates and time structure of FCC-ee running, transferring raw multi-GS/s waveforms from a detector-scale drift chamber is not sustainable. A viable baseline is online feature extraction, transmitting compact peak parameters (time and amplitude) rather than full waveforms, with implementations demonstrated in FPGA-based architectures [16].

In calorimetry, IDEA pursues dual-readout techniques to reduce the dominant fluctuations of hadronic shower response. By measuring the scintillation and Cherenkov light components separately, the electromagnetic fraction of a hadronic shower can be estimated event-by-event and used to correct the calorimetric response, aiming to improve jet-energy resolution and stability with reduced dependence on global calibration assumptions. Together with a high-granularity ECAL, a solenoidal field, muon instrumentation in the return yoke, the overall system provides redundant constraints explicitly aimed at systematic control over long data-taking periods.

These design choices make IDEA a credible candidate for a precision experiment at future circular colliders. They also imply that mechanical integrity and long-

term stability of structural components—in particular in the drift-chamber end-cap region where services and wire loads concentrate—are performance-critical and must be treated as part of the physics error budget. Overall, IDEA is attractive because it treats low material, PID, scalability of readout, and calorimetric stability as coupled requirements, consistent with the systematic-limited regime expected for FCC-ee precision physics. This also makes the mechanical stability of the drift-chamber end-cap region performance-critical, since it concentrates wire loads and services and therefore couples directly to alignment and calibration systematics.

For the purposes of this thesis, the most important implication is that mechanical stability is not an isolated engineering requirement. In a large drift chamber, endplate deformation, wire-position stability, material budget and long-term dimensional stability directly affect the time-to-distance calibration, the electrostatic configuration of the cells, the momentum resolution and the reliability of cluster-counting reconstruction. The mechanical studies presented in the following chapters are therefore interpreted as part of the detector-performance optimization.

1.3 Operating principle of the drift chamber

From the previous sections it is clear that one of the main sub-detectors of the IDEA experiment will be the central part of the tracker formed by the largest drift chamber ever built. Gaseous tracking detectors remain a competitive solution when large volumes must be instrumented with minimal material and stable performance over long data-taking periods. In particular, modern ultra-light drift chambers are engineered to provide precise tracking while enabling particle identification (PID) through ionization-based observables. But to appreciate the design choices it is useful to recall some fundamental physical principles underlying the functioning of drift chambers, summarizing the physical processes that govern the detector response, from the interaction of charged particles with matter to charge transport, amplification, and the specific operating principles of multi-wire and drift chambers.

1.3.1 Particles through matter

A charged particle traversing matter interacts predominantly through the electromagnetic field of atomic electrons and nuclei. For tracking detectors the relevant outcomes are: (i) energy loss by excitation and ionization, which creates the primary signal carriers, and (ii) deflections of the trajectory due to multiple Coulomb scattering, which set an irreducible limit through the material budget.

1.3.2 Electromagnetic interactions and energy loss

For heavy charged particles ($m \gg m_e$), the mean rate of energy loss per unit length in a medium is described by the Bethe–Bloch equation [17]. In a compact form, the mass stopping power is:

$$-\left\langle \frac{dE}{dx} \right\rangle = Kz^2 \frac{Z}{A} \frac{1}{\beta^2} \left[\frac{1}{2} \ln\left(\frac{2m_e c^2 \beta^2 \gamma^2 T_{\max}}{I^2} \right) - \beta^2 - \frac{\delta(\beta\gamma)}{2} \right], \tag{1.1}$$

where z is the projectile charge, Z and A are the absorber atomic number and mass, β and γ are the usual relativistic factors, I is the mean excitation potential, $T_{\max}$ is the maximum kinetic energy transferable to a free electron, δ accounts for the density effect, and K is a constant.

In thin absorbers the energy deposition fluctuates strongly because occasional hard collisions transfer large energies to single electrons. The resulting straggling is non-Gaussian and leads to a long high-energy tail. In practice, ionization-based PID does not use the arithmetic mean of the samples; robust estimators such as truncated means are preferred. A small subset of energetic knock-on electrons ("δ rays") can propagate away from the primary track and locally increase the charge yield, contributing both to fluctuations and to pattern-recognition ambiguities in dense events.

At the same time, multiple Coulomb scattering introduces an angular spread that scales with the material thickness expressed in radiation lengths X_0. A widely used approximation for the RMS projected scattering angle is

$$\theta_0 \simeq \frac{13.6\ \text{MeV}}{\beta pc}\sqrt{\frac{x}{X_0}}\left[1 + 0.038\ln\left(\frac{x}{X_0}\right)\right], \tag{1.2}$$

highlighting why low-mass tracking concepts prioritize minimizing x/X_0.

Energy loss rates for relativistic ionizing particles

For PID, the relevant observable is often a *truncated* energy loss, obtained by limiting the contribution of large-energy transfers (typically by rejecting energetic δ rays above a chosen threshold). This procedure reduces the Landau tail and yields an estimator closer to the most probable energy loss.

As $\beta\gamma$ increases, $\langle dE/dx\rangle$ decreases to the minimum-ionizing region and then slowly rises (relativistic rise) before approaching a saturation region (the "Fermi plateau") determined by the density-effect term [17]. A typical behavior of the stopping power in a copper for positive muons is shown in Figure 1.5.

In a drift chamber, this behavior sets the intrinsic separation power of charge-based dE/dx measurements at high momentum, and motivates alternative observables that are less sensitive to large fluctuations, such as the primary-cluster density [17].

1.3.3 Main principles of a gas detectors

In a gas detector, the passage of a charged particle produces excited atoms and ion pairs. An applied electric field suppresses recombination and drives electrons and ions toward electrodes, where the signal is formed either by direct charge collection or by gas amplification.

Primary ionization: clusters

The process of energy loss of a charged particle in a material is statistical and for this reason the ionization in gases occurs in localized points along the track; each

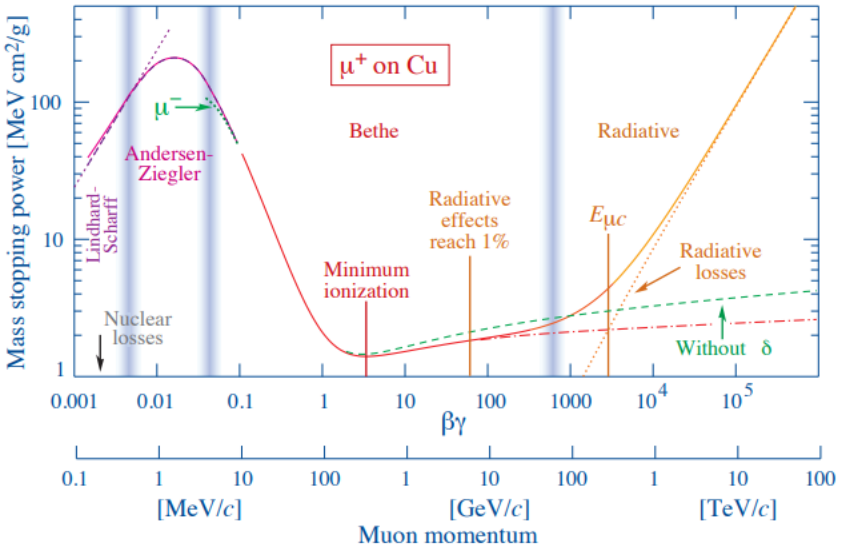

Figure 1.5: Mass stopping power for positive muons in copper as a function of $\beta\gamma$. The curve illustrates the minimum-ionizing region, the relativistic rise and the approach to the Fermi plateau, which provide the physical basis for ionization-based particle identification in tracking detectors.

point produces a *cluster* of one or more electrons. The number n of primary clusters in a path length L is well modeled, to first order, by a Poisson distribution [18]:

$$P(n|L,\lambda_{\mathrm{cl}}) = \frac{(\lambda_{\mathrm{cl}}L)^n}{n!}e^{-\lambda_{\mathrm{cl}}L} \tag{1.3}$$

where λ_{cl} is the cluster density for the chosen gas mixture and pressure and the mean of the distribution is $\bar{\mu}_{\mathrm{cl}} = \lambda_{\mathrm{cl}}L$.

The distinction between *cluster count* and *total charge* is central for PID. Charge-based measurements aggregate the electrons from all clusters and are dominated by rare large transfers (Landau tails), while the number of primary ionization acts is intrinsically closer to Poisson statistics and can therefore provide a more stable estimator when the individual clusters can be resolved in time.

The average number of electron–ion pairs produced by an energy deposit E_{dep} is

$$\bar{n}_e = \frac{E_{\mathrm{dep}}}{W}, \tag{1.4}$$

where W is the mean energy required to create one ion pair in the gas. The intrinsic statistical fluctuations are reduced with respect to a pure Poisson process by the Fano factor F, leading to $\sigma^2_{n_e} \simeq F\bar{n}_e$ in the absence of additional detector effects. In practice, attachment, recombination, gain fluctuations, electronics noise and thresholds typically dominate the effective resolution.

1.3.4 Electron and ions mobility

Once created, electrons drift toward the anode with a drift velocity

$$v_d = \mu_e E, \tag{1.5}$$

where μ_e is the electron mobility and E is the local electric field. The drift velocity is not a purely linear function of E in real gases: it depends on the microscopic energy distribution of electrons, hence on the reduced field E/N (with N the gas number density) and on mixture composition [19]. Many mixtures are chosen to operate in a "velocity plateau" region where v_d is relatively insensitive to small variations of E and gas conditions.

During transport, electrons diffuse. The transverse and longitudinal RMS spreads can be expressed as

$$\sigma_T = \sqrt{2D_T t}, \tag{1.6}$$

with D_T the diffusion coefficient that depends on the temperature T (calculated form the kinetic theory of gas) and t the drift time. In the presence of a magnetic field $\mathbf{B}$, electrons experience an $\mathbf{E} \times \mathbf{B}$ drift that rotates the drift direction by the Lorentz angle. Diffusion is reduced in the transverse plane for sufficiently large B, improving spatial resolution and pattern recognition, but the Lorentz angle must be measured or modeled to avoid systematic distortions [20].

Ions drift orders of magnitude more slowly than electrons. Their motion shapes the tail of the induced signal and can lead to space-charge effects at high rate, modifying the local electric field and thus the gain and drift properties. Gas purity is also critical: electronegative impurities cause electron attachment, reducing the collected charge and biasing time-based reconstruction.

1.3.5 The avalanche multiplication and gas choice

Gas multiplication arises when the electric field in the gas is raised to sufficiently high values. At low field strengths, the electron–ion pairs produced by a traversing particle simply drift to the collecting electrodes, undergoing frequent collisions with neutral molecules. Because ions have low mobility, they gain only a small amount of kinetic energy between collisions and therefore do not trigger further ionization. Electrons, in contrast, are easily accelerated by the applied field and can acquire substantial kinetic energy between collisions. If, during a collision, an electron's energy exceeds the ionization potential of a neutral molecule, an additional electron–ion pair can be produced. Since the mean electron energy between collisions increases with electric field, there exists a threshold field above which such secondary ionization becomes possible and gas amplification starts. This process is known as *Townsend avalanche* and the increase of electron per unit path length is described by the Townsend equation $\frac{dn}{n} = \alpha dx$, where α is the first Townsend's coefficient [20]. Avalanche multiplication can occur in essentially any gas, so in principle a proportional counter can be operated with a wide range of gases or mixtures. In practice, the choice is constrained by experimental requirements such as low operating voltage, high and stable gain, good proportionality, high-rate capability, and long-term reliability. The gas mixture defines the detector response through several coupled properties: primary-cluster density, drift velocity, diffusion, gain stability, aging, and safety/operational constraints. A typical mixture combines a light noble gas (to reduce multiple scattering and radiation length), with a molecular quencher (to provide stable operation, suppress photon feedback, and tune transport properties). Penning effects can enhance the effective ionization yield when metastable

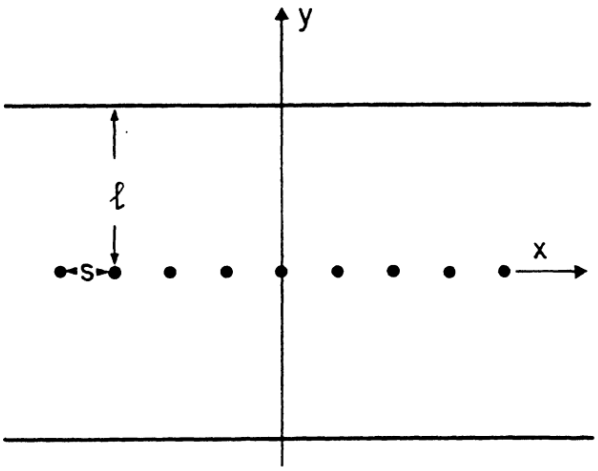

Figure 1.6: Schematic layout of a multi-wire proportional chamber (MWPC). Parallel anode wires are placed between cathode electrodes; ionization electrons drift toward the high-field region around the anodes, where avalanche multiplication produces detectable signals.

states of one component transfer energy to another component [21].

1.4 From Multi-wire proportional chambers to drift chamber

Multi-wire proportional chambers (MWPCs) consist of a plane of parallel anode wires between cathode electrodes, as shown in Figure 1.6. Each wire acts as an independent amplification element, and position information is obtained from the wire index and charge sharing on segmented cathodes. When an ionizing particle produces charge in the gas volume, the electrons drift along the electric-field lines toward the anode. As they enter the high-field region near the wire, they undergo avalanche multiplication. Near thin anode wires the electric field scales approximately as $E(r) \propto 1/r$, reaching values high enough to initiate impact ionization. The number of electrons grows exponentially along the path, characterized by the first Townsend coefficient $\alpha(E)$:

$$G = \exp\left(\int \alpha(E)\, ds \right), \tag{1.7}$$

where G is the gas gain. In the proportional regime, the induced signal is proportional to the initial ionization. At higher fields, secondary processes (photon feedback, ion feedback) can trigger streamers and breakdown; quenchers are therefore added to absorb UV photons and dissipate energy through molecular excitations.

The measured signal is induced by the motion of charges in the detector volume and can be described by the Shockley–Ramo theorem [19]. Fast timing performance is governed by the prompt electron motion, while the long ion drift induces slower components that define pulse shape and pile-up behavior.

The avalanche induces a large negative-polarity pulse on the anode wire, while adjacent anode wires typically register smaller pulses of opposite polarity due to

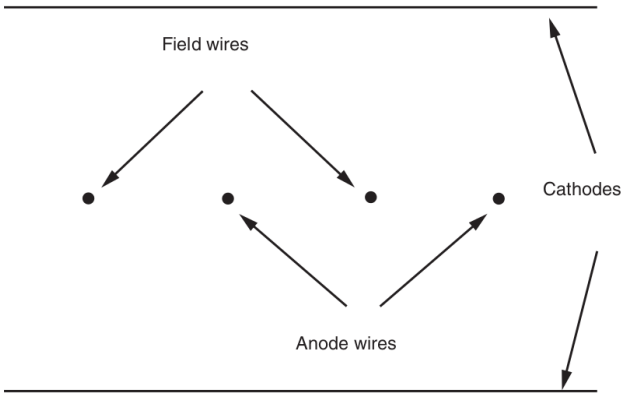

Figure 1.7: Schematic representation of a drift-chamber wire layer. Alternating anode and field wires define the drift cells and shape the electric field, allowing the charged-particle position to be reconstructed from the electron drift time to the nearest anode wire.

capacitive and inductive coupling. By reading out each wire with dedicated preamplifier, the hit position can be assigned to the nearest anode wire [22]. MWPCs offer robust operation and large-area coverage, but their rate capability and spatial resolution are limited by ion space charge, wire pitch, and diffusion. From an engineering perspective, MWPC-like amplification structures define the electrostatic design language of many gaseous trackers: field shaping, gain uniformity, stability against discharges, and the routing of signals and high voltage are all governed by the same physical constraints described in Sections 1.3.4–1.3.5.

1.4.1 Drift chamber detector

Drift chambers are similar in construction to the MWPC but the wires in the central layer are further apart. These wires consist of alternated 'field' and 'sense' wires in which the voltages across them, produce an electric field in which the electrons 'drift' at a constant velocity towards the nearest sense where they initiate a current pulse. Figure 1.7 depicts the drift chamber scheme of one layer of wires. While not as fast as a MWPC, with drift chambers it has proved possible to measure the position of particle tracks to an accuracy of 50 μm [21].

A drift chamber measures the position of a charged particle by converting the electron drift time to a distance from the sense wire. In a drift cell (Figure 1.8), the measured time t is mapped to a radial coordinate $r(t)$ through a calibrated time-to-distance relation, which depends on the electric and magnetic fields, the gas mixture, pressure/temperature, and the local cell geometry. An event-level time reference t_0 must be established (from a trigger, from external detectors, or from self-calibration strategies) to avoid systematic shifts in reconstructed positions.

The single-hit spatial resolution results from several contributions:

- electronics time resolution and discriminator/sampling strategy;
- electron diffusion during transport;
- primary-ionization statistics, which limit how accurately the earliest arriving electrons trace the true impact parameter;

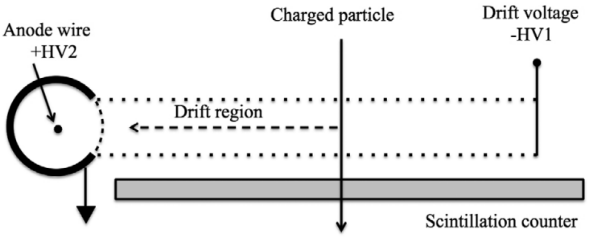

Figure 1.8: Single drift-cell geometry illustrating the conversion of drift time into a distance from the sense wire. The calibrated time-to-distance relation depends on the gas mixture, electric and magnetic fields, pressure, temperature and local cell geometry.

- calibration uncertainties in $r(t)$, including field non-uniformities and $\mathbf{E} \times \mathbf{B}$ effects.

At small drift distances, the finite density of primary clusters can bias the "first-electron" time, particularly in light gas mixtures, because the first observed electron does not necessarily correspond to an ionization act produced arbitrarily close to the track. This effect is one of the drivers for cluster-based reconstruction approaches.

For PID, drift chambers can exploit either the total collected charge (a dE/dx-like observable) or, when fast readout allows it, the number and timing of resolved ionization clusters (dN_{cl}/dx). In fact, for ultra-light drift chambers intended for precision tracking, helium-based mixtures are attractive because of their low radiation length and reduced multiple scattering. The trade-off is a lower primary-ionization density, which makes traditional dE/dx PID less effective unless long track lengths are available. This motivates PID techniques based on primary-cluster counting and timing, which exploit the statistics of ionization acts rather than the total deposited charge. Cluster counting leverages the more stable statistics of primary ionization and can improve PID performance compared with charge-based estimators, while cluster timing can also provide additional constraints for spatial reconstruction by using information from multiple clusters within the same cell. These techniques become particularly relevant for ultra-light drift chambers envisioned for future collider experiments like IDEA, where minimizing x/X_0 is essential and where PID must be achieved without introducing large additional subsystems.

1.5 Scope of the thesis and original contributions

This thesis is focused on the mechanical and technological R&D required for the development of ultra-light drift chambers for future lepton colliders, with particular emphasis on the INTREPID drift chamber concept and on related CEPC studies.

The original contributions of this work are:

- the development of CAD models and finite-element studies for the INTREPID endplate support concept, including the analysis of spoke deformation and the role of the stay-based tension-recovery system;
- the mechanical study of alternative CEPC drift-chamber endcap geometries, including thickness optimization and comparison between stepped and concave configurations;

- the design and implementation of an experimental tensile-test procedure for ultra-thin drift-chamber wires, with extraction of UTS, YTS and Young's modulus for candidate wire materials;
- the acoustic and acousto-ultrasonic characterization of UV-aged carbon-fiber benzoxazine composites as a model system for assessing early degradation in lightweight detector structures;
- the preparation, commissioning and operation of drift-tube prototypes used in cluster-counting beam-test campaigns.

The cluster-counting performance results discussed in Chapter 7 are obtained within a collaborative R&D programme. In this thesis they are used to connect the technological and mechanical studies to the expected detector-level particle-identification performance.

Chapter 2

The IDEA experiment core: the INTREPID drift chamber

Future circular lepton colliders, such as FCC-ee and CEPC, set detector conditions where performance is increasingly limited by systematic effects rather than by statistical precision. In the tracking system, this translates into a coupled set of constraints:

- *radiation transparency* to suppress multiple scattering at low transverse momentum, hence an aggressive material-budget minimisation for structures and services;
- *high granularity and fast response* to control occupancy and pile-up under the machine time structure;
- *stable calibration and alignment* over long data-taking periods;
- *radiation tolerance* of materials and electronics to preserve performance and mechanical integrity.

Meeting these requirements is not a single-parameter optimisation of gas or wire configuration, but a multidisciplinary design problem in which mechanics, materials, electrostatics and readout architecture must be treated consistently. We now discuss the drift chamber of the IDEA experiment, proposed by the INFN Bari and Lecce groups as part of the FCC detector R&D program, with the goal of installation at CERN.

2.1 Proposal for a new drift chamber

The drift chamber (DCH) for the IDEA detector concept is a large-volume, high-granularity, full-stereo, ultra-light cylindrical drift chamber operated with a helium-based gas mixture. The concept exploits the expertise earned from the previous chamber of KLOE experiment [23], successfully operated at the Daphne facility of the Frascati INFN Laboratories for over 20 years, and MEG II experiment [24], part of the upgrade of the MEG experiment which has produced an improved upper limit on the muon decay in a positron and a gamma [25] at the PSI laboratories in Zurich.

Main peculiarities of this design are the high transparency in terms of multiple scattering contributions to the momentum measurement of charged particles and its very promising particle identification capabilities. Indeed, a distinctive design goal is to integrate particle identification directly in the tracker via cluster counting/timing: the DCH exploits the time structure of the wire signals to reconstruct the number of primary ionisation clusters per unit length, dN_{cl}/dx, reducing sensitivity to Landau tails in charge-based dE/dx estimators and improving hadron separation in the few-GeV regime [26]. This combination of tracking and PID is attractive for flavour physics and exclusive final states, but it imposes stringent requirements on front-end bandwidth, timing performance, and feature-extraction strategies for scalable readout. For these reasons, it's more than a simple drift chamber and we call it **INTREPID** -*INnovative TRacking detector Equipped with Particle IDentification.*

Considering the large size of the chamber—enclosed in a cylinder about 4 m long and 4 m in diameter—the technological challenges are manifold and concern primarily the chamber's mechanical structure, which must comply with the stringent constraints of a precision machine of this kind. In particular, the research and development program aims to optimize the mechanical structure along several fronts, including:

- mechanical design of the drift chamber end plates with a novel tension recovery scheme to minimize the amount of material in front of the end-plate calorimeter.
- development of a new type of field wires based on carbon monofilament coated with a thin metal layer to allow for ease of soldering.
- study of new composite materials based on carbon fibres, capable of contributing to the transparency of the chamber without sacrificing the robustness of the structure

These also correspond to the themes covered in this thesis in the next chapters, where detailed preliminary studies on each part are presented.

2.2 Layout of the INTREPID drift chamber

The INTREPID drift chamber extends radially from an inner radius $R_{in} = 35$ cm, surrounding the inner tracking system, to an outer radius $R_{out} = 200$ cm, with a total length $L_{tot} = 450$ cm, which correspond to the length of the active area $L = 400$ cm and 25 cm service area at both ends. A schematic drawing of the drift chamber is presented in Figure 2.1. The chamber is built around a mechanical structure consisting of two end-plates forming the two bases of the cylindrical volume, and outer panels that make up the cylindrical barrel. Each end-plate is made of 24 *Spokes* with a length $l = 165$ cm, anchored between an inner and an outer ring as shown in the figure. The area covers the whole azimuthal angle ϕ subdivided in 24 identical 15° sectors.

In the active inner region of the chamber, 342,720 wires are placed between the two end-plates, divided in sense, field and guard wires in the following way:

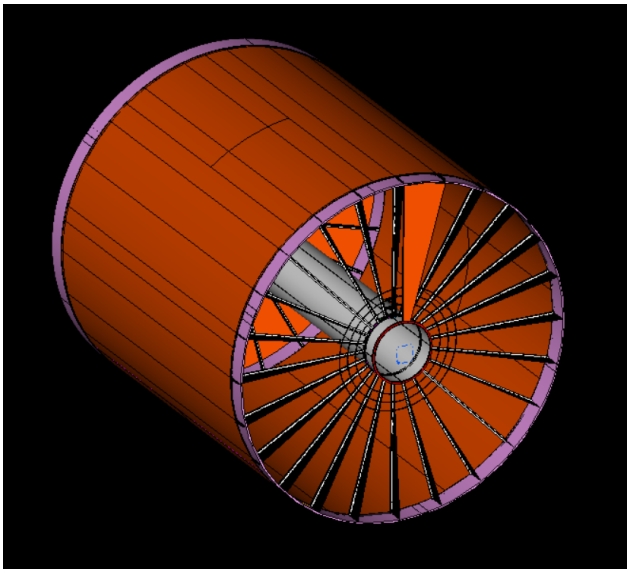

Figure 2.1: Schematic three-dimensional view of the INTREPID drift chamber concept. The detector consists of a large cylindrical wire volume closed by two endplates and supported by a low-mass mechanical structure designed to minimize material while preserving wire-position stability.

- 56,448 **sense** wires of gold-plated Tungsten (W-Au) or gold-plated Molybdenum (Mo-Au) with a diameter of $20\mu m$.
- 284,256 **field** wires of silver-plated Aluminum (Al-Ag) or silver-plated Carbon monofilament (C-Ag) with a diameter of around $40\mu m$.
- 2,016 **guard** wires of silver-plated Aluminum (Al-Ag) or silver-plated Carbon monofilament (C-Ag) with a diameter of around $50\mu m$.

The sense wires are the active ones where the signals are induced, the field wires create the stable electric field, and the guard wires are used to isolate the innermost and outer layers to avoid edge effects on the electric field.

The wire ends are soldered, with a well-defined pitch, to printed circuit boards (PCB) and the chamber layout is obtained by stacking up radially, in each sector, the wire PCBs between adjacent spokes, to which they are constrained, alternated with spacers to set the proper cell width as illustrated in Figure 2.2 (left).

To limit deformations induced by the cumulative wire tension, the design adopts an array of adjustable stays. The concept is analogous to a harp cable-stayed bridge, see Figure 2.2 (right): the outer ring acts as the pylon, while the spokes play the role of the bridge deck. In this configuration, the wire load is redirected to the outer endplate rim, where a stiff cylindrical carbon-fibre support structure is anchored and designed to carry the full wire load.

2.3 The INTREPID wire scheme

The wires are arranged in a full stereo configuration, with one sector connected with the second corresponding sector in the opposite end-cap, which gives a hyperbolic

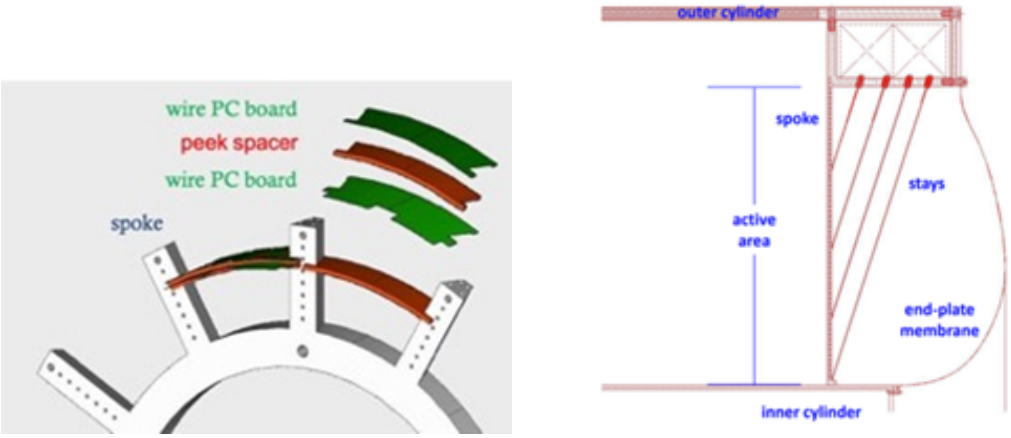

Figure 2.2: Mechanical concept of the INTREPID endplate. Left: wire-bearing PCB stacks alternated with spacers and inserted between adjacent radial spokes, following the feed-through-less construction approach developed for MEG II. Right: stay-based wire-tension recovery scheme, in which the radial spokes are supported by tensioned stays that redirect the cumulative wire load toward the outer support structure.

shape to the active volume.

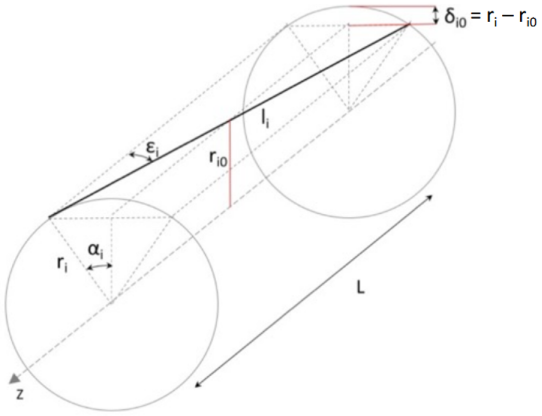

Figure 2.3: Geometrical definition of the stereo-wire configuration. The two wire ends are attached to azimuthally shifted sectors on opposite endplates, producing a stereo angle ϵ_i and a hyperboloidal wire envelope. The difference between the endplate radius r_i and the central radius r_{i0} determines the radial evolution of the wire position along z.

In Figure 2.3 is possible to appreciate the configuration:

- $\alpha_i = 15°$ is the angle of the ith-sector, $2\alpha_i = 30°$ is the azimuthal shift between the 2 wire ends.
- the difference δ_{i0} between the distance of the ith-wire from the central axis at the end-plate (r_i) and at the center (r_{i0}) is positive.
- ϵ_i represents the corresponding *stereo angle*.

As a consequence of this configuration, we have a different spatial distribution of the wires: they will be closer to the internal cylinder at the center of the chamber

($z = 0$) and closer to the external cylinder at the end-plates ($z = \pm L/2$) as shown in Figure 2.4.

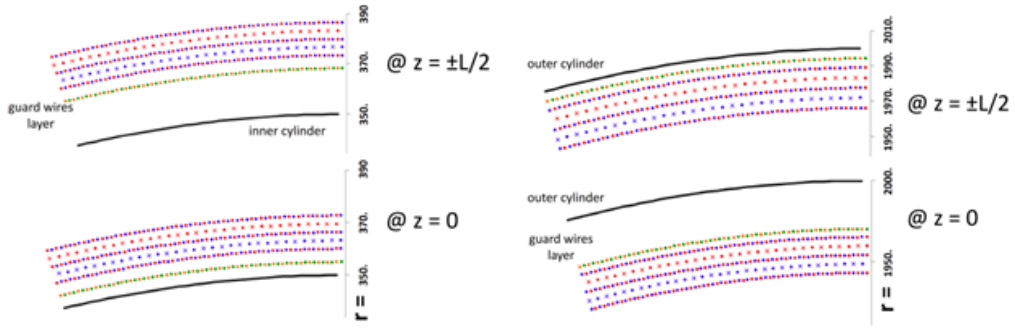

Figure 2.4: Projected wire distribution for the stereo layout near the inner chamber radius (left) and near the outer chamber radius (right). The changing apparent wire density reflects the hyperboloidal geometry generated by the full-stereo configuration.

2.3.1 Drift cell configuration

The totality of the wires is arranged in 14 coaxial super-layers, 8 layers each (112 total), with alternating-sign stereo angles ranging from 50 mrad to 250 mrad. The scheme of one super-layer is shown in Figure 2.5 (left). The wires are arranged to form drift cells approximately square with a range in size from 11.8 mm at the innermost layer to 14.9 mm at the outermost one. The number of drift cells ranges from 192 (at the inner layer) to 816 (at the outer layer). The ratio of field wires to sense wires is 5:1 to ensure the proper electrostatic configuration. The drift cells have wires with positive and negative stereo angles. They are then zipped together to form a structure in which the cathode wire layers form a rhomboidal network alternating with anode layers with opposite stereo angles. The positive and negative stereo angles define two projective views, the V-view and the U-view, respectively. All the wires with the same sign of the stereo angle are parallel; this is why the drift chamber takes the shape of a rotation hyperboloid whose surface is given by the envelope of the wires' planes. This process is pictured in Figure 2.5 (right). All the main parameter values are grouped in the Figure 2.6.

Figure 2.7 shows the drift chamber of MEGII experiment, where it is possible to notice the visual effect of the stereo configuration.

2.4 INTREPID Gas mixture choice

A very important element for a drift chamber is the gas mixture chosen to fill the sensitive volume. Usually, the mixture consists of a noble gas and a quencher: noble gases are used because they require lower electric field intensity for the formation of avalanches, on the other hand, the quencher is required to avoid self-sustained discharge. The INTREPID drift chamber requires a highly transparent gas to minimize the multiple scattering, for this reason the choice of a suitable gas mixture fell on a helium-based gas mixture, which has a long radiation length (for pure Helium

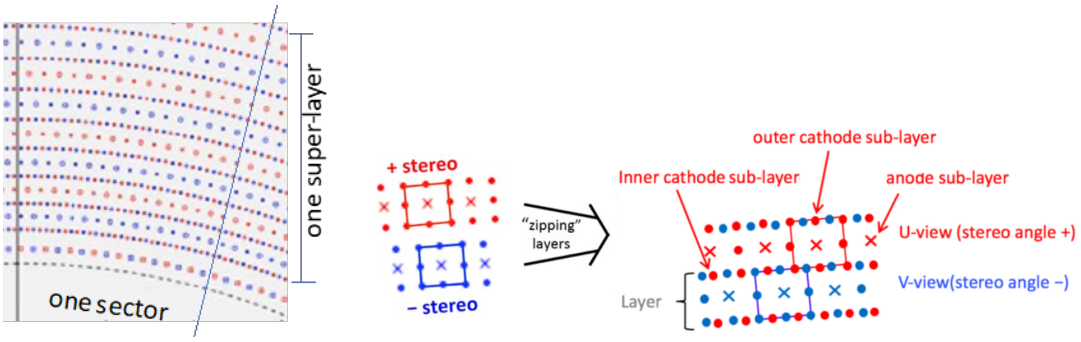

Figure 2.5: Stereo-cell organization of the INTREPID drift chamber. Left: schematic view of one super-layer with alternating wire layers. Right: arrangement of drift cells with positive and negative stereo angles, defining the U and V projective views required for three-dimensional track reconstruction.

Radii (at z = 0)		
Inner Cylinder	350	mm
Guard wires layer	354	mm
First active layer	356	mm
Last (112th) active layer	1915	mm
Guard wires layer	1927	mm
Outer Cylinder	2000	mm

Radii (at end plate)		
Inner Cylinder	350	mm
Guard wires layer	366	mm
First active layer	369	mm
Last (112th) active layer	1982	mm
Guard wires layer	1995	mm
Outer Cylinder	2000	mm

Active length	2000	mm
Number of super-layers (8 layers) Number of sectors	(14x8) = 112 24	
Number of cells per layer / per sector	192÷816 / 16	
Cell size (at z=0)	11.8 ÷ 14.9	mm
2α angle	30°	
Stereo angle	43 ÷ 223	mrad
Stereo drop	12.5 ÷ 68.0	mm

sense wires	56 448
field wires	284 256
guard wires	2 016
Total wires	342 720

Figure 2.6: Summary of the main INTREPID drift-chamber layout parameters, including radial dimensions, active length, number of layers, number of sectors, cell-size range and wire configuration. These values define the baseline geometry used in the mechanical and detector-performance studies.

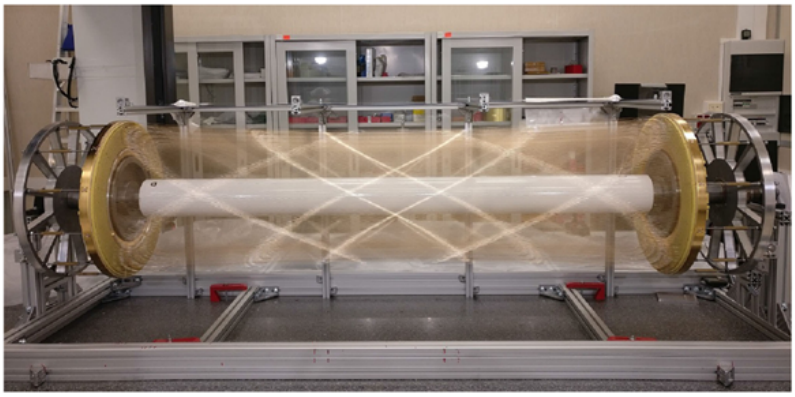

Figure 2.7: Complete MEG II drift-chamber wire cage. The visible twist of the wire layers illustrates the stereo geometry that inspired the feed-through-less wiring and full-stereo design strategy adopted for the INTREPID drift chamber.

the radiation length is 5300 m at STP); moreover it has a high ionization potential respect other noble gas, causes small primary ionization density and a small drift velocity, so that the time separation between consecutive ionization clusters goes from a few ns to a few tens of ns. These features are especially suitable for cluster counting techniques. For this reason, the ultra-low gas mixture suitable for the INTREPID drift chamber is formed by 90% Helium (He) and 10% Isobutane (iC4H10).

2.5 Design challenges for the INTREPID drift chamber

To design a chamber of this size, several practical limitations must be taken into account, both in the choice of wires essential for physics and in the choice of materials for structural stability.

2.5.1 Momentum and angular resolutions

The primary performance target of the drift chamber is the precise measurement of the transverse momentum of charged particles. The expected momentum resolution is

$$\frac{\sigma_{p_T}}{p_T} \approx 10^{-3} \quad \text{for } p_T = 1 \text{ GeV}.$$

The intrinsic spatial resolution per cell is estimated to be $100-120\ \mu m$, depending on the drift distance and gas properties. Through the use of cluster counting, a dE/dx resolution of about 3–4% can be achieved, enabling effective particle separation in the low- to mid-momentum range. The starting point is the separation of the transverse-momentum resolution into a measurement term and a multiple-scattering term. In a Gluckstern-like approximation [27], the measurement contribution scales as

$$\left.\frac{\Delta p_T}{p_T}\right|_{\text{res}} = \frac{\sigma_{r\phi}\, p_T}{0.3\, B_0\, L_0^2} \sqrt{\frac{720\, N^3}{(N-1)(N+1)(N+2)(N+3)}} \simeq \frac{12\, \sigma_{r\phi}\, p_T}{0.3\, B_0\, L_0^2} \sqrt{\frac{5}{N+5}}, \tag{2.1}$$

where $\sigma_{r\phi}$ is the single-hit transverse resolution, B_0 the solenoidal field, L_0 the effective active area, and N the number of measured points. The multiple-scattering contribution is written in terms of the effective material budget d_{tot}/X_0 (inner wall + gas + wires) as

$$\left.\frac{\Delta p_T}{p_T}\right|_{\text{m.s.}} \simeq \frac{0.0136 \text{ GeV}/c}{0.3\, \beta\, p\, B_0\, L_0} \sqrt{\frac{d_{\text{tot}}}{X_0 \sin\theta}}, \tag{2.2}$$

making explicit that low-momentum performance is controlled primarily by d_{tot}/X_0 rather than by intrinsic spatial precision. Assuming a solenoidal field $B_0 = 2$ T and an effective active area of $L_0 = 1.65$ m, as shown in Figure 2.8, the target high-momentum performance is expressed as $\Delta(1/p_T) \simeq 2\times10^{-5}\,(\text{GeV}/c)^{-1}$. In the drift-chamber-like tracker, the target is reached through a large number of space points, requiring $N > 100$ with a single-hit resolution $\sigma_{r\phi} \lesssim 100\ \mu$m. At low momentum,

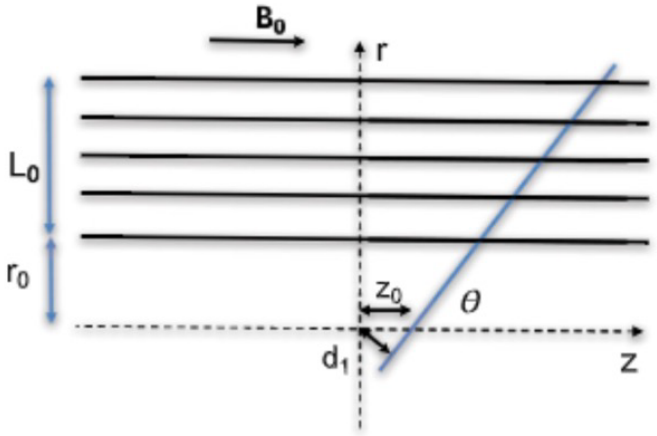

Figure 2.8: Conceptual transverse cross-section of the drift chamber in a solenoidal magnetic field B_0. The effective lever arm L_0 and the number of measured space points determine the measurement contribution to the transverse-momentum resolution, while the material budget controls the multiple-scattering term.

where multiple scattering dominates, the scaling $\Delta(1/p_T) \sim 10^{-3}/(p_T \sin\theta)$ and the corresponding material constraint is $d_{\text{tot}} \lesssim 5 \times 10^{-3} X_0$ (inner wall + gas + wires). In the same framework, the polar-angle resolution is expressed as

$$\Delta\theta|_{\text{res}} = \frac{\sigma_z \, \sin^2\theta}{L_0} \sqrt{\frac{12N}{(N+1)(N+2)}} \simeq \frac{2\,\sigma_z \, \sin^2\theta}{L_0} \sqrt{\frac{3}{N+3}}, \tag{2.3}$$

$$\Delta\theta|_{\text{m.s.}} \simeq \frac{0.0136 \text{ GeV}/c}{\beta \, p_T} \sin\theta \sqrt{\frac{d}{X_0 \sin\theta}}, \tag{2.4}$$

where σ_z is the effective longitudinal single-hit resolution and d denotes the relevant thickness driving scattering [27]. For an illustrative kinematic point $r_0 = 0.35$ m, $\theta = 45°$, and $p = 45$ GeV/c ($p_T \simeq 32$ GeV/c), the multiple-scattering contributions to the angular resolutions are quoted as $\Delta\theta|_{\text{m.s.}} \simeq \Delta\phi|_{\text{m.s.}} \simeq 40$ μrad, which sets the scale of the systematic sensitivity of angular measurements to the tracker material budget. Furthermore, the geometrical acceptance is connected to the inner radius by requiring $\Delta\Omega \simeq 98.5\%$ ($\theta_{\text{min}} \simeq 10°$), yielding $r_0 = (L_z/2)\tan\theta_{\text{min}} \simeq 0.35$ m, and it notes that this choice must be cross-checked against occupancy constraints driven by beam-related backgrounds. Finally, the angular-resolution requirement is used to derive explicit constraints on the stereo layout. A target of $\Delta\theta = \Delta\theta_{\text{res}} \oplus \Delta\theta_{\text{m.s.}} \lesssim 70$ μrad is imposed with the measurement component constrained to $\Delta\theta_{\text{res}} \lesssim 60$ μrad. For $B_0 \simeq 2$ T and $N \gtrsim 100$, this implies $\sigma_z \lesssim 0.6$ mm, which in turn requires that essentially all layers be stereo at an angle derived from:

$$\tan\varepsilon \gtrsim \frac{\sigma_{r\phi}}{\sigma_z}, \tag{2.5}$$

so that for $\sigma_{r\phi} \sim 100$ μm and $\sigma_z \lesssim 0.6$ mm one obtains stereo angles of order $|\varepsilon| \gtrsim 150$ mrad. So the momentum and angular targets are not independent: once B_0, L_0, and acceptance are fixed, the polar-angle requirement drives σ_z and hence the stereo strategy, with direct consequences for wire routing, end-cap complexity, and the mechanical tolerance budget of the tracking system.

2.5.2 Wire-tension constraints

The coupled requirements of electrostatic stability and material strength of the wires directly constrain the mechanical design of a long drift chamber. A conservative choice imposes the use of $40\mu m$ and $50\mu m$ diameter aluminum for field and guard wires and $20\mu m$ diameter tungsten or molybdenum for sense wires. However, the use of a new type of field wires based on carbon monofilament coated with a thin metal layer is under study and represents a concrete possibility to reduce by more than 30% the wire contribution to the total material budget of INTREPID. To achieve a balance of electrostatic and mechanical stability, a compromise must be found between the size of the wires and the size of the drift cell. A commonly used stability criterion [28] can be expressed as

$$T_c \;\geq\; \frac{C^2 V_0^2}{4\pi\,\varepsilon\,w^2}\,L^2, \tag{2.6}$$

where T_c is the wire tension, L the wire length, w the cell width, C the capacitance per unit length, V_0 the anode–cathode voltage, and ε the permittivity of the gas. The L^2/w^2 scaling makes this constraint particularly severe for long wires and small drift cells: increasing the chamber length or reducing the cell size rapidly raises the minimum tension required to prevent excessive electrostatic deflection and loss of stability. The maximum allowable tension is instead limited by the elastic (yield) strength of the wire material,

$$T_c \;<\; \mathrm{YTS}\,\pi r_w^2, \tag{2.7}$$

with YTS the yield tensile strength and r_w the wire radius. These two inequalities define a narrow feasible operating window when L is large (here $L \sim 4$ m) and w is of order 1 cm, because electrostatic stability pushes T_c upward while the elastic limit sets a hard upper bound that becomes more stringent for ultra-thin wires. The design implications are therefore explicit: either the wire radius and/or material strength must be increased, or the cell width and voltage must be adjusted, or alternative wire types and layouts must be adopted, to preserve an adequate safety margin. In a detector-scale chamber, maintaining this margin over time also requires that the endplate and support structure limit deflections and tension drifts, since small geometric changes propagate into the electrostatic equilibrium and ultimately into tracking stability.

2.5.3 Wire positioning

The electrostatic-stability and elastic-limit constraints connect directly to wire bowing (gravitational sagitta) and, ultimately, to the required accuracy in wire positioning. For a long drift chamber ($L \simeq 4$ m) and small cell width ($w \simeq 1$ cm), the mid-span deflection due to gravity, δ_{grav}, is intrinsically of the order of several $10^2\,\mu$m: $\delta_{\mathrm{grav}} \approx 510$–$580\,\mu$m for $20\,\mu$m W sense wires in the admissible tension range ($T_c \gtrsim 21$ g for electrostatic stability and $T_c \lesssim 24$ g from the elastic limit), and $\delta_{\mathrm{grav}} \approx 190$–$260\,\mu$m for $40\,\mu$m Al field wires ($26 \lesssim T_c \lesssim 36$ g). These values are consistent with the expected "bowing" of thin, long wires and demonstrate that

one cannot simply increase T_c to suppress sag because the available margin is small, especially for 20 μm tungsten. While the tracking requirement $\sigma_{xy} < 100\,\mu$m implies $\mathcal{O}(50\,\mu\text{m})$ accuracy on the anode-wire position, such micro metric tolerances must be understood as the residual misplacement *after* controlling (or compensating) the predictable bowing shape; otherwise the wire would deviate from the nominal geometry by ~ 0.5 mm at mid-span. Moreover, preserving a uniform and reproducible electric field requires anode and cathode wires to remain effectively parallel along z, i.e. to minimize *differential* sagitta between wire species; differing δ_{grav} for sense and field wires would introduce z-dependent anode–cathode spacing, impacting gain and the time-to-distance relation. Therefore, the combined constraints motivate design levers such as increasing wire radius, enlarging the cell size, adopting alternative wire types, and/or implementing mechanical schemes (profiling, pretension/tension-recovery concepts, dedicated supports) to keep relative alignment within the micrometric envelope demanded by the target spatial resolution.

2.5.4 Load constraints

With a nominal tension of about 30 g per wire, the cumulative contribution of the full wire set translates into a very large axial load on the endcap, of the order of ~ 10 tonnes. Assuming a segmentation into 24 sectors, this load is distributed over the radial spokes with an average of ~ 208 kg per spoke over a span of ~ 165 cm, corresponding to an equivalent line load of about 1.26 kg/cm. In first approximation, each spoke can therefore be idealized as a cantilever beam of length $L = 1650$ mm and cross-section $16 \times 10\,\text{mm}^2$, for which bending stiffness and deflection control become primary design drivers. A significant fraction of the load is further transferred to the stays: with ~ 14 stays per spoke, the average load is ~ 100 kg per stay (for a mean inclination angle $\langle\Phi\rangle \simeq 8.6^\circ$), despite their small cross-sectional area ($\sim 3\,\text{mm}^2$). This highlights the tight trade-off between material budget (transparency) and structural capacity, and motivates an endcap concept in which load paths are carefully engineered to limit deformations and local instabilities while sustaining the multi-ton wire preload.

2.5.5 Material budget

The material budget, usually expressed as a fraction of the radiation length X/X_0, quantifies the amount of matter traversed by a charged particle along its path through the detector and therefore represents one of the most critical parameters in the design of a tracking system. Indeed, it determines the extent to which the detector itself perturbs the particle before its trajectory is reconstructed. An excessive material budget enhances multiple Coulomb scattering, energy-loss fluctuations, and, for electrons and photons, bremsstrahlung and conversion processes. The impact of multiple scattering on the track angular resolution is commonly described by the equation 2.4, which explicitly shows that the characteristic scattering angle increases with the square root of the material budget. As a consequence, larger values of X/X_0 lead to a deterioration of the angular, momentum, and vertex resolutions, and may also reduce the effectiveness of particle-identification techniques.

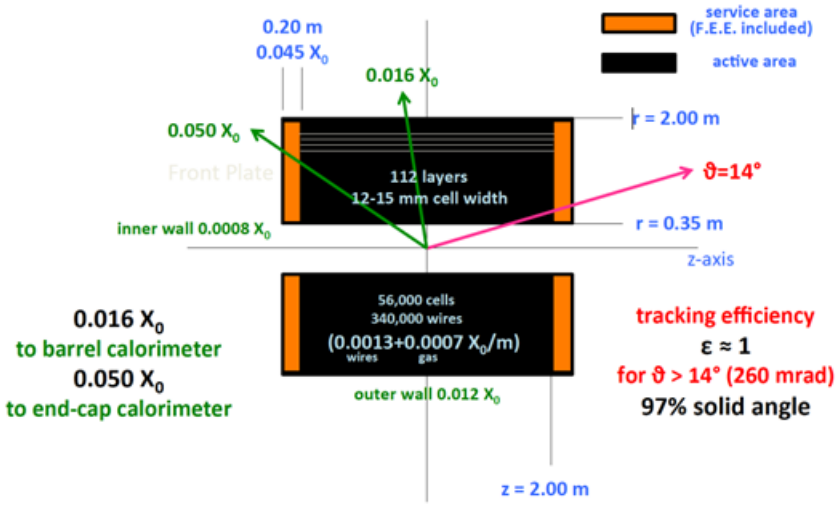

Figure 2.9: Material-budget breakdown of the drift-chamber concept, expressed in fractions of radiation length X_0. The barrel contribution is dominated by gas, wires and thin walls, while the forward region includes additional contributions from wire supports, endplate structures, front-end electronics, cables and services.

For this reason, minimizing and carefully controlling the material budget is a central requirement in detector design, especially for ultra-light drift chambers, where mechanical strength and stability must be achieved while preserving the highest possible transparency to traversing particles.

The material budget is decomposed into gas, wires, and structural elements: the gas and wires each contribute at the level of $\mathcal{O}(10^{-3})\,X_0$, while endplates including services can reach the $\mathcal{O}(10^{-2})\,X_0$–$\mathcal{O}(10^{-1})\,X_0$ scale and therefore dominate the forward material. A concrete trade-off example is proposed to recover wire-stability margin: increasing the cell size (e.g. $w > 1.5$ cm) and modifying the wire choice (including a different field-to-sense configuration) leads to a substantially wider stable-tension window (quoted as 30–87 g) and reduces the wire multiple-scattering contribution (e.g. $1.3 \times 10^{-3} X_0 \rightarrow 0.9 \times 10^{-3} X_0$). However, the same example increases the total number of wires and the cumulative wire load (quoted as $\sim 9 \rightarrow 18$ ton), shifting the dominant risk from single-wire electrostatics to the global mechanical design of the endcaps and support structures.

The amount of radiation length due to the inner and outer walls of the drift chamber, to the gas mixture and to the wire material is 1.6% X_0 in the radial direction and 5.0% X_0 in the forward direction, including wire support, gas containment and services (electronics, cables, etc.). A scheme with the total material budget is depicted in Figure 2.9.

2.6 Mechanical constraints study plan

The dominant engineering challenge for the INTREPID drift chamber at detector scale is the mechanical realisation of a structure that remains both transparent and stable under large cumulative wire loads. The chamber is defined by two endplates

Table 2.1: Connection between detector-performance requirements and the R&D studies presented in this thesis.

Detector requirement	Engineering consequence	Thesis study
Momentum resolution	Low material budget and stable wire geometry	Endplate FEM studies, Chapters 3–4
Low multiple scattering	Lightweight wires and composite structures	Wire and composite characterization, Chapters 5–6
Stable calibration	Limited endcap deformation and controlled wire tension	Tension-recovery studies, Chapter 3
Particle identification	Preservation of fast signal components for cluster counting	Beam-test studies, Chapter 7
Long-term operation	Material durability, ageing and damage monitoring	UV-aged composite diagnostics, Chapter 6

closing the cylindrical volume and by outer panels forming the barrel; approximately 3×10^5 wires are strung between the endplates, so that the total wire tension amounts to several tonnes. Consequently, the endcap region is simultaneously a load-bearing component and a performance-critical area, because it typically concentrates a significant fraction of the forward material budget together with services and front-end electronics. Within these constraints, the mechanical concept must satisfy three conditions at once: it must sustain the total wire load, limit endplate deflections to the sub-millimetre level to preserve wire geometry and calibration stability, and guarantee electrostatic stability of the drift cells by controlling wire sag and maintaining adequate tension margins. This motivates targeted R&D on lightweight load paths (e.g. adjustable stays/tie-rods and composite supports), on the optimisation of endplate stiffness distribution, and on the manufacturable integration of services within strict transparency requirements.

At the detector scale, these principles translate into coupled engineering constraints. The mechanical structure, defined by the end plates and the barrel panels, must sustain the cumulative tension of $\mathcal{O}(10^5)$ wires while maintaining a stable geometry over long periods. In practice, end-cap deformations and tension drifts propagate into wire positioning, electrostatic equilibrium and calibration constants, and therefore become part of the detector response model rather than secondary construction details. For this reason, the end-plate region is simultaneously a load-bearing element and a performance-critical area, where services and front-end electronics tend to concentrate and where the forward material budget is typically dominated.

The following chapters address the INTREPID drift-chamber design from three complementary directions. Chapter 3 studies the global mechanical stability of the endplate concept through CAD and FEM analyses. Chapter 5 provides experimental mechanical properties of candidate ultra-thin wires, which define the load and safety margins used in the structural design. Chapter 6 investigates the durability and

non-destructive monitoring of composite materials relevant for lightweight detector structures. Finally, Chapter 7 connects these technological developments to the detector-performance motivation by discussing the experimental validation of cluster counting for particle identification. Table 2.1 summarizes the connection between detector-performance requirements and the R&D studies presented in this thesis.

Chapter 3

Mechanical design of the INTREPID drift chamber

The INTREPID drift chamber considered in this research consists of a cylindrical geometry with two endplates joined by a low-mass support structure. The endplates are designed using advanced composite materials and sustain the mechanical tension of more than 3×10^5 wires, in line with the design scale of the IDEA-like ultra-light drift chamber concept for future lepton colliders [8], [29]. Each wire applies a small individual force, but the collective load results in substantial stress on the chamber components, especially on the endplates. A careful mechanical design is therefore essential to ensure structural integrity and to minimize deformations under operating conditions. The mechanical design is driven by two main objectives:

- maximizing transparency in terms of radiation length;
- maximizing mechanical stability by reducing endplate deformations to acceptable limits under the total wire load.

The endplate is a critical structural component and serves several essential functions:

- **Mechanical stability:** it supports and maintains tension on the wires. If the plate is not rigid enough, unwanted motions may compromise tracking accuracy.
- **Alignment and precision:** it fixes the position and alignment of wires. Small misalignment can lead to systematic biases in track reconstruction.
- **Resistance to environmental stresses:** temperature variations can alter wire tension and gas properties, motivating low-CTE and high-stiffness materials.

3.1 Global mechanical architecture and design requirements

The baseline chamber is a full-length (4 m) cylindrical drift chamber segmented into 24 azimuthal sectors. The wire cage comprises 112 coaxial layers, and the wires

are soldered to PCBs inserted between radial spokes, enabling a feed-through-less wiring concept inherited from the IDEA and MEG II drift-chamber design approach [8], [29], [30].

From a mechanical standpoint, wire stability imposes stringent constraints. A 4 m long tungsten wire tensioned at 30 gf bows by $\sim 400\,\mu$m at mid-span; the end-plate and support structure must therefore preserve the wire geometry and limit additional perturbations. At the design level, a representative wire tension of 30 gf corresponds to an overall wire-tension load of order 10 tf per endcap for an IDEA-scale wire count. Distributed over 24 sectors, this gives an average load of about 420 kgf per spoke, for a spoke length of approximately 165 cm. This value is consistent with the refined spoke-level load mapping adopted later in this chapter, where the equivalent integrated load is 444 kgf per spoke. The stay system provides a tension-recovery mechanism and reduces spoke axial deflection; the baseline architecture adopts 15 stays per spoke to improve redundancy and integration margin [8]. Table 3.1 summarizes the baseline mechanical quantities driving the endcap support design.

Table 3.1: Baseline mechanical quantities driving the endcap support design (design-level estimates).

Item	Representative value
Wire length	4 m
Example wire tension	30 gf
Total load per endcap (order)	~ 10 tf
Sectors/spokes per endcap	24
Average load per spoke	$\sim$ 420–440 kgf over 165 cm
Stays per spoke	15

3.1.1 Design requirements and acceptance criteria

The endcap support shall guarantee mechanical integrity and electrostatic stability under wire/PCB tension loads, while preserving detector transparency and assembly feasibility. In this chapter, the acceptance criteria are expressed in terms of:

1. maximum axial (directional) deflection under nominal loading, $\delta_{\max}$;
2. structural margin assessed via an inverse reserve factor, IRF, evaluated with the adopted composite failure criterion and allowable;
3. robustness against integration constraints, with special attention to tolerances and mating with wire PCBs.

Axial deflection target. A total deformation of $\mathcal{O}(0.2\,\text{mm})$ is taken as a practical target for mechanical/electrostatic stability at the design level. This value is intentionally small compared to typical elastic elongations in the wiring operating regime and is compatible with expected wire-by-wire tension variations and operational tolerances. For a representative 20 μm tungsten wire tensioned at 30 gf

($T \simeq 0.294\,\mathrm{N}$), the elastic elongation can be estimated as $\Delta L/L = T/(EA)$. Using $E_{\mathrm{W}} \simeq 400\,\mathrm{GPa}$ and $A = \pi(10\,\mu\mathrm{m})^2$, one obtains $\Delta L/L \simeq 2.3 \times 10^{-3}$, i.e. about 2.3 mm/m or 9–10 mm over a 4 m wire. An axial deformation δ of the support structure therefore modifies the effective wire elongation and induces a relative tension variation of order $\Delta T/T \simeq \delta/\Delta L$. Requiring $\delta \lesssim 0.2\,\mathrm{mm}$ keeps this variation at the percent level, approximately 2% for the representative wire considered here. Since the gravitational sagitta scales approximately as $s \propto 1/T$, this corresponds to a sagitta uncertainty of only a few to ten micrometres, still small compared with the target wire-positioning accuracy. Conversely, millimetre-scale support deformations would produce several-percent tension variations and sagitta shifts of several tens of micrometres, becoming non-negligible in the wire-geometry error budget.

Strength margin target. The structural margin is tracked using IRF, with IRF < 1 indicating compliance with the adopted criterion and allowables. In the preliminary design phase, a representative target IRF ~ 0.6 is used to preserve margin against modelling uncertainties (boundary conditions, contact idealizations, and material property scatter), while leaving room for optimization.

3.2 Mechanical design workflow

The mechanical R&D follows a top-down workflow that starts from the full chamber architecture and progressively introduces dedicated prototypes and higher-fidelity numerical models. The logic is:

1. **Full-chamber mechanical design (CAD-driven):** define the global architecture, interfaces, clearances, insertion paths, datums, and routing envelopes at full scale.

2. **Full-length prototype (system tests):** build a reduced-azimuthal-coverage chamber at full length to validate wiring/assembly/electrostatic limits and technology choices under realistic conditions.

3. **Endcap structural development:** perform early FEM optimization on the spoke–stay load path, which is expected to dominate the local axial compliance of the wire cage.

4. **Model and design maturation:** progressively extend numerical models and prototype validation to the whole chamber (endcaps + barrel panels + joints + boundary compliance) and freeze key parameters based on correlated evidence.

In this thesis chapter, the emphasis is placed on the endplate/endcap support design and its FEM validation at increasing fidelity, culminating in refined single-spoke studies with stays (tension recovery). The full-length prototype is presented as a system-validation step enabling multiple technology and integration tests; subsequent work will extend structural modelling to the complete chamber assembly.

3.3 3D CAD modeling: INTREPID full chamber

A full 3D CAD model of the drift chamber has been developed to consolidate the mechanical architecture and integration envelopes, and to provide consistent interfaces for FEM boundary conditions and load mapping. The model includes endcaps, inner and outer rings, spokes, representative PCB envelopes and mating planes, stay routing volumes and anchoring concepts, and barrel panel segmentation. An overview is shown in Figure 3.1.

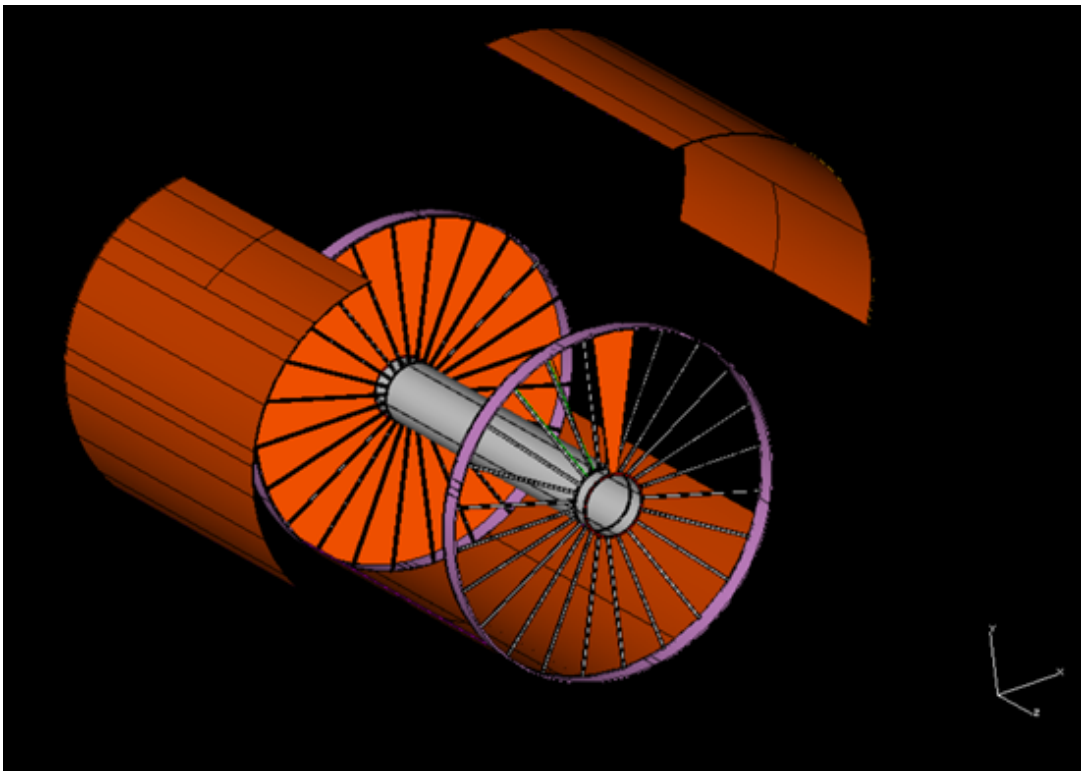

Figure 3.1: Full three-dimensional CAD model of the INTREPID drift chamber used to define the global mechanical architecture, integration envelopes and interfaces for finite-element modelling. The model includes the endcaps, radial spokes, support rings, representative PCB volumes, stay-routing regions and segmented barrel structure.

The initial CAD and FEM studies started from a simplified rectangular spoke cross-section, used as a concept-level geometry to define the main load path, the connection strategy to the inner and outer rings, and the preliminary integration of the wire-supporting elements. Dedicated inserts were then introduced to provide the mechanical interfaces required to anchor the spokes to the inner and outer rings, each manufactured as two assembled halves, as shown in Figure 3.2. Subsequently, the spacers and the PCBs to be inserted between adjacent spokes were modelled. The PCBs were shaped to conform to the spoke geometry and act as positioning references for the wires. The support cables (stays) are anchored directly to the spokes through dedicated attachment features, as shown in Figure 3.3. The figure also highlights the gas distribution system, which is implemented through openings drilled in dedicated spacers.

The support cables are anchored to the outer ring through a tension-recovery

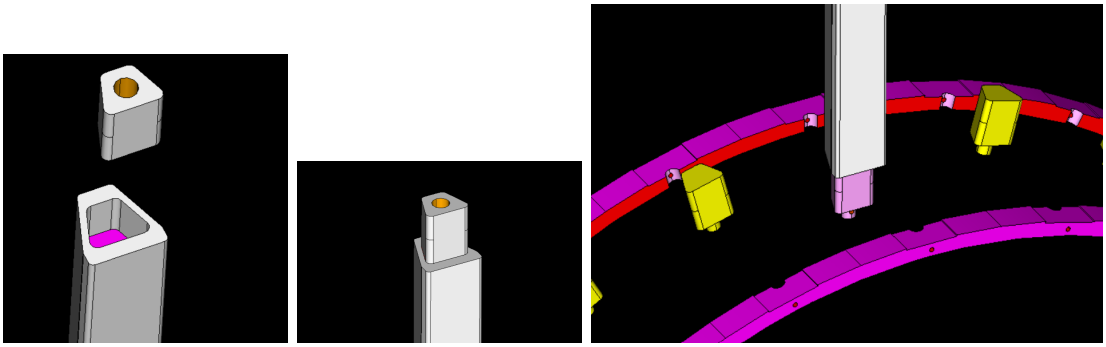

Figure 3.2: CAD details of the spoke-to-ring interfaces. The spoke includes dedicated inserts and mating features for connection to the inner and outer support rings, providing the reference geometry for subsequent endplate assembly.

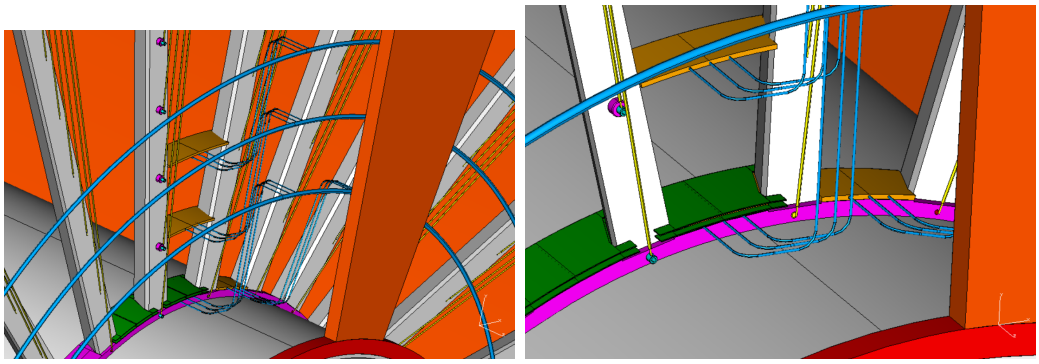

Figure 3.3: CAD details of the endplate integration region, showing PCB stacks, spacers, gas-distribution openings and stay-routing features. These elements define the local mechanical interfaces that must simultaneously provide wire positioning, gas distribution and structural load transfer.

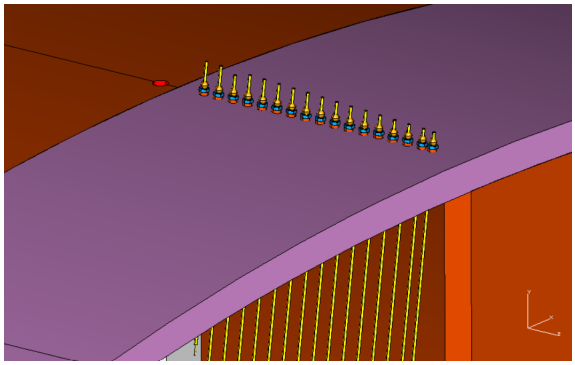

Figure 3.4: CAD representation of the stay anchoring concept at the outer ring. The adjustable stay connection enables controlled tension recovery and provides the mechanical path through which the cumulative wire load is redirected from the radial spokes to the external support structure.

mechanism that allows fine tension adjustments (Figure 3.4).

3.3.1 Full-length prototype

The full-length prototype is introduced to validate, at the 4 m scale, aspects that cannot be fully assessed with local mock-ups or numerical models alone: assembly and wiring procedures, electrostatic stability, material and component choices, and service integration under representative operating conditions. It therefore represents the next baseline step of the mechanical R&D programme. A representative concept includes 3 sectors per endcap, corresponding to 8 spokes total (4 per endcap), an internal ring, a fraction of the outer ring (e.g. $\sim$1/3), and the corresponding cylindrical panel segment.

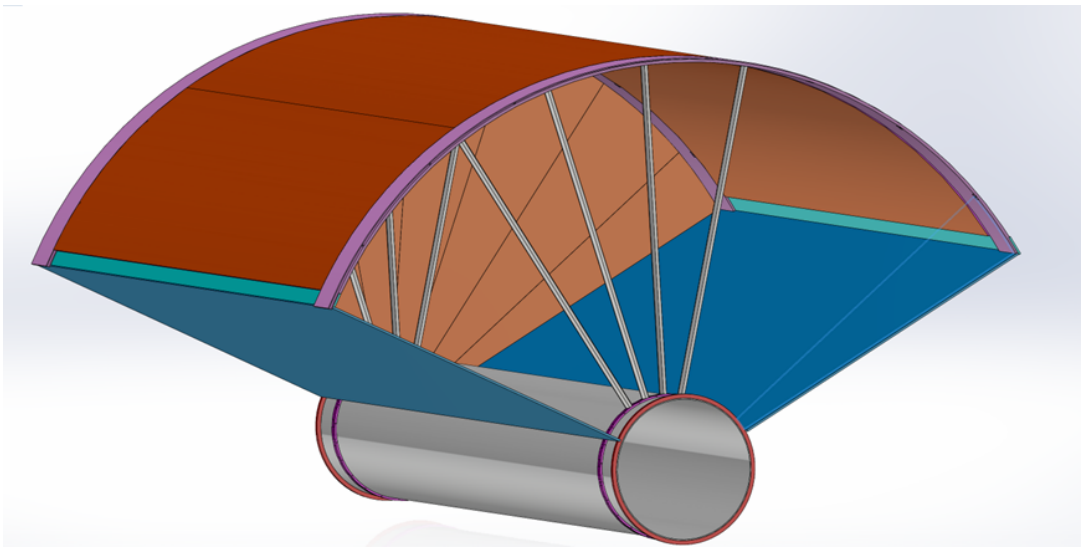

Figure 3.5: CAD concept of the proposed full-length prototype with reduced azimuthal coverage. The prototype preserves the full chamber length while instrumenting a limited number of sectors, allowing wiring, electrostatic stability, gas distribution, mechanical integration and readout concepts to be validated under realistic longitudinal conditions.

System test programme. The full-length prototype is designed to support the following validation tests:

- **Electrostatic stability limits:** check the limits of the electrostatic stability of the wire configuration at full length and at nominal stereo angles.
- **Wire technology scan:** test different wire types (e.g. uncoated Al, carbon monofilaments, Mo sense wires, and different diameters) and related integration procedures:
  - compare wire anchoring procedures to the wire PCBs (soldering, welding, gluing, crimping, ...);
  - test different materials and production procedures for spokes, stays, support structures and spacers;
  - assess compatibility of proposed materials with drift chamber operation (outgassing, aging, creeping, ...).
- **Wire tension recovery validation:** validate the concept of the wire-tension recovery scheme with respect to tolerances on wire positions; optimize the layout of the wire PCBs (sense/field/guard) according to the anchoring procedures, with the aim of minimizing the endplate total material budget.
- **Wiring strategy:** starting from the concepts implemented in the MEG II DCH robot, optimize the wiring strategy accounting for 4 m long wires arranged in multi-wire layers [30], [31].
- **Assembly scheme:** define and validate the assembly scheme (with respect to mechanical tolerances) of the multi-wire layers on the endplates; define the front-end cards channel multiplicity and their location (including possible cooling needs).
- **HV and signal distribution:** optimize the high-voltage and signal distribution (cables and connectors).
- **Readout chain:** test performance of different versions of front-end, digitization and acquisition chain.

3.4 Mechanical Design and Finite Element Analyses of the INTREPID Drift Chamber Endplate

In line with the mechanical strategy of the IDEA drift chamber, the INTREPID end cap is designed as a composite load-bearing structure consisting of inner and outer CFRP rings connected by radial spokes. [8], [29]. These spokes support the wire-bearing PCBs and transfer the loads generated by wire tension to the external structure, which in turn interfaces mechanically with the cylindrical barrel panels forming the sealed gas vessel. While the full-length prototype addresses system tests (electrostatics, wiring, integration, services, and readout), the dominant contributor

to the mechanical stability of the wire cage is the endplate/endcap support. In particular, the spoke is the primary load-carrying element that transfers the distributed wire/PCB tension to the rings and to the external structure; its axial deformation directly affects wire-position stability.

For this reason, the early structural optimization reported in this chapter concentrates on endplate FEM studies and progressively transitions to refined single-spoke models including the tension-recovery stay system. Subsequent activities will extend the validated modelling approach to the full chamber, including barrel panels, joint compliance, and global boundary conditions.

3.4.1 Preliminary design and modelling

A preliminary mechanical model of the endplate was developed to validate the overall structural concept and assess the feasibility of composite materials for the main load-bearing components.

A finite element model was generated in `Ansys Workbench` using `Composite PrepPost (ACP)`, i.e. the Workbench-integrated pre/post-processing environment for layered composite structures, which allows the definition and visualization of complex lay-ups and their transfer to structural analysis workflows [32], [33]. The general workflow is illustrated in Figure 3.6.

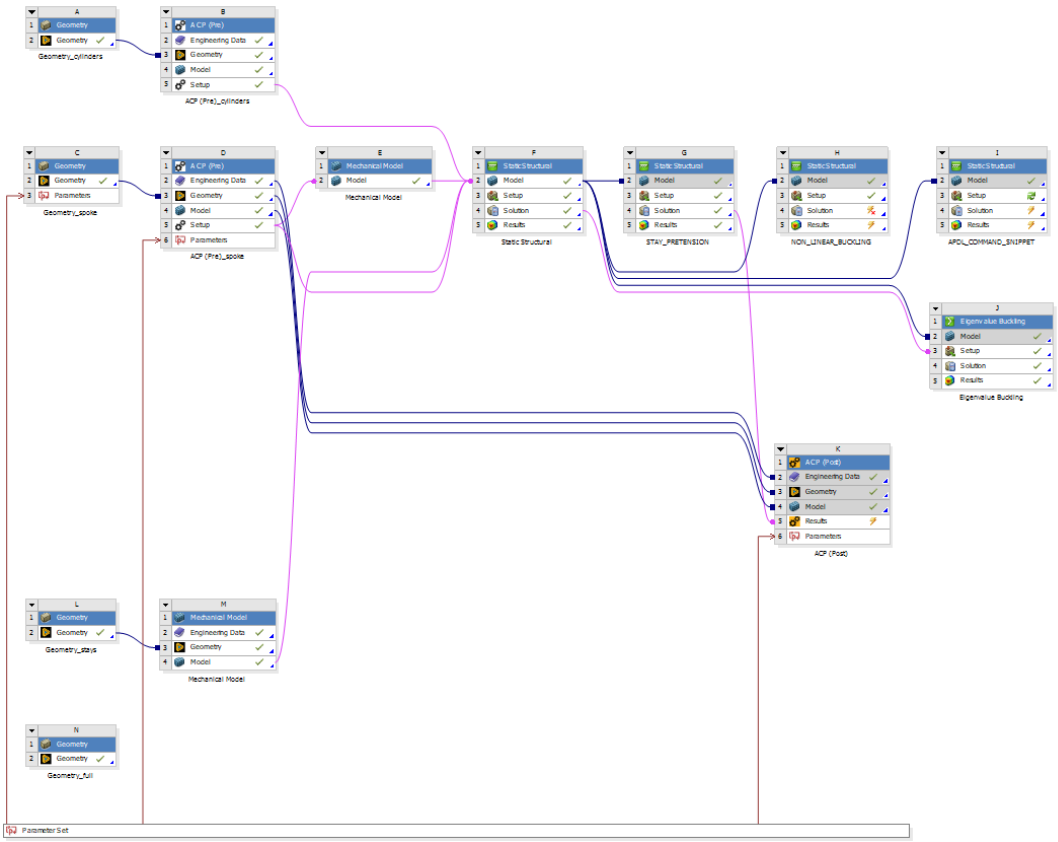

Figure 3.6: Finite-element modelling workflow adopted in ANSYS Workbench with Composite PrepPost (ACP). The workflow links composite lay-up definition, mesh generation, structural analysis and post-processing of deformation, stress and composite failure indices.

Within this framework, the cylindrical walls and the spokes were generated in ACP-Pre. The corresponding meshes are shown in Figure 3.7. Each spoke consisted of 84 plies of an Epoxy/Carbon UD 230 GPa prepreg with ply thickness 0.2 mm. These layers were distributed across four solid elements through the thickness to improve aspect ratio and numerical accuracy (Figure 3.7, right).

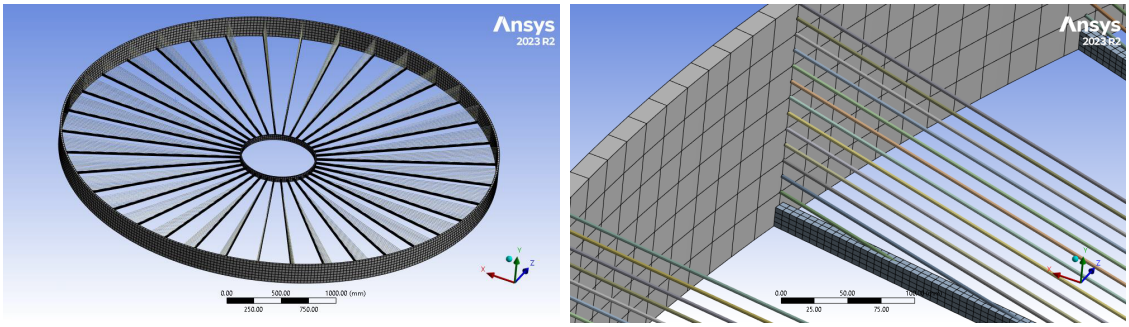

Figure 3.7: Finite-element mesh of the preliminary endplate model. Left: full endplate mesh including rings, spokes and stay geometry. Right: mesh detail of a representative spoke, where the composite lay-up is discretized through the thickness to improve the accuracy of stress and deformation predictions.

The inner and outer rings were modeled using layered shell elements, with mapped quadrilateral meshes where possible. The inner ring consisted of 50 unidirectional plies (fibers at 0° in the circumferential direction), while the outer ring adopted a similar lay-up with 80 plies. The lay-up adopted here is intentionally simplified for concept-level structural assessment. It is not meant to represent the final manufacturing solution, which will require a balanced and process-compatible laminate sequence accounting for fabrication constraints, handling, and out-of-plane stability.

The geometry of the tension rods (stays) was included in the same model, and a circular array was used to replicate the baseline 24 spokes around the full 360° extent of the endplate. The outer ring was constrained along the chamber-side circumference using a fixed support.

Load mapping (concept level). A radially varying pressure load, ranging from 0 to 0.36 MPa, was applied to the spokes to represent the distributed load generated by the increasing radial contribution of the wire tension along the spoke length (Figure 3.8, top). This mapping was adopted at the concept stage as a conservative screening load to study deformation patterns and the qualitative benefit of pretension.

Stay pretension (concept level). An additional configuration included pretensioning of the stays, simulated via thermal contraction by imposing a controlled temperature drop (Figure 3.8, bottom). Stays were initially assigned a uniform temperature and cooled down to different target temperatures corresponding to the pretension levels.

To complement the static analysis, a nonlinear buckling study was performed to qualitatively investigate possible local instability phenomena in the outer cylindrical wall. Given the limited modeled extension, the results were used mainly for

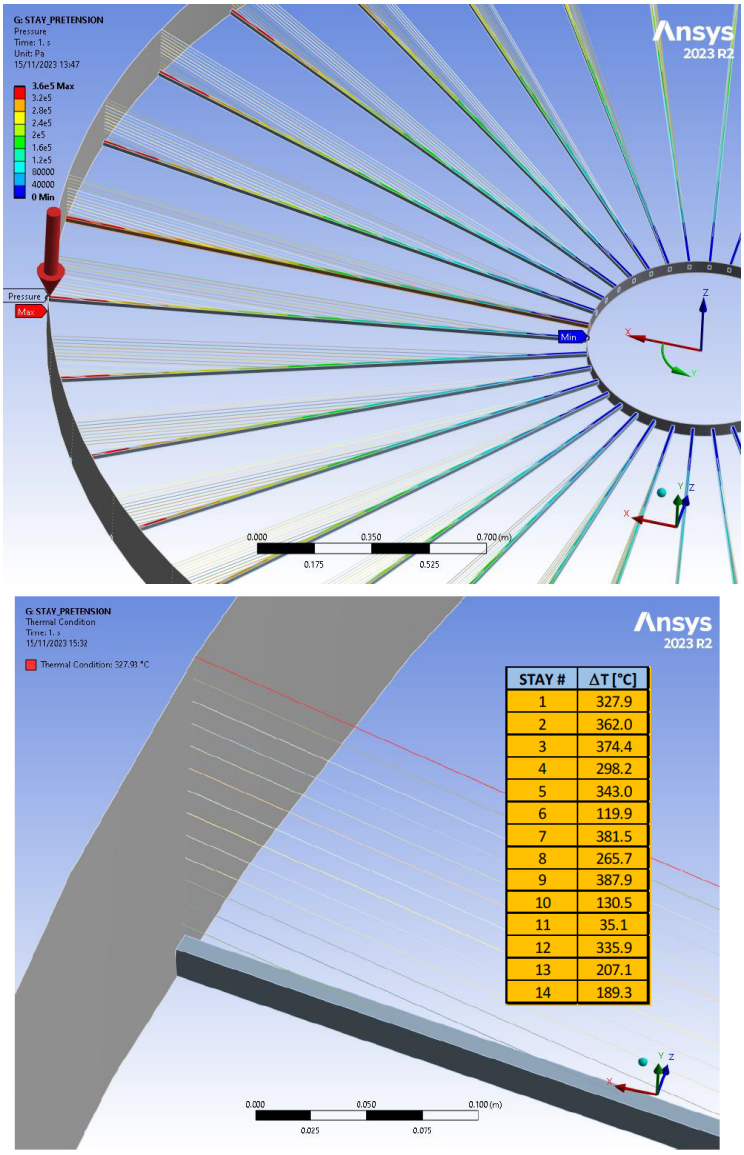

STAY #	ΔT [°C]
1	327.9
2	362.0
3	374.4
4	298.2
5	343.0
6	119.9
7	381.5
8	265.7
9	387.9
10	130.5
11	35.1
12	335.9
13	207.1
14	189.3

Figure 3.8: Concept-level load and pretension modelling adopted in the preliminary endplate FEM analysis. Top: radially varying equivalent pressure applied to the spokes to represent the distributed wire-tension load. Bottom: thermal contraction applied to the stays to simulate pretension and evaluate its effect on endplate deformation.

validation and numerical verification. ACP-Post was configured for advanced post-processing, including failure indices such as First Ply Failure and IRF-like metrics.

Preliminary results (global endcap trends)

The structural performance of the endplate was evaluated under two configurations: (i) without stay pretension and (ii) with stay pretension simulated through thermal contraction. Key outputs were maximum axial deformation, principal stress range in spokes, and an inverse reserve factor (IRF) computed here according to a Maximum Stress/Strain criterion.

Table 3.2: Summary of the main results obtained from the concept-level endcap FEM analysis.

Config.	**Max Axial Deform. [mm]**	**Stress Range [MPa]**	**IRF**
Without pretens.	14.0	-321 / $+176$	0.75
With pretens.	3.6	-166 / $+75$	0.70

In the non-pretensioned condition (Figure 3.9), the maximum axial deformation reached about 14 mm, mainly along the chamber axis. Stresses ranged from -321 MPa (compression) to $+176$ MPa (tension), highlighting bending effects. With pretension (Figure 3.10), the maximum deflection decreased to 3.6 mm and stresses were homogenized (-166 MPa to $+75$ MPa), with IRF improving slightly.

3.4.2 Advanced cross-section design (manufacturing convergence)

The second phase focused on redefining the spoke geometry and lay-up to improve stiffness and manufacturability while maintaining an ultra-low material budget.

Spoke cross-section development

Starting from the preliminary rectangular spoke, a double-T cross-section was proposed as a refined structural solution. This geometry increases bending and torsional stiffness while providing well-defined mounting surfaces for the PCBs. This geometry provides higher bending and torsional rigidity and well-defined mounting surfaces for the PCBs.

The cross-section is composed of a carbon–epoxy rectangular core (20×10 mm) surrounded by CFRP skins with five unidirectional plies $[90/0/90/+45/-45]$. Two additional stacks of 23 plies ($0°$) are placed on the upper and lower flanges to increase bending stiffness. The total cross-sectional area is approximately 670 mm^2.

Spokes can be manufactured using an interlocking mold, with the core serving as a removable insert and skins laid up from CFRP prepreg plies. This approach allows fiber orientations to be optimized for axial and torsional loads while preserving mating tolerances for PCB insertion.

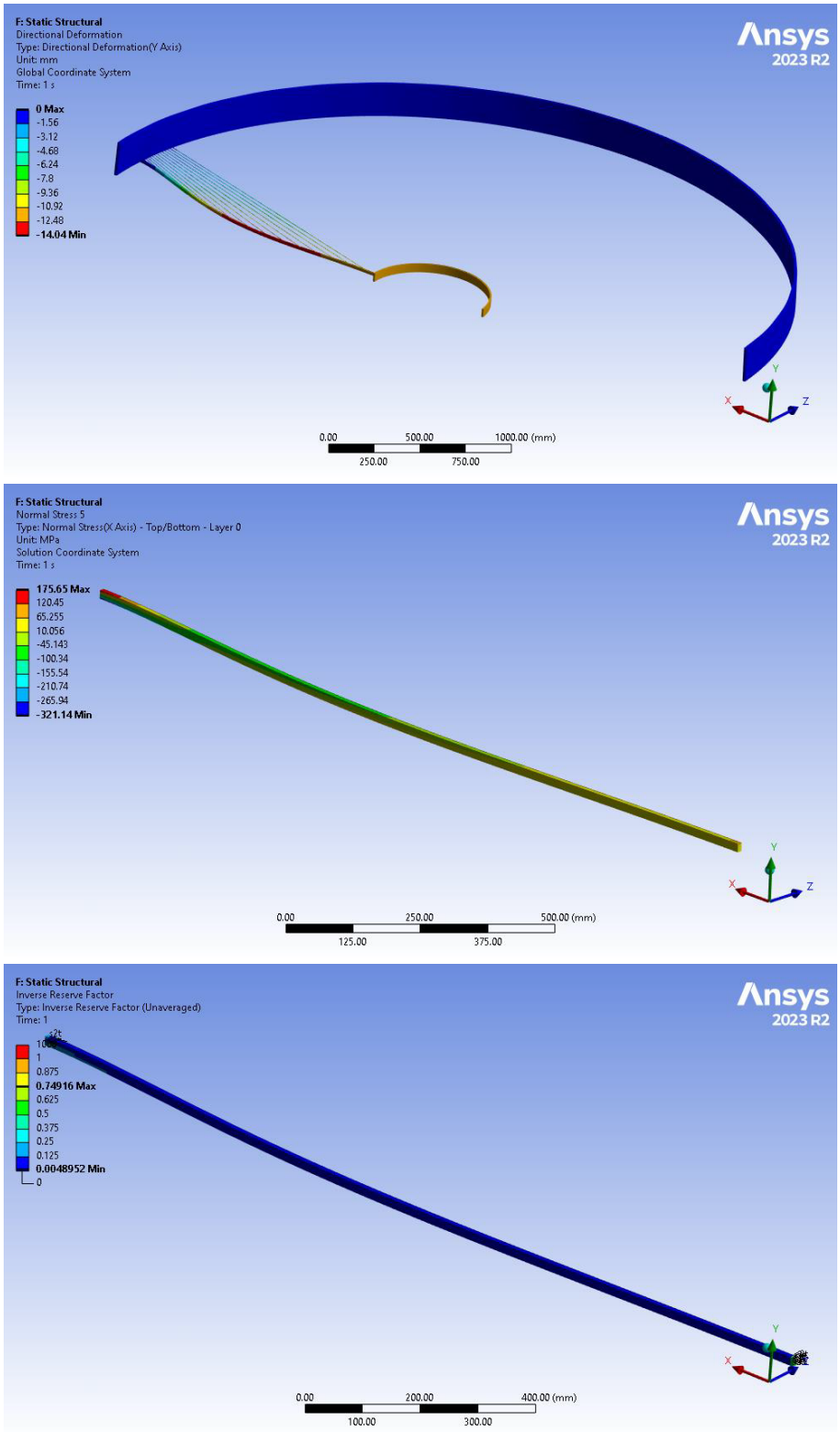

Figure 3.9: Preliminary full-endplate FEM results without stay pretension. From top to bottom: directional deformation along the chamber axis, directional stress along the spoke axis, and inverse reserve factor evaluated with the adopted Maximum Stress/Strain criterion. The large axial deformation identifies the need for an active tension-recovery strategy.

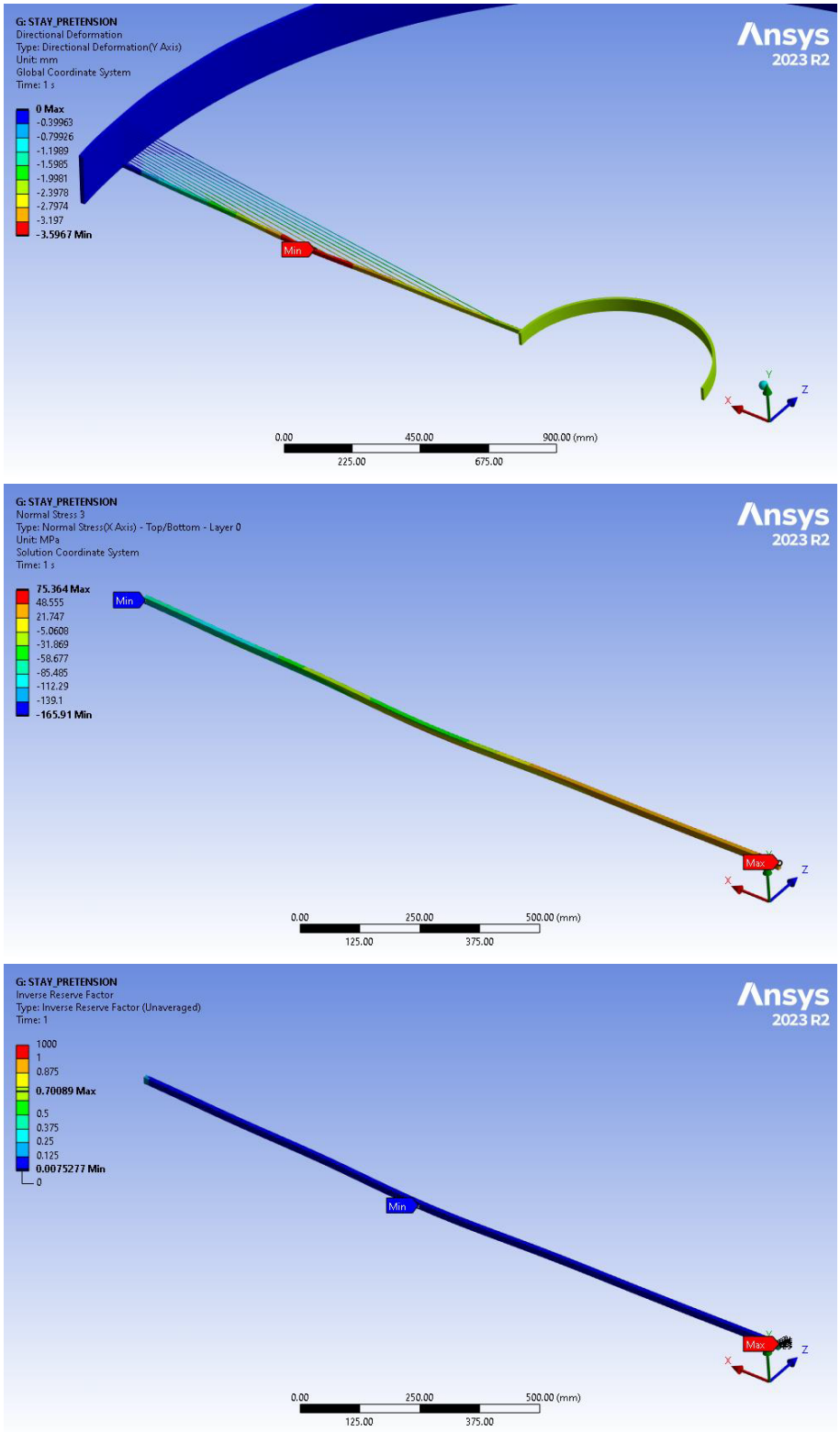

Figure 3.10: Preliminary full-endplate FEM results with stay pretension introduced through thermal contraction. From top to bottom: axial directional deformation, spoke-axis directional stress and inverse reserve factor. The comparison with the non-pretensioned case shows the ability of the stay system to reduce deformation and homogenize the stress distribution.

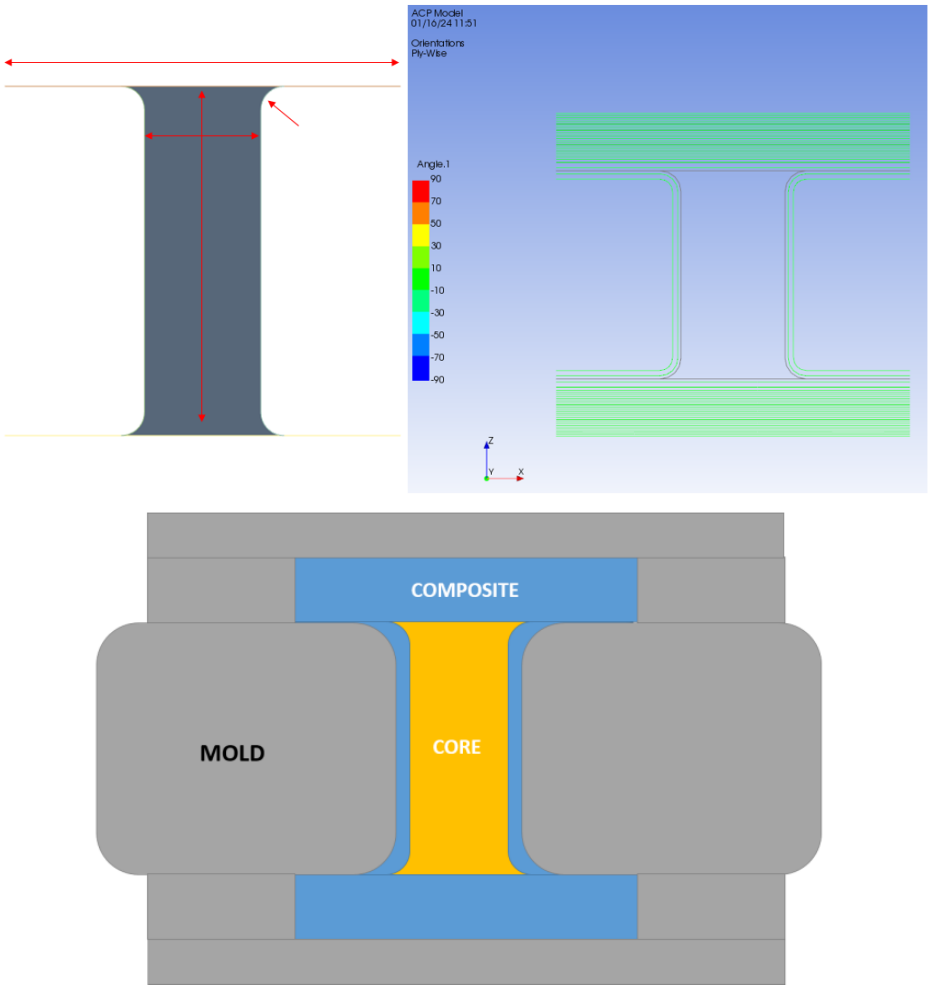

Figure 3.11: Refined double-T spoke concept developed for improved stiffness and manufacturability. Top: cross-section and composite ply distribution, including the central carbon–epoxy core, skin plies and additional unidirectional flange reinforcement. Bottom: interlocking-mold concept proposed for manufacturing and dimensional control of the composite spoke.

Refined FE model and analysis setup (single-spoke level)

A detailed FE model of a single spoke and attached portions of the inner and outer rings was developed in `ANSYS Workbench 2023R2` (Figure 3.12, top). The spoke skins were meshed with `SHELL181` elements, the core with `SOLID185`, and bonded contact conditions were used between interfaces.

Material properties were taken from the ANSYS composite library:

- Epoxy–Carbon UD (395 GPa) for skins,
- Epoxy–Carbon UD (230 GPa) for core,
- Aluminum alloy for walls (used for convenience in this phase).

Updated load mapping (refined model). At spoke level, the wire-tension load was represented by a radially varying pressure distribution with a peak value of 0.159 MPa, corresponding to an equivalent total load of 444 kgf per spoke (Figure 3.12, bottom). This updated mapping is adopted as the quantitative basis for design decisions in the refined stage, while the earlier 0.36 MPa mapping is treated as a conservative concept-level screening load.

Boundary conditions locked circumferential displacements at the wall edges and fixed axial motion at the bottom of the outer wall. In the refined spoke–level model, the inner ring was intentionally left free in the axial direction, while the outer support region provided the reference constraint for the system. This choice reflects the intended load-transfer concept of the endplate, in which the spoke–stay assembly acts as a tension-recovery structure: the inner region is not rigidly clamped, but is supported through the stays and the spoke, in a way conceptually analogous to a suspended system.

Results: spoke–only vs spoke–stay system

Two static structural analyses were carried out. The first model excluded stays to quantify intrinsic compliance under wire load; the second included the estimated stay forces to evaluate the effectiveness of the tension-recovery scheme.

Without stays. The maximum deformation along the chamber axis was 73mm (Figure 3.13, top). A local failure index exceeded unity near the outer wall (reported as IRF$\simeq$1.43 using a Puck-based criterion in this stage), indicating an unacceptable configuration without tension recovery. The no-stay configuration is not intended as a realistic detector option. It is used as a limiting case to quantify the intrinsic compliance of the spoke and to isolate the mechanical role of the stay system.

With stays. Fifteen stays were introduced, applying tensile forces between 50 and 500N each. The maximum deformation reduced to 0.19mm (Figure 3.13, bottom), with IRF ≈ 0.6 and stresses within allowable ranges, confirming the effectiveness of the tension-recovery concept at the refined stage.

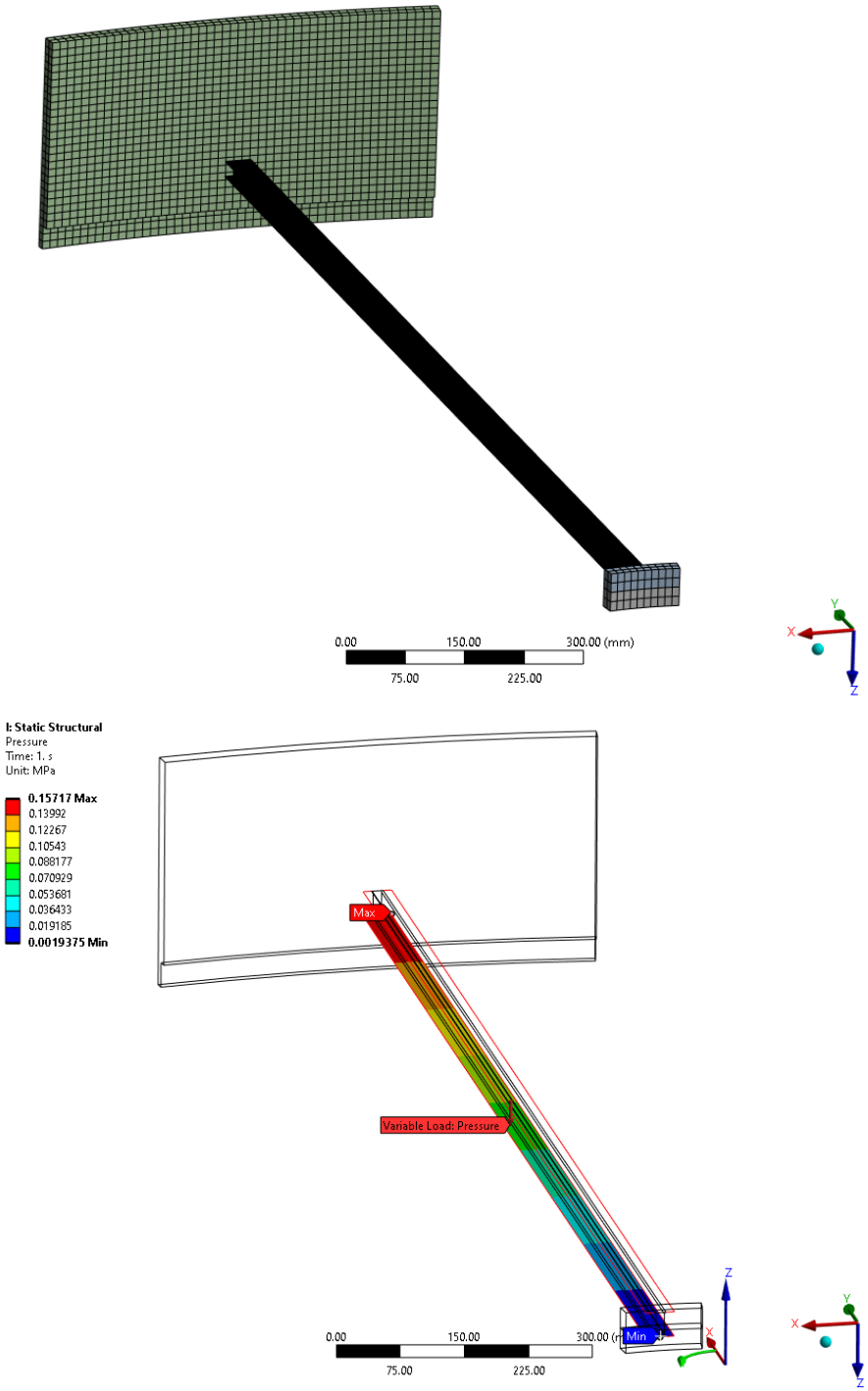

Figure 3.12: Refined single-spoke finite-element model. Top: spoke model with attached portions of the inner and outer rings and bonded composite interfaces. Bottom: updated radially varying pressure distribution applied to the spoke to reproduce the equivalent integrated wire load in the refined design stage.

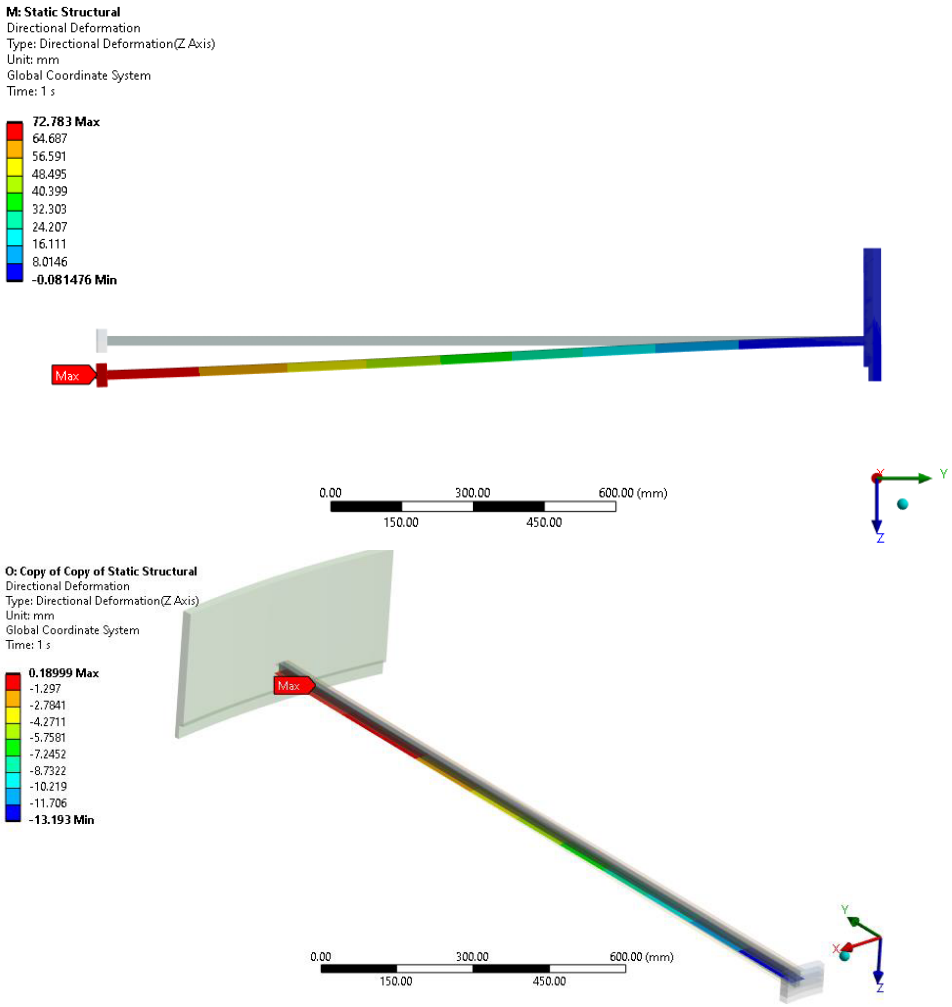

Figure 3.13: Directional axial deformation of the refined single-spoke FEM model under the equivalent wire load. Top: configuration without stays, used as a limiting compliance case rather than as a realistic detector option. Bottom: configuration with 15 tension-recovery stays, showing the reduction of the maximum axial deformation to approximately 0.19 mm.

The deformation fields obtained in the preliminary endplate model and in the refined single-spoke model are not expected to coincide point by point, since the two analyses address different geometrical levels and use different load-transfer representations. The former is a concept-level model of the endplate architecture, based on a conservative homogenized pressure mapping and stay pretension introduced through thermal contraction, whereas the latter is a refined spoke–level model with an updated pressure distribution and discrete stay forces. For this reason, the location of the maximum deformation is not directly comparable between the two cases. It should be noted that the IRF values reported for the preliminary and refined models are not meant to be compared quantitatively, since different geometrical idealizations, load mappings and composite failure criteria were adopted. They are used here as stage-dependent indicators of structural margin.

Model fidelity and limitations with respect to the full detector

The refined single-spoke model should be interpreted as a local design validation of the tension-recovery concept, rather than as a complete prediction of the final detector deformation. Compared with the real detector, the model includes the dominant local load path between the wire-bearing spoke and the stay system, but it does not yet include the full azimuthal coupling among the 24 sectors, the compliance of the complete barrel structure, the detailed stiffness of all PCB/spacer stacks, the nonlinear behaviour of adhesive joints, manufacturing tolerances, thermal and hygroscopic strains, long-term creep, or possible dynamic effects during operation.

The equivalent pressure used to represent the wire load is therefore a design-level load mapping. It reproduces the integrated load acting on the spoke, but it cannot describe local force concentrations associated with individual wire anchoring points. Similarly, the stay forces are introduced as prescribed tensile loads, while in the real chamber they will depend on the stiffness and adjustment strategy of the complete endcap assembly.

Within these assumptions, the predicted axial deformation of about 0.19 mm demonstrates that the stay-based recovery system can reduce the spoke compliance to the required scale. However, this value should be regarded as an optimistic local estimate. A full-detector model including rings, barrel panels, PCB stacks, joints and realistic boundary compliance will be required before freezing the mechanical design.

Design consolidation and next refinements

The refined analysis confirms that the double-T section meets stiffness and strength targets while keeping the material budget extremely low. Further improvements will involve:

- tuning stay pretension to further reduce deflection margins and improve robustness;
- optimizing flange width and mating surfaces to simplify PCB mounting and tolerance closure;

- defining the assembly strategy between spokes and rings (e.g. adhesive bonding on the inner ring and mechanical support shoulders on the outer ring);
- refining joints and interfaces and extending the FE model fidelity in the prototype phase (e.g. 3D solid representation of selected composite regions where needed).

3.4.3 Conclusions

The mechanical concept presented in this chapter—derived from the FCC-ee IDEA design studies [8], [29]—demonstrates the feasibility of an ultra-light endcap support based on composite spokes, CFRP inner/outer rings, and a system of adjustable stays enabling wire-tension recovery. In the preliminary validation stage reported here, a double-T spoke cross-section was adopted as a representative and manufacturable solution to quantify the effectiveness of the tension-recovery scheme. With PCBs inserted radially between adjacent spokes and acting as wire-position references, the refined single-spoke FEM predicts a maximum axial deformation of approximately 0.2 mm under the full equivalent wire load. This level of deformation is compatible with both mechanical tolerances and electrostatic stability requirements, while preserving a minimal material budget. These results should be regarded as a first design proof rather than a final optimization. The double-T spoke was used as a refined manufacturable section to demonstrate the effectiveness of the stay-based tension-recovery scheme after the initial rectangular concept. Current work is now moving toward an improved trapezoidal spoke geometry, with the aim of better matching the full CAD integration constraints, refining load transfer to the rings, and improving the realism of the spoke–PCB and spoke–ring interfaces. The next steps will consolidate the key design parameters (spoke shape, composite lay-up, joints, and stay pretensioning strategy) and will validate the predicted performance through dedicated prototype tests, ultimately extending the correlated modelling approach from the single-spoke level to the full chamber assembly. From the detector-performance point of view, the relevance of this result is that an axial deformation at the 0.2 mm level produces only a percent-level variation of the nominal wire tension and therefore a sagitta uncertainty of the order of a few micrometres. This is small compared with the target wire-positioning accuracy and with the intrinsic single-hit resolution. On the contrary, millimetre-scale deformations would propagate into the electrostatic cell geometry and into the time-to-distance calibration, becoming a direct source of systematic tracking error.

Chapter 4

The CEPC drift chamber

INTREPID was originally proposed by the Italian community as the drift-chamber solution for the IDEA detector at FCC-ee at CERN. However, the same detector concept can also be adapted to other future lepton-collider facilities, including CEPC. In the CEPC framework, the drift chamber is introduced within the silicon tracking system to improve charged-particle identification and to preserve robust tracking performance under high-luminosity operating conditions. In particular, cluster-counting techniques offer the possibility of significantly better resolution than conventional dE/dx-based methods. For this reason, the study of drift-chamber solutions for CEPC is closely connected with the development of high-precision simulation and reconstruction tools for cluster counting, in continuity with the R&D programme carried out for INTREPID in the FCC-ee/IDEA framework.

The work presented in this chapter is the result of a research period spent at the Institute of High Energy Physics (IHEP) in Beijing, carried out within a mutual-support collaboration on detector R&D for future lepton colliders. The mechanical studies presented here were developed to support the synergy between the FCC-ee and CEPC detector communities. Within this collaborative framework, the original contribution of this thesis concerns the mechanical modelling and finite-element evaluation of CEPC endcap solutions, with particular attention to thickness optimization and to the comparison between the stepped baseline geometry and a proposed concave endcap configuration.

4.1 An alternative drift chamber proposal

In contrast to the ultra-light IDEA concept developed for FCC-ee, the drift chamber proposed for CEPC adopts a more conventional mechanical architecture, consisting of a lightweight cylindrical barrel coupled to two metallic endcaps [34]. The barrel is based on a high-modulus carbon-fiber (CF) composite structure composed of eight longitudinal hollow beams and eight annular beams, with a total length of 5.8 m and an outer diameter of 3.6 m, corresponding to an outer radius of 1.8 m. The initial reference design considered an aluminum endcap thickness in the 20–25 mm range. In the present optimization study, thicknesses between 15 and 25 mm were analysed in order to identify the minimum value compatible with the required stiffness. The endcaps are perforated with a regular pattern of holes to accommodate the feed-

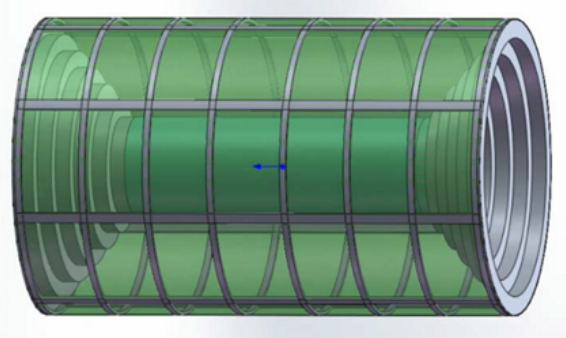

Figure 4.1: Reference mechanical concept of the CEPC drift chamber. The detector consists of a carbon-fiber barrel structure closed by two aluminum endcaps with a stepped profile and a regular hole pattern for wire installation and tensioning.

throughs used for wire installation and tensioning. A general view of this design is shown in Figure 4.1. The adoption of metallic endplates simplifies machining, wire assembly, and alignment procedures while ensuring high stiffness, structural robustness, and long-term mechanical reliability. By comparison, the FCC-ee drift chamber is characterized by a larger active radius of 2.0 m and by a more aggressive low-mass design philosophy. Although both detectors make use of CF-based barrel structures, the principal distinction lies in the endcap concept: the FCC-ee solution is based on composite endcaps, for instance carbon-fiber skins combined with lightweight core materials, whereas the CEPC design relies on solid aluminum plates. This difference has a direct impact on the material budget (see 2.5.5) and, consequently, on the expected detector performance. For the FCC-ee IDEA drift chamber, the overall material budget amounts to about $1.6\%\,X_0$ in the radial direction through the barrel region, including the contributions from the inner and outer walls, the gas mixture, and the wires. In the forward direction, where wire supports, gas containment, front-end electronics, cables, and services also contribute, the total material budget reaches about $5.0\%\,X_0$. In the CEPC configuration, the heavier mechanical implementation leads to a substantially larger material budget, of the order of $5\%\,X_0$ in the barrel region and up to $20\%\,X_0$ in the forward region. Therefore, while the CEPC chamber benefits from a mechanically conservative and technologically mature design, it does so at the cost of a significantly reduced transparency with respect to the FCC-ee concept.

These two approaches reflect different engineering priorities. In the FCC-ee case, the mechanical design is driven by the need to minimize multiple scattering and preserve the excellent tracking and particle-identification capabilities of the detector. This objective requires extensive FEM-based optimization in order to achieve adequate stiffness with minimal mass, together with advanced composite manufacturing techniques and high-precision dimensional control. In the CEPC case, by contrast, the use of aluminum endcaps leads to a more conventional and inherently robust solution, characterized by lower implementation risk and simpler production routes based on established machining and assembly procedures.

From the physics perspective, the lower material budget of the FCC-ee chamber is expected to provide clear advantages in terms of momentum resolution and particle identification, owing to the reduction of multiple scattering and the improved

preservation of both dE/dx and cluster-counting information. The CEPC design, although less favorable from the standpoint of material transparency, offers a reliable and comparatively low-risk solution with strong mechanical stability. The comparison between the two detectors therefore highlights the classical trade-off between structural innovation and manufacturing simplicity.

Table 4.1 summarizes the main differences between the FCC-ee and CEPC drift chamber concepts.

Aspect	**FCC-ee drift chamber**	**CEPC drift chamber**
Outer radius	2.0 m	1.8 m
Barrel material	CF composite (ultra-light concept)	CF composite
Endcap material	Composite (e.g. CF + foam core)	Aluminum
Material budget (barrel region)	$\sim 1.6\% X_0$	$\sim 5\% X_0$
Material budget (forward region)	$\sim 5\% X_0$	$\sim 20\% X_0$
Manufacturability	Complex, R&D intensive	Conventional, low risk

Table 4.1: Comparison of the main design features of the FCC-ee and CEPC drift chamber concepts.

In summary, although the FCC-ee and CEPC drift chambers are conceived to fulfill similar tracking functions, they embody substantially different structural strategies. The FCC-ee option represents an optimized ultra-light solution, in which composite materials and FEM-driven design are exploited to reduce the radiation length as much as possible. The CEPC chamber, on the other hand, adopts a more traditional and conservative architecture, privileging robustness, reliability, and ease of construction. The following sections present the mechanical studies carried out for the CEPC endcap and discuss their implications for the comparison with the INTREPID concept.

4.2 The Drift Chamber for CEPC

Having explored the FCC drift chamber in detail, we now transition to the CEPC drift chamber, following the evolution of design principles and highlighting the specific adaptations that reflect the unique requirements of the CEPC experiment.

Figure 4.2 illustrates the conceptual detector and provides an overview of its sub-detectors [35]. The drift chamber is a crucial element of this design, enhancing track reconstruction performance and enabling high-precision particle identification (PID) through the cluster counting method.

In our case study, the drift chamber, proposed for a future experiment at CEPC, has a very large structure with a cylindrical geometry formed by a barrel body 5.8 meters long and two endcaps with a diameter of 3.6 meters. More than 100 thousand wires are connected to the two endcaps, providing a load of about 10 tons.

The idea of this study is to optimize the thickness and geometry of the endplate to have a structure that is both resistant to the large tensions involved and light enough to reduce multiple scattering.

The endplate combines several functions that are mechanically and experimentally coupled: it supports the cumulative wire tension, defines the wire-position

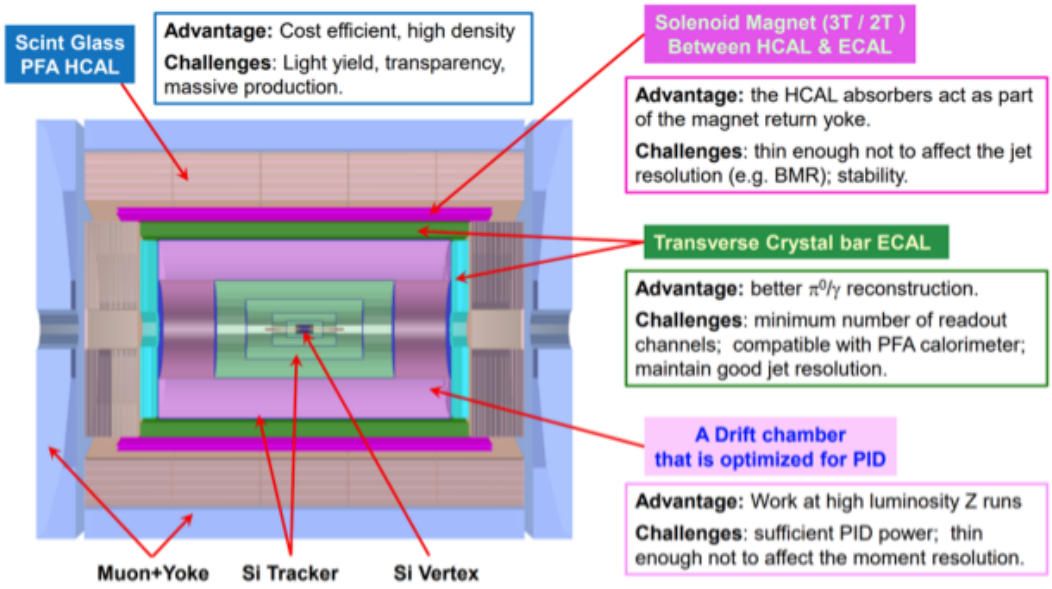

Figure 4.2: Conceptual layout of the CEPC detector, showing the main tracking and calorimeter subsystems. The drift chamber is integrated within the tracking system to enhance charged-particle identification through ionization and cluster-counting measurements.

reference system, contributes to gas sealing, and must remain dimensionally stable under environmental variations. Unlike the INTREPID composite concept, the CEPC solution adopts aluminum endcaps, trading a higher forward material budget for greater stiffness, simpler machining and lower integration risk. The optimization discussed below therefore aims at reducing the endplate thickness and improving its geometry without compromising deformation control under realistic wire loads.

In this chapter, we will provide a detailed description of the drift chamber, with the various preliminary studies with finite element analysis that mark a starting point for the optimization of the proposed endplate. Then we will analyze a study as a function of the thickness of the endplate and the evaluation of the number of layers of wires to determine the mechanical stability of the endplate. Lastly, we will see the proposal for a new shape of the endplate that will improve its mechanical performance.

4.3 The drift chamber for CEPC: mechanical design

The mechanical structure of the drift chamber for the Circular Electron-Positron Collider (CEPC) is typically cylindrical to maximize the active tracking volume around the interaction point, where particles are produced. This geometry allows particles to traverse multiple layers of detection, improving spatial resolution and momentum reconstruction.

COMPOSITE PROPERTIES

PROPERTY	ENGLISH	METRIC	METHOD
Tensile Strength*	293 ksi	2,020 MPa	ASTM D-3039
Tensile Modulus*	49 Msi	338 GPa	ASTM D-3039
Tensile Strain		0.61%	ASTM D-3039
Compressive Strength*	129 ksi	890 MPa	SACMA SRM 1R-94
Flexural Strength*	171 ksi	1,180 MPa	ASTM D-790
Flexural Modulus*	40 Msi	274 GPa	ASTM D-790
ILSS	11 ksi	73.2 MPa	SACMA SRM 8R-94
In Plain Shear Strength	10 ksi	68 MPa	ASTM D-3518
90° Tensile Strength	5 ksi	37 MPa	ASTM D-3039

Figure 4.3: Carbon-fiber material configuration adopted for the CEPC drift-chamber barrel support. The figure illustrates the layered composite structure and the main material parameters used to define the mechanical model of the cylindrical frame.

4.3.1 Overall design

The structural design of the drift chamber comprises a lightweight cylindrical barrel constructed from composite materials and two aluminum endcaps. The barrel consists of a carbon fiber (CF) structure based on M55J High Modulus fibers, featuring eight longitudinal hollow beams and eight annular beams, with a total length of $5.8\,m$ and an external diameter of $3.6\,m$. Figure 4.3 shows the characteristics of the composite material. The CF frame walls are $3.2\,mm$ thick and consist of 16 composite layers with fibers having alternating directions for each layer ($200\,\mu m$ per layer). The cross-sectional dimensions of the longitudinal beams are $125\,mm \times 40\,mm$, and those of the annular beams are $80\,mm \times 40\,mm$, with each beam contributing approximately $78\,kg$ and $111\,kg$ of mass respectively. A detailed view of the layers that make up the barrel is shown in the Figure 4.4. To minimize the material budget while maintaining gas-tightness, an inner and outer CF cylinders are designed with minimal wall thicknesses of $200\,\mu$m and $300\,\mu$m, corresponding to 0.08% and 0.13% of a radiation length (X_0), respectively. Each endcap is fabricated from a $25\,mm$ thick aluminum disk with a stepped profile, extending inward to form a central cylindrical section with an inner diameter of $1.2\,m$. The material used is a 7075 Aluminum with a Yield strength of $505\,MPa$, Young's modulus of $71.7\,GPa$, and Poisson's ratio of 0.33. Figure 4.5 presents a schematic view of the cross-sectional profile of one quarter of the drift chamber, highlighting the main structural components and relevant geometrical parameters. The overall material contribution of the mechanical structure, including cables and endplates, remains within acceptable limits for tracking detectors in high-energy physics experiments. The complete mechanical structure has a total estimated mass of approximately $1100\,kg$.

4.3.2 Wire tension

Wire tension represents one of the dominant mechanical loads in the present design. The chamber accommodates 26,483 drift cells distributed across the four endcap steps, with sense wires made of gold-coated tungsten ($20\,\mu$m diameter) and field

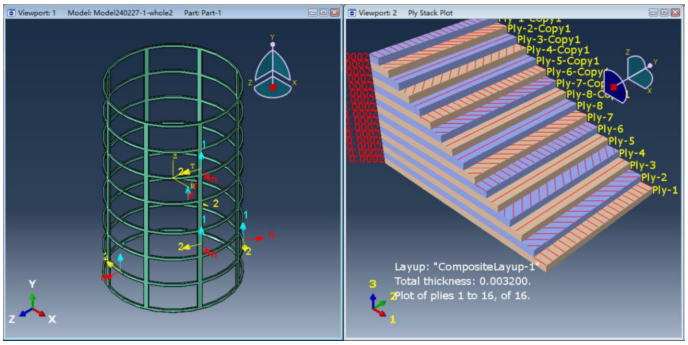

Figure 4.4: CEPC drift-chamber barrel structure and composite lay-up detail. The barrel is composed of longitudinal and annular carbon-fiber beams together with thin inner and outer carbon-fiber cylinders, providing a lightweight support for the large wire volume.

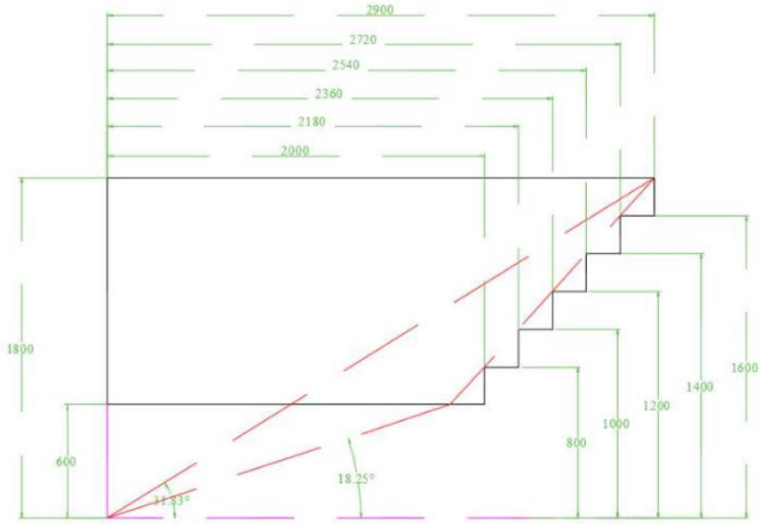

Figure 4.5: Quarter-section profile of the CEPC drift chamber with main geometrical dimensions. The drawing shows the barrel envelope, stepped aluminum endcap, central opening and radial regions used for wire anchoring and mechanical optimization.

wires made of gold-coated aluminum (60 μm diameter). Depending on the step, the single-wire tension ranges from 41.75 g to 86.92 g for sense wires and from 64.14 g to 133.56 g for field wires. The total cumulative wire tension is about 10.2 t. The wire tension values for each step are summarized in Table 4.2.

Table 4.2: Wire tension summary by step.

	Cell no./step	**Avg. length [mm]**	**Sense (g)**	**Field (g)**	**Total (kg)**
step1	9172	5668	86.92	133.56	4472.08
step2	7528	5122	70.98	109.07	2997.38
step3	5845	4526	55.43	85.16	1817.14
step4	3939	3928	41.75	64.14	922.46
Total	**26483**				**10209**

4.3.3 Finite Element Analysis

Finite Element Analysis (FEA) was conducted to evaluate the structural integrity of the chamber under the combined action of wire tension and self-weight. The results show a maximum von Mises stress of about 30 MPa in the endplate, with a corresponding maximum deformation of 2.7 mm. For the CF frame, the analysis gives a maximum von Mises stress of about 235 MPa and a maximum deformation of 1.1 mm. These results indicate that the overall structure remains mechanically stable under the applied loads [36].

4.4 Endplate optimization

As part of the mechanical optimization process, a detailed study was carried out on the endplate, focusing on two key aspects: the variation of its thickness and the geometrical configuration of the holes distributed across its surface.

The first part of the analysis consisted of a parametric finite element study aimed at identifying the minimum endplate thickness that would still ensure adequate structural rigidity under operational loads, particularly the wire tension and self-weight. This optimization was driven by the need to reduce the material budget, which is a critical factor in the overall detector design, especially in tracking systems where multiple scattering must be minimized.

In parallel, a second study was devoted to evaluating different configurations of the holes in the endplate. These holes are required for routing wires and services, and their number and arrangement directly impact the mechanical strength of the structure. Through systematic simulations, various radial and angular distributions were tested to determine the most efficient layout capable of accommodating the highest possible number of holes without inducing significant stress concentrations or compromising mechanical stability.

The results of both studies were used to guide the final design of the endplate, balancing competing requirements of low material budget, high structural integrity, and functional integration.

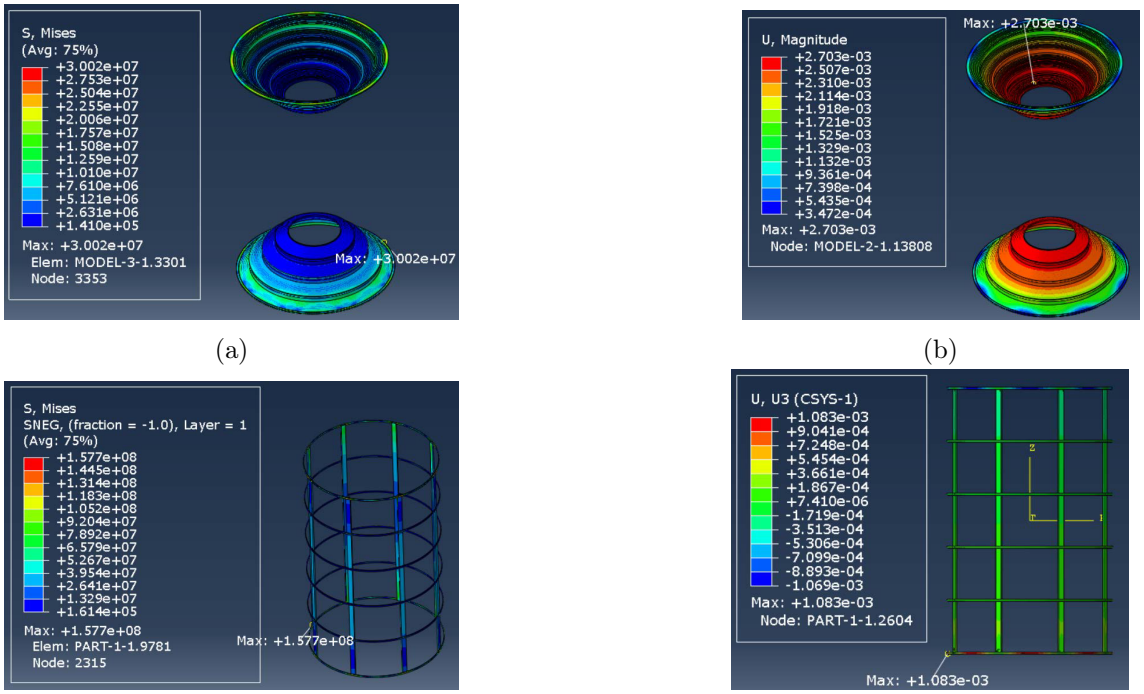

Figure 4.6: Finite Element Analysis results for the mechanical structure under wire tension and self-weight: (a) von Mises stress distribution in the endplates, (b) total displacement magnitude of the endplates, (c) von Mises stress distribution in the carbon-fiber support frame, and (d) axial displacement (U_3) of the carbon-fiber frame. The results show moderate stress levels and limited deformations, confirming the mechanical stability of the overall assembly.

4.4.1 Thickness optimization

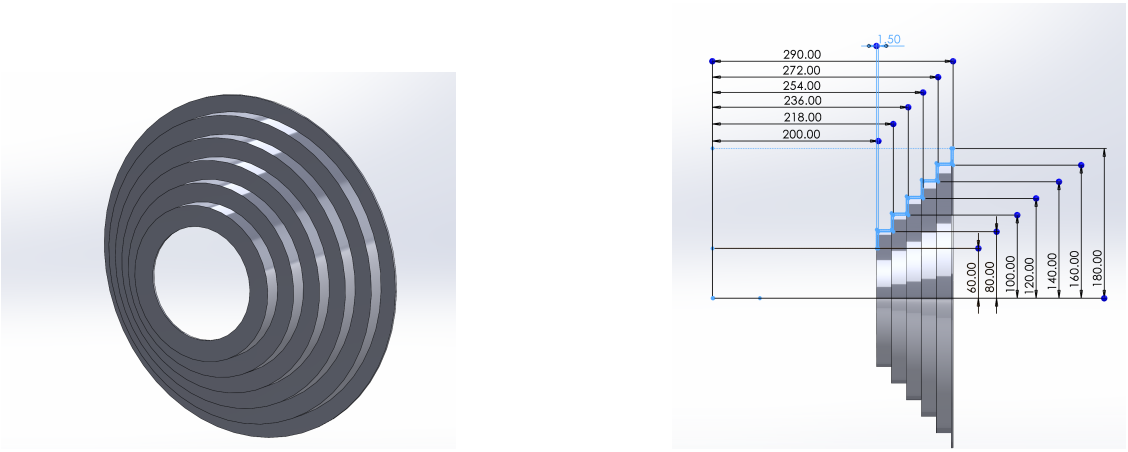

(a) (b)

Figure 4.7: Baseline stepped endcap geometry used for the CEPC thickness-optimization study. The views show the overall aluminum endcap design and the detailed stepped profile, which determines both the mechanical stiffness and the available wire-routing area.

Following the design and modeling of the endplate using SolidWorks (see Figure 4.7), a static structural analysis was performed in Ansys Workbench to assess its mechanical response under load. The simulation focused on evaluating two key parameters: the equivalent (von Mises) stress, which provides a measure of the yield criterion for ductile materials, and the equivalent elastic strain, used to quantify the deformation behavior of the structure. These metrics allowed for a comprehensive assessment of the mechanical performance of the endplate design under realistic loading conditions. In particular, the investigated thicknesses ranged from 15 mm to 25 mm, with increments of 2.5 mm. For each configuration, the static simulation results were analyzed to determine the maximum equivalent stress and elastic strain under the combined effect of wire tension and self-weight. The objective was to identify the minimum thickness that would keep stress levels well below the material yield strength, while limiting deformations within acceptable tolerances for precise wire alignment. This parametric approach enabled a quantitative comparison between different design options and guided the selection of the optimal endplate thickness in terms of both mechanical performance and material budget. A static structural analysis was carried out to assess the stiffness and stress state of the endplate under the equivalent load generated by the wire tension. The model was implemented in ANSYS Mechanical considering the nominal aluminum geometry and assuming linear elastic material behavior. The outer boundary was constrained according to the support configuration, while the wire load was represented through an equivalent distributed load. The results were evaluated in terms of equivalent elastic strain, and equivalent (von Mises) stress. Particular attention was devoted to the mesh definition in the critical regions and to the verification of result consistency through equilibrium checks and mesh-sensitivity analysis. The model was intended to provide a comparative and design-oriented evaluation of the structural response, rather than a fully detailed reproduction of all local assembly features. Figure 4.8 shows

the Equivalent Elastic Strain and Equivalent (von-Mises) Stress of the endcap with a thickness of 20mm.

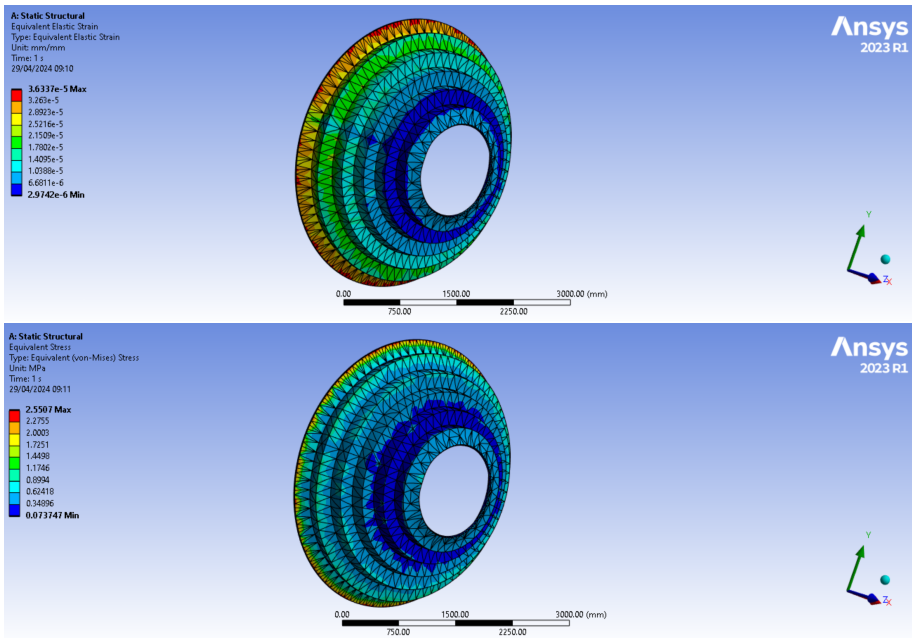

Figure 4.8: Static FEM results for the CEPC stepped aluminum endcap with a thickness of 20 mm. Top: equivalent elastic-strain distribution. Bottom: equivalent von Mises stress distribution. The results are used to assess the mechanical response of the reference geometry under the equivalent wire-tension load.

Thickness [mm]	**Max Eq. Elastic Strain ($\mu\varepsilon$)**	**Max Eq. Stress (MPa)**
15.0	208.0	14.75
17.5	72.8	5.17
20.0	36.3	2.55
22.5	30.9	2.19
25.0	29.1	2.07

Table 4.3: Maximum equivalent elastic strain and maximum equivalent (von Mises) stress as a function of the endplate thickness, as obtained from the ANSYS static structural analysis.

Table 4.3 and Figure 4.9 summarize the effect of the endplate thickness on the structural response of the component. Both the maximum equivalent elastic strain and the maximum equivalent (von Mises) stress decrease significantly when the thickness is increased from 15 to 20 mm, indicating a substantial improvement in stiffness and load-bearing capability within this interval. For thickness values above 20 mm, the reduction becomes much less pronounced, thus suggesting the onset of a diminishing-return regime. This result indicates that a thickness of about 20 mm represents a reasonable compromise between mechanical performance and material budget, since a further increase would provide only limited structural benefit while inevitably increasing the detector material budget.

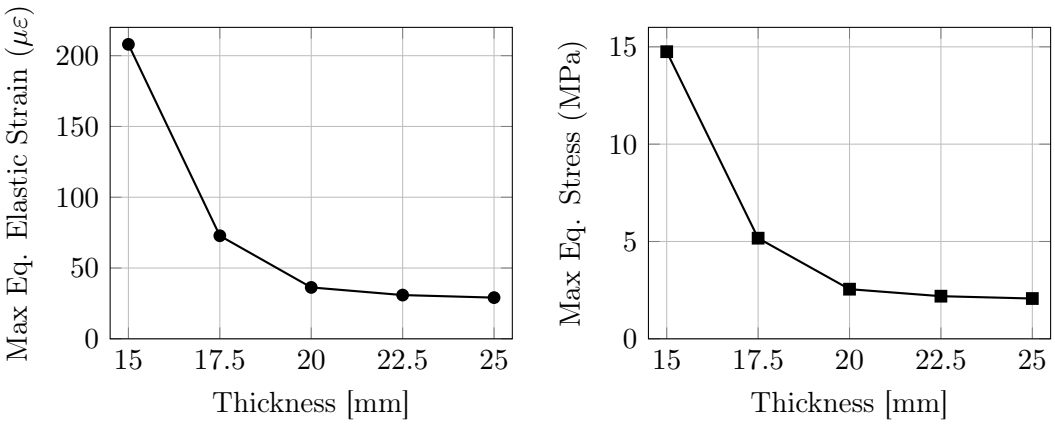

Figure 4.9: Dependence of maximum equivalent elastic strain and maximum von Mises stress on CEPC endcap thickness. Both quantities decrease strongly between 15 and 20 mm, while further thickness increases provide only marginal improvement, indicating a diminishing-return regime.

4.4.2 New version of the endcap

Since the endplate thickness also affects the number of wires that can be accommodated on each step of the current stepped geometry, and given that wires cannot be placed directly on the step regions—resulting in a loss of active area and reduced occupancy—an alternative design has been proposed. This new version of the endcap features a continuous, uniform surface with a concave disk shape, eliminating the stepped profile.

The revised geometry allows for a more efficient and uniform wire distribution, maximizing the number of instrumented cells and improving overall coverage. Moreover, the concave shape contributes to structural stiffness while maintaining compatibility with the mechanical constraints and alignment requirements of the detector. Further FEM studies are planned to validate the mechanical performance of this design under realistic loading conditions.

The proposed design is shown in Figure 4.10, and the FEM analysis was conducted assuming a uniform endplate thickness of 15 mm (see Figure 4.11). The simulation results indicate a significant improvement in mechanical performance compared to the stepped geometry with the same thickness. Specifically, both the equivalent elastic strain and the von Mises stress are considerably reduced, demonstrating that the concave disk design offers enhanced structural rigidity and better stress distribution, even at reduced thickness. Table 4.4 shows that Version II provides a substantial improvement in the mechanical response of the endplate, with the maximum equivalent elastic strain reduced from 208.0 $\mu\varepsilon$ to 12.7 $\mu\varepsilon$ and the maximum equivalent (von Mises) stress reduced from 14.75 MPa to 0.90 MPa. These results indicate a markedly higher stiffness and a significantly lower stress level in Version II with respect to Version I. These findings support the adoption of the new geometry as a promising solution for optimizing both the mechanical stability and functional efficiency of the endplate.

Although the concave geometry shows a clear improvement in the simplified FEM comparison, this result should be considered preliminary. The present model

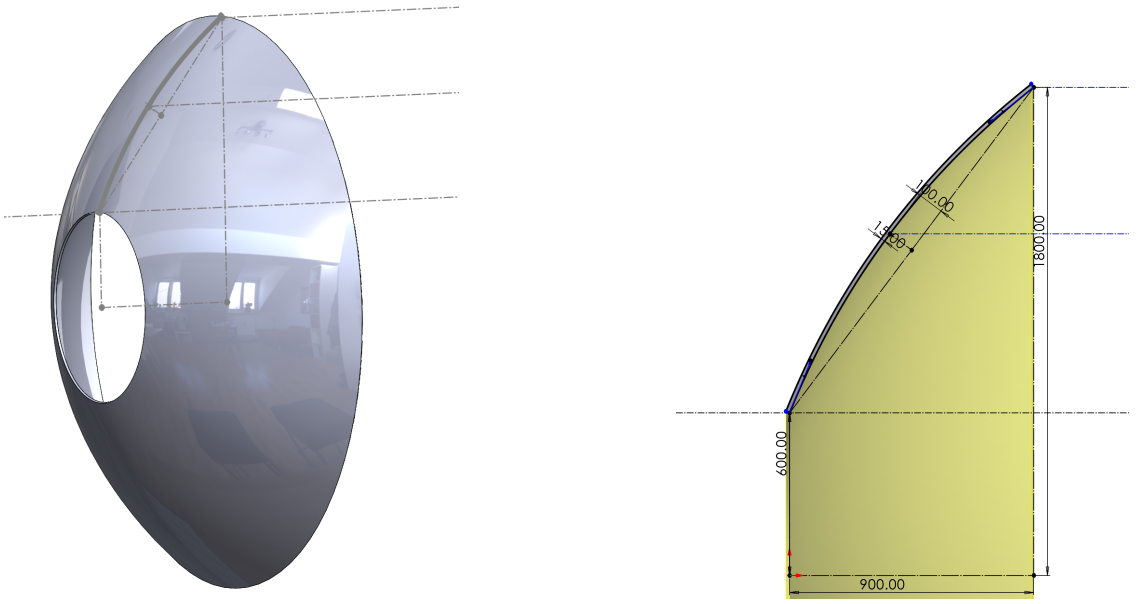

(a) (b)

Figure 4.10: Proposed concave CEPC endcap geometry. The design replaces the stepped profile with a continuous surface in order to improve active-area coverage and redistribute stiffness more efficiently while maintaining compatibility with the global endcap envelope.

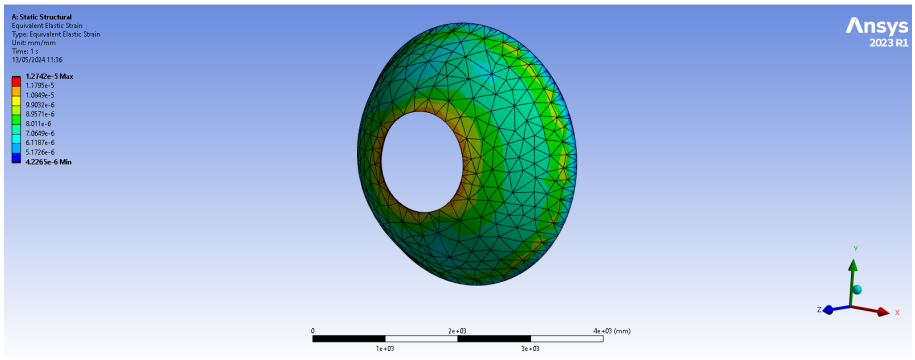

(a)

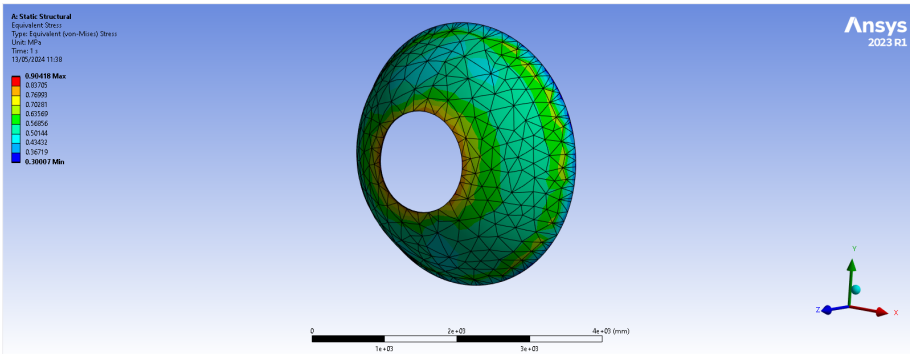

(b)

Figure 4.11: Static FEM results for the proposed concave CEPC endcap with a uniform thickness of 15 mm. The equivalent elastic strain and von Mises stress fields indicate improved global stiffness and lower stress levels with respect to the stepped geometry of the same thickness, within the assumptions of the simplified model.

	Version I	Version II
Maximum Equivalent Elastic Strain ($\mu\varepsilon$)	208.0	12.7
Maximum Equivalent (von Mises) Stress (MPa)	14.75	0.90

Table 4.4: Comparison of the maximum equivalent elastic strain and maximum equivalent (von Mises) stress for the two endplate versions.

does not yet include the complete hole pattern, local feed-through details, machining tolerances, assembly constraints, sealing interfaces, or possible stress concentrations around wire-routing holes. Moreover, the manufacturability of a large concave aluminum endcap and its compatibility with wire installation procedures must be assessed. Therefore, the concave solution is promising from the point of view of global stiffness, but it requires a more detailed local mechanical and integration study before being considered as a final design option.

4.4.3 Ongoing R&D on primary ionization counting in the CEPC framework

In parallel with the full-detector studies discussed in this chapter, it is worth mentioning that dedicated R&D activities on primary ionization counting have also been carried out within the broader CEPC drift-chamber program [37]. The main motivation is to explore the feasibility of using the dN/dx observable, rather than the conventional charge-based dE/dx, in order to improve particle-identification capabilities in a gaseous tracker. In the study presented by the CEPC collaboration, simulations indicate that for a track length of 1.2 m the dN/dx resolution can be below 3%, with a K/π separation power reaching about $3.2\,\sigma$ at $20\,\mathrm{GeV}/c$ [37].

To investigate this approach experimentally, a dedicated multilayer prototype was developed as a reduced-scale platform for signal studies, electronics validation, and reconstruction tests [37]. The prototype consists of 12 layers with 10 cells per layer, for a total of 120 cells, and adopts a cell size of 18×18 mm^2, consistent with the scale considered for the CEPC chamber. The active length of the detector is 60 cm. The anode wires are 20 μm gold-plated tungsten wires, while the field wires are 70 μm aluminum wires. In Figure 4.12 the prototype design is presented with the wire scheme of the first two layers. Although this prototype does not reproduce the full mechanical configuration of the CEPC drift chamber described in the previous sections, it provides a realistic test system for studying the detector response associated with cluster-counting techniques.

The detector construction and commissioning activities included wiring, tension checks, leakage-current measurements, and high-voltage training [37]. The reported operating parameters are 11 g tension for the 120 sense wires and 19 g for the 416 field wires, with a measured sag of about 25 μm and leakage currents below 1 nA [37]. Within this activity, my contribution concerned part of the detector commissioning and setup of the prototype system, contributing to the preparation of stable operating conditions for data taking and to the practical implementation of the experimental workflow. The entire working setup is showed in Figure 4.13.

A preliminary validation of the system was carried out through cosmic-ray mea-

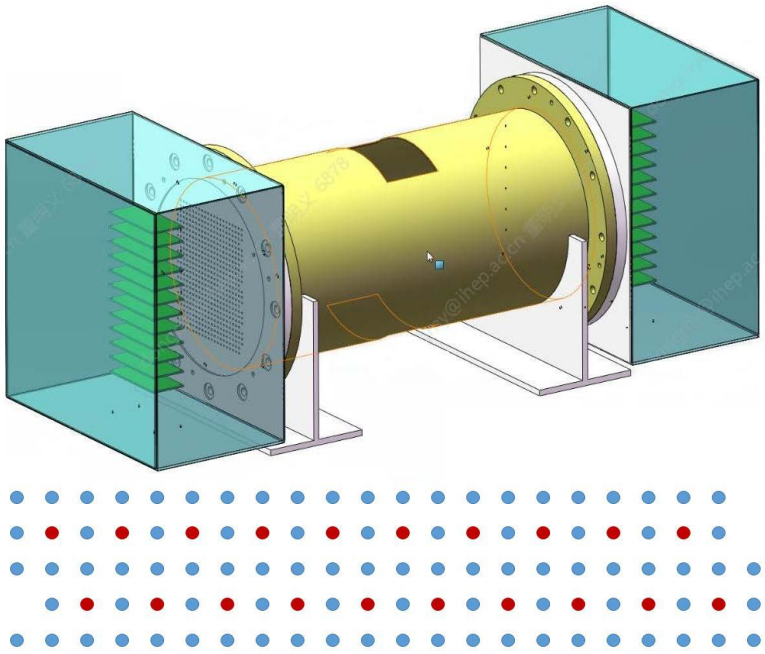

Figure 4.12: Multilayer drift-chamber prototype developed within the CEPC primary-ionization-counting R&D programme. Top: mechanical layout of the reduced-scale prototype. Bottom: wire scheme of the first two layers, showing the arrangement of sense wires and field wires used to study cluster-counting signal formation.

surements, using plastic scintillators for triggering together with the preamplifier chain, digitization electronics, trigger board, fanout board, and DAQ software [37]. The first analysis of these data indicates correct detector operation, with a measured baseline noise of $1.58\,\mathrm{mV_{rms}}$, a signal rise time of 2.65 ns, and a typical signal amplitude of 86.2 mV, see Figure 4.14 [37]. These results suggest that the acquired waveforms are suitable for detailed signal studies and for the development of dedicated peak-finding and cluster-reconstruction procedures. Overall, these prototype studies represent a useful complement to the full-chamber investigations discussed in this chapter. While the latter address the CEPC detector at the level of global geometry and mechanical feasibility, the prototype activity provides an experimental environment in which the readout chain, waveform quality, and signal-reconstruction strategy required for dN/dx-based particle identification can be directly investigated.

4.5 Next developments

A comprehensive mechanical optimization study was conducted on the drift chamber endplate, with the goal of minimizing the material budget while ensuring structural stability under realistic operating conditions. The investigation included a parametric analysis of the endplate thickness, together with a detailed evaluation of the hole distribution required for wire routing.

Finite Element Method simulations showed that a thickness of 20 mm represents an optimal compromise between stiffness and mass, keeping stresses and deformations within acceptable limits. In parallel, the optimization of the hole configuration demonstrated the feasibility of accommodating a large number of wire channels

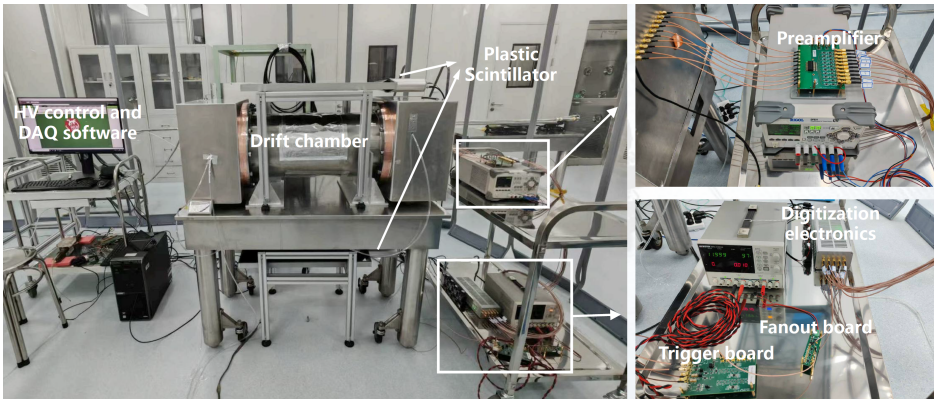

Figure 4.13: Experimental setup used for commissioning and preliminary cosmic-ray tests of the CEPC multilayer prototype. The setup includes the drift chamber, trigger scintillators, front-end electronics, digitization chain and data-acquisition system used to validate stable detector operation.

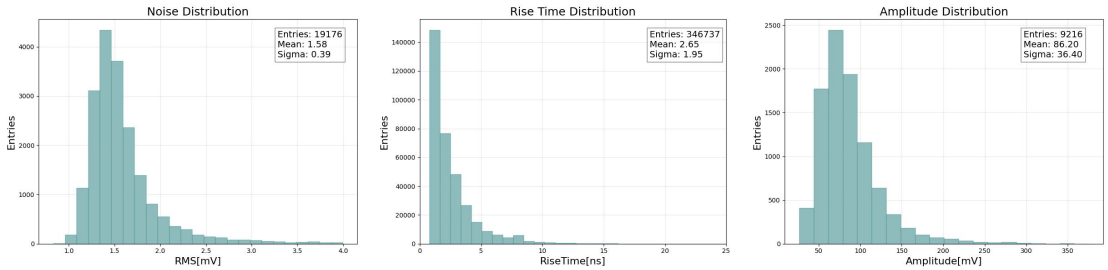

Figure 4.14: Preliminary waveform-quality measurements obtained with the CEPC multilayer prototype during commissioning. The distributions show baseline noise (left), signal rise time (center) and signal amplitude (right), confirming that the acquired waveforms are suitable for subsequent signal and cluster-reconstruction studies.

without compromising the mechanical integrity of the structure.

To further improve the active-area coverage and overcome the limitations associated with the stepped geometry, a new endcap design based on a uniform concave disk was proposed. The FEM results confirmed that this configuration, even with a reduced thickness of 15 mm, provides better performance than the stepped solution in terms of stress distribution and deformation control.

These results provide essential input for the final mechanical design of the CEPC drift chamber and highlight the importance of addressing structural and functional requirements in an integrated manner from the early stages of detector development. As a natural continuation of these full-chamber studies, dedicated prototype activities on primary ionization counting represent an important next step within the broader CEPC drift-chamber R&D program, offering a complementary experimental platform for the validation of readout strategies, waveform analysis, and dN/dx-based particle-identification techniques.

Chapter 5

Mechanical Characterization of Ultra-Thin Wires for Drift Chambers

5.1 Introduction

Ultra-thin wires are central to drift-chamber operation. Sense wires (anodes) provide gas amplification and deliver the signal to the front-end electronics, while field wires shape and stabilize the electric field within each cell. From a mechanical standpoint, wire material and diameter directly affect positioning accuracy, electrostatic stability, robustness during assembly, and long-term reliability.

For ultra-light tracking detectors developed for FCC-ee and CEPC, wire diameters in the (20–50) μm range are often considered to reduce the material budget and limit multiple scattering [19], [21]. The downside is that thinner filaments are more vulnerable to handling damage and to local stress concentrations introduced by clamping, crimping, and small alignment errors. In addition, environmental effects such as humidity-driven corrosion can become a practical failure driver during construction, especially for plated light-alloy wires and imperfectly protected terminations [38].

In a conventional drift-chamber layout, the sense wire is the instrumented anode: it is biased at positive high voltage and operates in avalanche mode in the immediate vicinity of the wire. Field wires (sometimes referred to as cathode or guard wires) mainly define the field configuration and are typically kept at ground potential or at a negative bias, depending on the cell design.

Because the anode experiences the highest electric field, its surface quality is critical: microscopic defects or contamination can trigger dark current, micro-discharges, and gain instabilities. For this reason, sense wires are usually made of very high tensile-strength materials to allow extremely small diameters with limited sag under tension. In this work we investigate 20 μm gold-plated tungsten (W–Au) and gold-plated molybdenum (Mo–Au) filaments, both provided by *Luma Metall*[1]. Gold plating reduces oxidation and surface contamination, improving electrostatic stability; this is particularly important because the operating high voltage is typically of the order of (1.5–2.0) kV, depending on gas mixture and geometry. Although tungsten is a high-Z material, its contribution to the overall material budget is mitigated

[1] https://lumawiretech.com/

by the very small filament diameter and by the low linear mass density of the wire set.

Field wires primarily provide field shaping and mechanical support for the cell, and can therefore be thicker than sense wires. Since the dominant design goal is to minimize multiple scattering, low-Z and low linear-mass materials are preferred. Here we study an innovative 33 μm carbon monofilament provided by *Specialty Materials*[2] (currently without coating). Studies on 40 μm aluminium wires are ongoing. For field wires, surface condition still matters to prevent discharges, but the requirements are generally less stringent than for the anode because the electric field at the wire surface is lower.

All wire types operate under constant tension throughout the detector lifetime, which is typically designed on a multi-decade timescale. A necessary first step toward mechanical stability is therefore a consistent mechanical characterization of candidate filaments, intending to define a common and safe operational window across materials. In this chapter, we propose an experimental procedure to characterize single-wire specimens and derive the ultimate tensile strength (UTS), the yield tensile strength (YTS, taken as a 0.1% proof stress when applicable), and the Young's modulus E.

5.2 Mechanical Model

The previous chapter quantified the mechanical constraints imposed by wire load on the endcap through FEM simulations. Here we move to an experimental characterization of candidate ultra-thin filaments for the IDEA/INTREPID drift-chamber prototype. Since all wires operate under constant tension over the detector lifetime, their mechanical response must be measured consistently to define a safe and reproducible operational tension window and handling margins across different materials and diameters.

5.2.1 Stress–strain definitions

In a uniaxial tensile test, the wire response is described in terms of engineering (nominal) stress σ and engineering strain ε:

$$\sigma = \frac{F}{A_0}, \qquad \varepsilon = \frac{\Delta L}{L_0}, \tag{5.1}$$

where F is the applied force, A_0 is the initial cross-sectional area, L_0 is the initial gauge length, and ΔL is the measured elongation. For a circular wire of initial diameter d_0,

$$A_0 = \frac{\pi d_0^2}{4}. \tag{5.2}$$

Within the linear elastic regime, stress and strain are related by Hooke's law,

$$\sigma = E\,\varepsilon, \tag{5.3}$$

with E the Young's modulus.

[2] https://www.specmaterials.com/

5.2.2 Mechanical properties extracted from the tensile curve

From the stress–strain curve $\sigma(\varepsilon)$ we extract three key material properties for wire operation:

- **Young's modulus (E).** E is obtained as the slope of the linear elastic region. In practice, E is computed via a linear regression over a selected strain interval where the response is linear. The initial "toe" region (often caused by seating and grip compliance) is excluded from the fit.
- **Yield tensile strength (YTS, 0.1% proof stress).** For thin filaments the onset of plasticity may be gradual or not clearly identifiable. For this reason, we define YTS as a proof stress using the 0.1% offset method:

$$\sigma_{\text{off}}(\varepsilon) = E(\varepsilon - 0.001). \tag{5.4}$$

  The intersection between the offset line in Eq. (5.4) and the experimental $\sigma(\varepsilon)$ curve defines YTS.
- **Ultimate tensile strength (UTS).** The UTS is the maximum engineering stress reached before fracture:

$$\text{UTS} = \max\big(\sigma(\varepsilon)\big) = \frac{F_{\max}}{A_0}. \tag{5.5}$$

These quantities provide a compact description of (i) elastic stiffness (E), (ii) the transition from elastic to irreversible deformation under a conservative criterion (YTS), and (iii) the maximum load-carrying capability (UTS). Together, they are used to define operational tensions, safety factors, and allowable handling margins for the wire set of the drift-chamber prototype.

5.2.3 Tension and sagitta constraint

In drift-chamber operation, tension is also the main knob to control sagitta. For a wire of free length L under an approximately uniform transverse load per unit length w, the mid-span deflection can be written, in the small-deflection approximation, as

$$\delta_{\max} \simeq \frac{wL^2}{8T}, \tag{5.6}$$

with T the applied tension [19]. This relation motivates the use of high-strength materials: a larger safety margin on rupture load allows higher working tensions and therefore smaller sagitta, provided that electrostatic stability and construction constraints are respected.

5.3 Experimental Setup

The tensile-test setup was developed by adapting the rationale of ASTM D3379 [39] (single-filament tensile testing) to ultra-thin drift-chamber wires and to a compact, alignment-controlled laboratory apparatus.

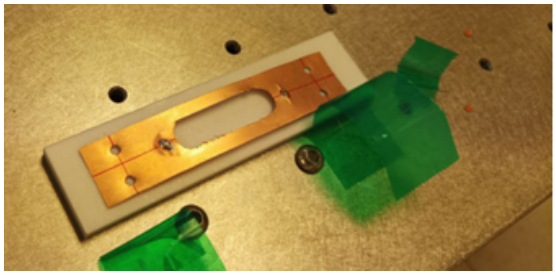

Figure 5.1: Copper-clad PET tab used for single-filament tensile testing. The central circular window defines the free gauge length of the wire specimen, while the copper-clad regions provide controlled attachment points and reduce direct handling of the ultra-thin filament.

5.3.1 Specimen preparation (tabbing)

Following the tabbing approach of ASTM D3379, each wire specimen was mounted on a copper-clad PET tab of size $100 \times 20\,\mathrm{mm}^2$, see Figure 5.1. A central circular window of diameter 50 mm was machined in the tab to define the free span ($L_0 \simeq 50\,\mathrm{mm}$). The filament was attached to the tab on both sides of the window, at a distance of 25 mm from each tab edge. Depending on the wire type and surface condition, the attachment was performed either by soldering (enabled by the copper cladding) or by adhesive bonding. The goal of tabbing is to minimize handling damage, improve gripping repeatability, and reduce stress concentrations at the grips.

5.3.2 Loading system and alignment

Force was measured using a digital dynamometer (PCE-FB series), used as a load cell to acquire the tensile load during the test. Displacement was applied by a motorized actuation system equipped with a three-axis piezo-positioning stage, software-controlled to improve alignment and reduce bending-induced artifacts. In particular, three Picomotor piezo linear actuators were used[3]. The tab was clamped at its extremities using custom-shaped aluminium grips designed to securely hold the PET tab while limiting parasitic compliance and rotation.

After mounting, the specimen was aligned with a laser level to ensure that the wire axis was collinear with the loading direction. Once alignment was achieved, the tab was cut across the central window, so that the applied displacement was transmitted only through the wire free span (gauge length), while the tab halves remained gripped.

A picture of the setup is shown in Fiure 5.2. All tests were performed in an ISO7 (class 10000) clean room to keep temperature and humidity stable, since low-load measurements are sensitive to environmental variations. Tests were performed on an optical table to reduce the impact of external vibrations.

[3] `https://www.newport.com/p/8303`

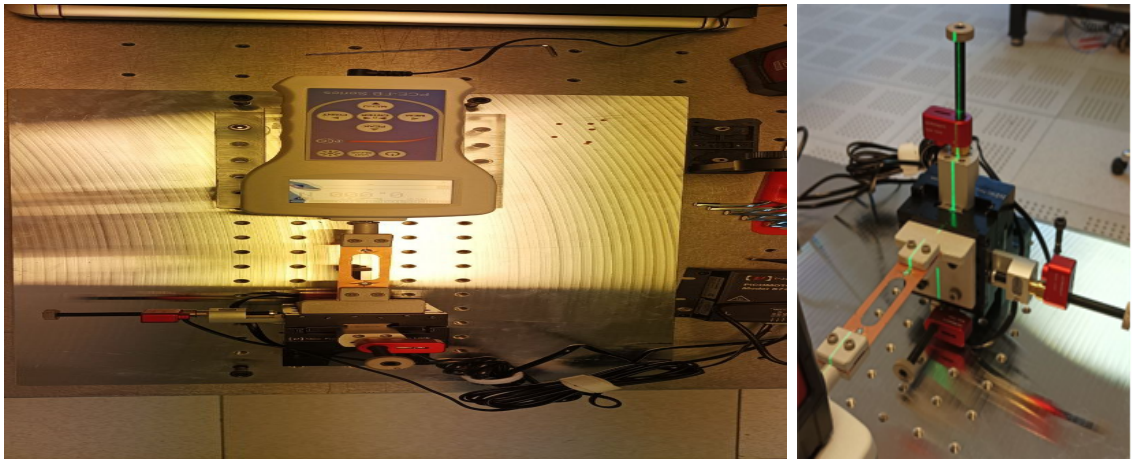

Figure 5.2: Experimental setup for tensile testing of ultra-thin drift-chamber wires. Left: complete setup including digital dynamometer, custom gripping system, mounted tab and three-axis piezoelectric actuation stage. Right: close-up of the actuator and tab region used to impose controlled displacement while maintaining alignment of the wire specimen.

5.3.3 Data processing and property extraction

Tensile load was applied at constant actuator velocity (*crosshead velocity*) until wire fracture. The raw output of each test consists of a time series of tensile load $F(t)$ acquired from the digital dynamometer. Data reduction is performed in four steps: (i) preprocessing and identification of the starting time, (ii) conversion from time to elongation and strain, (iii) construction of the engineering stress–strain curve, and (iv) extraction of E, YTS (0.1%), and UTS.

Before converting time to elongation, the load signal is baseline-corrected by subtracting the initial mean value measured with the specimen mounted but not yet tensioned.

The time t_0 corresponding to the start of the effective load is defined as the instant the wire becomes fully tensioned after the tab is cut at the center. Operationally, t_0 is identified when $F(t)$ first exceeds a small threshold F_{th} (chosen above the noise level) and remains above it for a minimum time interval. This procedure removes the initial toe associated with setup compliance.

The elongation is reconstructed from the imposed constant velocity v:

$$\Delta L(t) = v\,\big(t - t_0\big), \tag{5.7}$$

and the engineering stress and strain are computed using Eq. (5.1). (Unless stated otherwise, A_0 is computed from the nominal wire diameter.)

When fracture occurs, the last valid point is taken immediately before the load drop associated with failure.

Young's modulus E

E is obtained from the slope of the linear elastic region. Because the very first portion of the curve can be influenced by compliance and alignment residuals, the modulus is estimated by linear regression over a selected strain interval:

$$\sigma \approx E\,\varepsilon + b \qquad \text{for } \varepsilon \in [\varepsilon_1, \varepsilon_2], \tag{5.8}$$

excluding the toe region. The fitting interval is chosen to lie below the onset of non-linearity and to provide a stable fitted slope.

Yield tensile strength (YTS, 0.1% proof stress)

After E is determined, YTS is computed as the intersection between the experimental $\sigma(\varepsilon)$ curve and the 0.1% offset line $\sigma_{\text{off}}(\varepsilon) = E(\varepsilon - 0.001)$. For brittle-like filaments, fracture may occur before a clear intersection is reached; in such cases, YTS is effectively equal to UTS within uncertainties (as observed for the carbon monofilament).

5.4 Results

5.4.1 Rate-study and choice of the test velocity

A preliminary rate-study campaign on 20 μm W-wire was performed by repeating the tensile tests at different crosshead velocities, spanning from 10 μm/s to 50 μm/s. Results are reported in Table 5.1. The extracted values remain stable within uncertainties, as expected in this quasi-static regime.

Table 5.1: Tensile test results for 20 μm W-wire: ultimate tensile strength (UTS) and Young's modulus (E) as a function of crosshead velocity.

Velocity [μm/s]	**UTS [GPa]**	E **[GPa]**
50	2.844 ± 0.006	291.481 ± 5.312
40	2.827 ± 0.024	301.959 ± 13.658
30	2.821 ± 0.013	297.872 ± 9.309
20	2.799 ± 0.010	282.716 ± 6.140
10	2.785 ± 0.006	284.760 ± 11.154

Defining the nominal strain rate as $\dot{\varepsilon} = v/L_0$, this velocity range corresponds to $\dot{\varepsilon} \sim 2 \times 10^{-4}\,\text{s}^{-1}$ to $1.0 \times 10^{-3}\,\text{s}^{-1}$ for $L_0 \simeq 50\,\text{mm}$. Within this quasi-static regime, no systematic dependence of the extracted properties (E and UTS) was observed beyond the experimental uncertainties. Figure 5.3 illustrates the stability of UTS and E as a function of crosshead velocity.

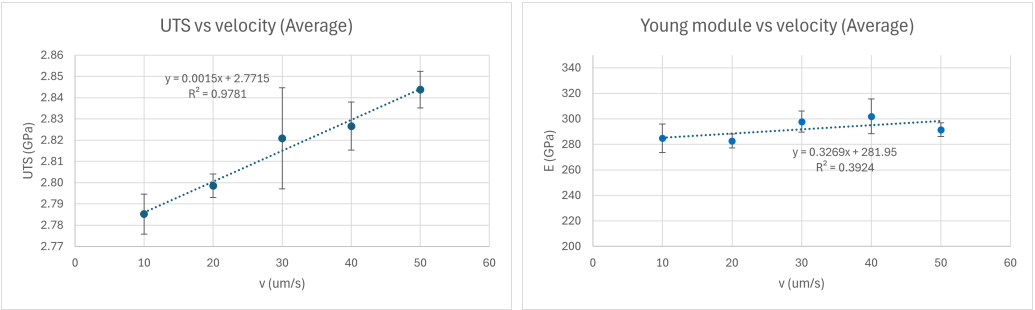

Figure 5.3: Rate-dependence study performed on 20 μm W–Au wires. The average ultimate tensile strength (left) and Young's modulus (right) are shown as a function of crosshead velocity, indicating stable quasi-static mechanical response in the tested velocity range.

For the remainder of the campaign, the crosshead velocity was fixed to 20 μm/s as a compromise between sufficiently slow loading (to remain in quasi-static conditions and limit dynamic artefacts) and adequate time resolution of the load signal (sampled at 40 Hz). A monotonic constant-velocity protocol was preferred over stepwise "static" loading because it provides a simpler and more reproducible definition of strain and strain rate, reduces the influence of seating and fixture relaxation, and avoids hold-time effects (tab/grip compliance, viscoelasticity of the tab/adhesive) that can bias the estimation of E and proof-stress yield criteria.

5.4.2 Stress–strain response and extracted properties

The stress–strain curves exhibit a clear linear-elastic regime followed by abrupt rupture, with only limited plastic deformation in the ultra-thin configuration. Tungsten provides the highest ultimate tensile strength, while molybdenum shows systematically lower values. Figure 5.4 reports representative stress–strain curves for W and Mo, highlighting the linear fit used to extract E, the 0.1% offset-line construction adopted to determine YTS, and the UTS value.

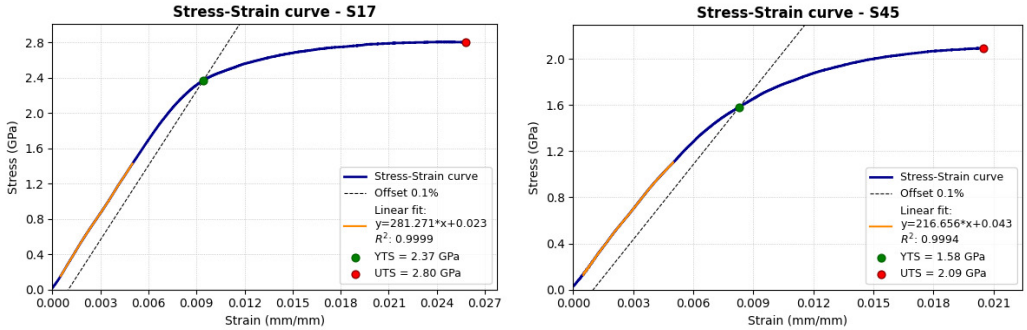

Figure 5.4: Representative engineering stress–strain curves for 20 μm W–Au wire (left) and Mo–Au wire (right). The plots show the linear elastic fit used to extract Young's modulus, the 0.1% offset construction used to determine the proof-stress yield value, and the ultimate tensile strength at rupture.

Carbon monofilament wires behave differently, exhibiting a brittle-like response. These wires fail abruptly with small strain-to-break. Figure 5.5 reports a representative stress–strain curve for the carbon monofilament, showing that in this case YTS coincides with UTS within uncertainties.

Five specimens were analyzed for each wire type. The results and associated uncertainties are reported in Table 5.2.

Table 5.2: Summary results of the tensile-test campaign for W–Au, Mo–Au and carbon monofilament wires.

Wire type	**UTS (GPa)**	**Young modulus E (GPa)**	**YTS (GPa)**
W–Au	2.80 ± 0.01	285.30 ± 7.49	2.34 ± 0.03
Mo–Au	2.11 ± 0.01	218.24 ± 7.91	1.62 ± 0.03
C	0.69 ± 0.12	38.24 ± 0.53	0.69 ± 0.12

Table 5.2 summarizes the key mechanical parameters extracted from the tensile-test campaign for the investigated ultra-thin filaments. Gold-plated tungsten pro-

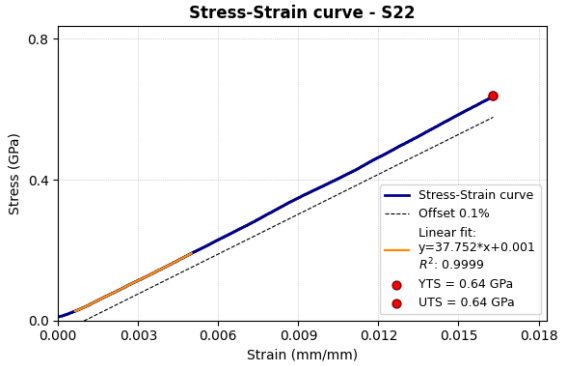

Figure 5.5: Representative engineering stress–strain curve for the tested carbon monofilament. The abrupt fracture and limited plastic deformation indicate a brittle-like response, for which the yield tensile strength is effectively coincident with the ultimate tensile strength within the experimental uncertainty.

vides the highest strength and stiffness, making it the most robust option for sense-wire operation at very small diameters and high tension. Gold-plated molybdenum exhibits systematically lower values, but remains compatible with mechanically demanding anode-wire applications, making it an interesting choice as anode wires. The carbon monofilament shows substantially lower stiffness and strength, consistent with its intended use as a low-mass field-wire candidate; the coincidence of YTS and UTS indicates a fracture-dominated response with limited margin against localized stress concentrations at terminations.

The relevance of these measurements for the design of the drift chamber is twofold. The measured YTS and UTS values define the mechanical safety margin for nominal operating stresses, while Young's modulus directly influences the prediction of wire elongation, tensile stability, and deflection under gravity. Therefore, the tensile test campaign provides experimental input parameters for the mechanical models discussed in Chapters 3 and 4.

5.4.3 Carbon monofilament as a low-mass field-wire candidate

Carbon monofilaments are of interest for ultra-light drift chambers as possible field-wire materials, since their low linear mass may contribute to a reduction of the overall tracker material budget. In the present study, the tested carbon monofilament exhibited an ultimate tensile strength of (0.69 ± 0.12) GPa and a Young's modulus of (38.24 ± 0.53) GPa, significantly lower than those measured for W–Au and Mo–Au wires. Its stress–strain response was brittle-like, with abrupt fracture at small strain and with YTS effectively coincident with UTS within uncertainties. This behavior is compatible with the use of carbon as a field-wire candidate rather than as an anode material, but it also indicates limited tolerance to local stress concentrations and therefore requires particular care in handling and termination design.

It should be emphasized that the carbon monofilament tested in this campaign was uncoated. In drift-chamber applications, carbon wires are expected to require a conductive surface treatment to ensure adequate electrical conductivity, solderabil-

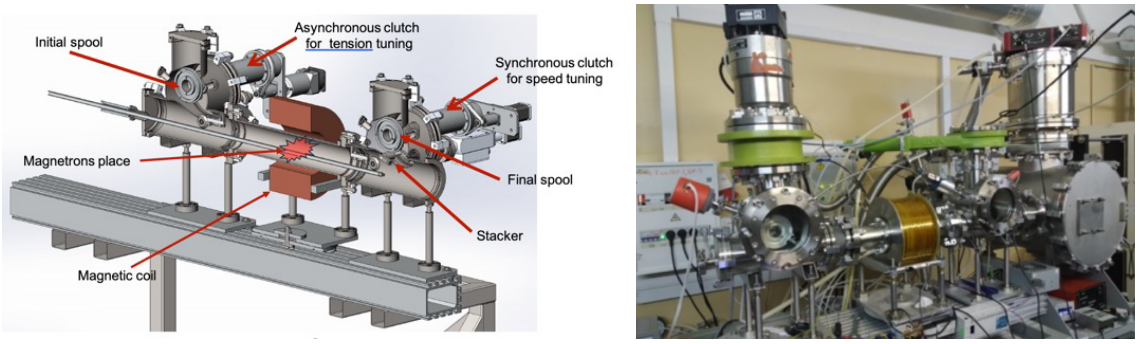

Figure 5.6: High-power impulse magnetron sputtering (HiPIMS) system considered for metallic coating of carbon monofilaments. Left: schematic representation of the physical-vapor-deposition process. Right: photograph of the sputtering apparatus. Such coatings are relevant for improving electrical conductivity, solderability and detector compatibility of carbon field-wire candidates.

ity, and electrostatic robustness. In this context, thin metallic coatings deposited by HiPIMS (High-power impulse magnetron sputtering), such as Ni/Cu bilayers, have been proposed as a possible technological solution [40]. Figure 5.6 depicts a machine for the metallic sputtering.

Preliminary studies reported in the detector R&D literature indicate that coated carbon wires can be integrated into drift-tube tests and may represent a viable option for low-mass gaseous trackers [41].

For the purposes of the present work, however, the values obtained on the uncoated monofilament should be regarded as a baseline mechanical characterization. Application-oriented parameters for detector design will require a dedicated follow-up study on coated carbon wires, with controlled coating type and thickness.

5.5 Limitations of the tensile-test campaign

Several limitations should be considered when interpreting the extracted mechanical properties. First, the stress values were computed using nominal wire diameters; therefore, diameter tolerances and plating-thickness variations directly affect the absolute values of UTS and YTS. Second, the strain was reconstructed from the imposed actuator displacement, so residual compliance of the tab, adhesive layer and gripping system may influence the absolute value of the Young's modulus. Third, the number of tested specimens was limited, and the results should therefore be interpreted as a preliminary qualification dataset rather than as a complete statistical characterization. Finally, the tests were monotonic and quasi-static; they do not yet address creep, stress relaxation, fatigue, humidity effects, corrosion, or long-term behaviour under sustained load, all of which are relevant for detector operation.

5.6 Conclusions

This chapter presented an ASTM D3379-inspired tensile-test methodology adapted to ultra-thin drift-chamber filaments and aimed at providing mechanically grounded

inputs for the IDEA/INTREPID prototype design. A dedicated tabbing and alignment-controlled setup was developed to test single wires under monotonic loading and to extract the engineering stress–strain response, from which Young's modulus E, the 0.1% proof-stress yield tensile strength (YTS), and the ultimate tensile strength (UTS) were derived.

A preliminary rate study on 20 μm W-wire in the 10–50 μm/s crosshead-velocity range (quasi-static strain rates for $L_0 \simeq 50$ mm) showed no systematic dependence of E and UTS beyond experimental uncertainties. The campaign was therefore standardized at 20 μm/s, improving repeatability and limiting fixture-relaxation artefacts that can bias proof-stress criteria.

The results demonstrate that W–Au provides the highest stiffness and strength, followed by Mo–Au, both supporting the use of ultra-thin metallic anodes with conservative mechanical margins. The carbon monofilament exhibits lower modulus and strength and a brittle-like failure mode, consistent with low-mass field-wire concepts but demanding careful termination and handling to avoid stress concentrations. Future work will extend this baseline characterization toward time-dependent effects under sustained load (relaxation/fatigue) and environment-driven degradation mechanisms relevant for long-term detector operation, while completing the ongoing aluminum-wire study.

Chapter 6

Non-destructive Evaluation of UV-Induced Damage in Fiber-Reinforced Benzoxazine Composites

The previous chapters addressed two key mechanical constraints of ultralight drift chambers: endplate deformation under wire loading and the mechanical reliability of ultra-thin wires. An additional requirement concerns the long-term stability of the lightweight composite structures used for the chamber body, support elements, and bonded interfaces. Even in the absence of visible macroscopic defects, small material variations can alter the stiffness, damping, and propagation of elastic waves, potentially impacting dimensional stability and detector calibration.

This issue is relevant not only for particle detectors, but also for aerospace structures, where polymer-based composites are exposed to extreme environmental conditions and must maintain their mechanical performance over long periods of operation. In both fields, the critical issue is early detection of damage before it develops into visible cracks or structural failure.

This chapter analyzes a Carbon/Benzoxazine laminate, specifically a 5HS HTA40/ BZ9110 composite manufactured by Resin Transfer Molding (RFT). The material consists of a thermosetting benzoxazine resin reinforced with high-tenacity carbon fibers arranged in a five-harness satin fabric. This material has already been mechanically characterized by the research group, including measurements of Young's modulus, Poisson's ratio and tensile strength [42]. It is therefore used in this study as a representative CFRP system for analyzing early degradation in lightweight structural components.

The aging procedure adopted in this work is based on controlled ultraviolet irradiation. UV exposure does not fully reproduce the radiation environment operating in particle detectors or spacecraft, which can include electrons, protons, neutrons, and gamma rays. Its penetration depth is limited, and its effects are primarily concentrated near the exposed surface. However, UV irradiation provides a controlled method for inducing photochemical degradation in the polymer phase and for testing the sensitivity of nondestructive techniques to early-stage material evolution.

For this reason, the results presented in this chapter should be interpreted as a diagnostic sensitivity study rather than a comprehensive radiation qualification campaign. The objective is to verify whether acoustic methods can detect measurable changes in material response after controlled aging. Two complementary techniques are considered: Pencil Lead Break (PLB) tests, which use a reproducible pulsed source, and Acousto-Ultrasonic (AU) tests, which actively probe the transmission of waves through the sample. Their combination allows us to correlate variations in amplitude, energy, duration and frequency content of the signal with possible damage-induced changes in wave propagation.

6.1 Acoustic-based methods for damage detection

Acoustic Emission (AE) monitoring is based on the detection of transient elastic waves generated by rapid local energy release, for example during microcrack formation, interfacial debonding or frictional processes inside a composite material [43], [44]. In this work, AE is used in a controlled configuration through the Pencil Lead Break (PLB) test, also known as the Hsu–Nielsen source. The fracture of a pencil lead on the specimen surface provides a repeatable impulsive excitation that can be used to compare wave propagation before and after UV exposure [45], [46].

The Acousto-Ultrasonic (AU) method provides the active counterpart of this approach. In this case, elastic waves are injected into the material by a piezoelectric transducer and measured by a receiving sensor [47], [48]. Changes in the transmitted waveform reflect modifications in attenuation, scattering and frequency redistribution.

The two techniques are therefore complementary. PLB tests are useful to study the response to a localized impulsive source, while AU tests provide a more controlled measurement of transmission between two known points. In both cases, the working hypothesis is that UV-induced material changes modify the propagation of elastic waves, producing measurable variations in time-domain and frequency-domain features.

6.2 Experimental campaign

The experimental campaign is structured around pre- and post-irradiation measurements performed on composite specimens exposed to controlled ultraviolet radiation. Since the acoustic source mechanism and acquisition geometry are nominally identical in all tests, any systematic variation observed in the recorded signals can be attributed to modifications in the wave transmission properties of the material, and therefore to radiation-induced microstructural changes [49]. The objective of this study is to develop a quantitative and multi-domain analysis framework capable of detecting subtle material degradation without inducing visible macroscopic defects. The central hypothesis is that UV-induced microstructural damage alters:

- the overall energy transmission of elastic waves,
- the statistical properties of AE hits,

- the spectral distribution of signal frequencies.

These effects can be detected through a combined analysis in the time domain and frequency domain, enabling a sensitive evaluation of changes in the elastic transparency of the material.

The two tests were conducted on carbon fiber reinforced polymer (CFRP) specimens with nominal dimensions of $100 \times 18 \times 3$ mm^3. An initial baseline characterization was first performed on all samples using both Pencil Lead Break (PLB) and Acousto-Ultrasonic (AU) techniques, in order to establish reference acoustic features representative of the undamaged material state.

For each specimen, the two main surfaces were conventionally labelled as side A and side B. Side B corresponds to the surface directly exposed to ultraviolet radiation during the aging process, while side A denotes the opposite, non-irradiated surface.

For each specimen, two distinct experimental configurations were investigated. In configuration A, both the acoustic source (pencil lead break or pulser transducer) and the receiving sensor were placed on the same surface of the specimen (side A). In configuration B, the source and the receiver were located on opposite surfaces, so that the elastic waves propagated through the full thickness of the composite. This dual-geometry approach allows the discrimination between surface-dominated propagation effects and bulk transmission effects, thus enhancing sensitivity to internal damage mechanisms such as interlaminar defects and fiber-matrix debonding.

The sensor used for both tests was a broadband piezoelectric AE Pico-sensor, a lightweight Miniature AE Sensor with Integral Coaxial Cable[1]. The sensor was connected to a 40 dB preamplifier and subsequently interfaced with the AEwin data acquisition software. The software AEwin is a Windows-based program for real-time simultaneous Acoustic Emission (AE) feature and waveform processing.

Subsequently, the specimens were subjected to accelerated ultraviolet aging through repeated exposure cycles of 40 hours using an AG19 UV accelerated weathering tester [50], [51]. The irradiation spectrum included both UVA and UVB components, with a total irradiance of 2 W/m^2 and a controlled black panel temperature of 70°C. All specimens were irradiated exclusively on side B, to introduce a controlled asymmetry in the damage distribution and to enable the investigation of directional effects in wave propagation between the irradiated and non-irradiated surfaces. These conditions were selected to promote photo-induced degradation mechanisms in the polymer matrix [52], while maintaining a stable and reproducible thermal environment.

After completing the UV exposure cycles, a second acoustic characterization was performed using the same PLB and AU experimental configurations as those adopted in the baseline tests. This pre–post comparative approach allows the investigation of variations in key signal features, such as amplitude, energy, attenuation and frequency content, which are directly associated with changes in elastic wave propagation induced by radiation-related microstructural modifications.

The complete numerical values of the AEwin features and of the waveform-derived quantities are reported in Appendix A. In the following sections, the discussion focuses on representative spectra, damage indices and the main physical

[1] https://www.physicalacoustics.com/content/literature/sensors/Model_PICO.pdf

trends, which provide a more compact interpretation of the material evolution after UV exposure.

6.3 Pencil Lead Break test

The Pencil Lead Break (PLB) test, also known as the Hsu–Nielsen source, is a standardized artificial acoustic emission technique widely employed for the calibration and validation of AE monitoring systems. The test consists in pressing a brittle pencil lead, typically with a diameter of 0.5 mm and hardness HB, against the surface of the specimen at a controlled angle,, typically 30°–45°, until fracture. The sudden release of elastic energy generates a transient wave that mimics a localized AE source and allows comparison between different material states.

The sensor was placed on the surface A at 2.5cm from the small border, while the pencil was broken at the same distance in the opposite side on the surface A (configuration A) and then on the surface B (configuration B). For each AE hit, the acquisition system provides those features used for statistical validation:

- Counts (N),
- Energy (E),
- Duration (T),
- Amplitude (A),
- Frequency Centroid (f_c),
- Peak Frequency (f_p).

Plus full AE waveforms are stored as time series and are processed for spectral analysis:

$$x(t_i), \quad i = 1, \ldots, N, \tag{6.1}$$

By repeating the PLB at fixed locations, it is possible to assess the repeatability of the acquisition chain and to investigate variations in wave propagation properties induced by changes in the material state, such as damage accumulation or environmental effects. For each configuration and for each specimen, three independent acoustic events (hits) were recorded in order to improve statistical robustness and to mitigate the influence of local variability in source coupling and sensor positioning.

6.3.1 PLB AEwin features

The first level of analysis aims at validating the stability and reproducibility of the AE acquisition system. For each specimen and sensor side, the mean and standard deviation of classical AE parameters provided by the acquisition system are computed:

$$\mu_X = \frac{1}{M} \sum_{k=1}^{M} X_k, \tag{6.2}$$

$$\sigma_X = \sqrt{\frac{1}{M-1}\sum_{k=1}^{M}(X_k - \mu_X)^2}, \tag{6.3}$$

where $X \in \{N, E, T, A, f_c, f_p\}$ and M is the number of AE hits.

This analysis ensures that observed differences in subsequent stages are not caused by instrumental instability.

Table A.1 in the appendix reports the main Acoustic Emission (AE) features provided by the AEwin software for the different samples, configurations, and UV irradiation states. The selected parameters include both time-domain quantities (Counts, Energy, Duration, Amplitude) and frequency-domain descriptors (Frequency Centroid and Frequency Peak), providing a synthetic representation of the signal evolution as a function of material degradation. The labels *pre*, *post40* and *post80* refer to the sample before UV exposure, after 40 hours and after 80 hours, respectively.

The Counts exhibit a non-monotonic behaviour between the pre- and post-irradiation states. In several cases (e.g. sample 43, configuration B), a significant increase is observed in the post40 condition, indicating an enhanced AE activity associated with the activation of new damage sources. This is often followed by a decrease in the post80 state, consistent with a more advanced damage regime in which a large fraction of the stored elastic energy has already been released.

The mean Energy generally decreases after irradiation, suggesting a transition from a limited number of high-energy events to a larger population of low-energy emissions. This behaviour is typically associated with diffuse damage mechanisms, such as microcracking, interlaminar friction, and progressive debonding within the composite structure.

A particularly relevant trend is observed in the Duration parameter, which shows a marked increase in the post40 condition for several samples (e.g. 41B, 42A, and 43B), reaching values up to three times larger than in the pre-irradiation state. Longer signal durations indicate more complex waveforms, compatible with damage propagation processes and interactions among multiple defects, rather than isolated impulsive events.

The Amplitude exhibits an overall decreasing trend with increasing damage level, indicating a reduced capability of the material to generate high-intensity AE signals. This effect can be attributed to increased internal damping and loss of structural continuity due to the accumulation of micro-defects.

From a spectral perspective, the Frequency Centroid remains relatively stable across the different irradiation states, suggesting that the dominant emission mechanisms do not undergo substantial changes. Conversely, the Frequency Peak shows more pronounced variations, with a tendency to shift towards lower frequencies after irradiation. This behaviour is consistent with increased attenuation of high-frequency components caused by the presence of internal interfaces and distributed micro-damage.

Overall, the combined analysis of time- and frequency-domain features highlights a clear transition from an initial regime dominated by impulsive, high-energy events to a progressive damage regime characterized by longer, lower-amplitude signals with reduced spectral content. These trends are fully consistent with the expected

physical evolution of UV-induced degradation in composite materials.

6.3.2 PLB Waveform-processing strategy

Although spectral features such as the frequency centroid, peak frequency, and signal energy were already available in the previous analysis step as part of the standard AE hit parameters, these quantities are inherently dependent on the internal signal processing chain implemented by the acquisition system, including threshold-based triggering, hit segmentation, and proprietary filtering. As a consequence, the extracted features may not represent the full physical content of the propagating waveform, but rather a truncated and system-dependent version of it. In order to obtain a more physically grounded and reproducible characterization of wave propagation, in this step the same spectral indicators are recalculated directly from the raw acquired waveforms. This approach removes the dependence on acquisition thresholds and internal processing algorithms, allowing the spectral analysis to be performed on the complete impulse response of the system. Consequently, the derived features can be interpreted as intrinsic properties of the propagation medium, enabling a more robust assessment of material degradation based on fundamental signal processing principles rather than on vendor-specific AE descriptors.

For each experimental configuration (specimen, side, and irradiation state), three independent waveforms are processed and the extracted spectral quantities are averaged in order to reduce statistical fluctuations. For each recorded acoustic emission signal $s(t)$, two complementary signal processing pipelines are applied to decouple purely spectral shape information from physically meaningful energy content. In the *shape pipeline*, the time-domain waveform is normalized by its maximum absolute amplitude,

$$\tilde{s}(t) = \frac{s(t)}{\max |s(t)|}, \tag{6.4}$$

so that the subsequent analysis becomes invariant to absolute signal magnitude and only retains information on the relative distribution of frequency components. This pipeline is therefore used to characterize modifications in the spectral structure induced by changes in wave propagation mechanisms, independently of attenuation effects.

In parallel, a *physics pipeline* is defined by preserving the original signal amplitude, thus maintaining the physical scaling of the elastic wave. This second pipeline is used to extract energy-related quantities directly linked to the mechanical transmissivity of the material.

In both cases, the spectral content is analysed by computing the discrete Fourier transform through a fast Fourier transform (FFT) algorithm,

$$S(f_k) = \sum_{n=0}^{N-1} s_n \, e^{-i2\pi kn/N}, \tag{6.5}$$

and then computing the normalized amplitude spectrum

$$|S(f_k)|/N \tag{6.6}$$

, where N is the number of samples and $f_k = kf_s/N$ represents the discrete frequency bins associated with the sampling frequency f_s. The normalization removes the influence of absolute gain and sensor coupling, allowing a direct comparison between different measurements. For the shape pipeline, the spectral features are computed from the power spectrum, defined as $P(f_k) = |X(f_k)|^2$, where $X(f_k)$ is the discrete Fourier transform of the signal.

The spectral centroid represents the energy-weighted mean frequency and provides a compact descriptor of the dominant frequency content of the signal. It is computed as:

$$f_c = \frac{\sum_k f_k P(f_k)}{\sum_k P(f_k)}. \tag{6.7}$$

The bandwidth is defined as the 90% energy bandwidth and quantifies the frequency interval containing the central portion of the signal energy, making it robust with respect to noise and low-amplitude spectral components. The normalized cumulative distribution is:

$$C(f_k) = \frac{\sum_{i=1}^{k} P(f_i)}{\sum_{i=1}^{N/2} P(f_i)}. \tag{6.8}$$

The lower and upper cutoff frequencies are:

$$f_{5\%} = \min\{f_k \mid C(f_k) \geq 0.05\}, \qquad f_{95\%} = \min\{f_k \mid C(f_k) \geq 0.95\}, \tag{6.9}$$

and the bandwidth is:

$$\mathrm{BW}_{90} = f_{95\%} - f_{5\%} \tag{6.10}$$

Finally, the high-to-low frequency ratio R compares the energy content above and below a fixed threshold frequency (set to 300 kHz) and is used as a dimensionless indicator of spectral shape variations associated with material or structural changes. It is defined as:

$$R = \frac{\sum_{f_k > f_{\mathrm{HF}}} P(f_k)}{\sum_{f_k \leq f_{\mathrm{HF}}} P(f_k)} \tag{6.11}$$

The physics pipeline computes energy-related metrics on the raw waveform- Three main features are extracted from each waveform: the total signal energy (E), the root mean square (RMS), and the high-to-low frequency energy ratio (R_E). These features quantify the overall signal intensity, its average amplitude, and the spectral distribution of energy, respectively.

The total energy of a waveform in the time domain is computed as the sum of the squares of its samples:

$$E = \sum_{n=0}^{N-1} x[n]^2 \tag{6.12}$$

where $x[n]$ is the signal amplitude at sample n and N is the total number of samples. This feature is proportional to the overall amplitude of the signal and provides a measure of the acoustic activity.

The RMS of a waveform provides the average magnitude of the signal over its duration:

$$\mathrm{RMS} = \sqrt{\frac{1}{N} \sum_{n=0}^{N-1} x[n]^2} \tag{6.13}$$

Unlike the total energy, RMS normalizes by the number of samples, giving a measure that is independent of the signal length. It is particularly useful to compare signals of different durations or amplitudes.

The spectral content of the signal is analyzed by computing the power spectrum $P(f_k)$ mentioned for the shape pipeline. The energy in the low-frequency (LF) and high-frequency (HF) bands is then calculated in the same way of shape pipeline(6.11) but denoted as R_E. Unlike R, R_E depends on the absolute signal energy and represents the actual energy content distributed between high and low frequencies.

For each feature Q, a damage index was defined as the ratio between post- and pre-irradiation ensemble averages:

$$DI_Q = \frac{\langle Q_{\text{post}} \rangle}{\langle Q_{\text{pre}} \rangle}. \tag{6.14}$$

providing a direct measure of the relative variation of wave transmission between damaged and pristine conditions. Since individual pencil break hits are statistically independent realizations of the excitation process, the damage index was defined as the ratio between post- and pre-irradiation ensemble averages, rather than as the average of single-hit ratios. The associated uncertainty was obtained via standard error propagation. This dual-pipeline approach enables the separation of geometrical modifications of the spectral content from genuine physical attenuation phenomena, ensuring that structural degradation is interpreted on both morphological and energetic levels.

6.3.3 PLB test results

To evaluate the effect of irradiation on the AE signals, the amplitude spectra of the waveform for each specimen and side were computed and compared across different states (pre, post40, post80). Using the amplitude spectrum (6.6) preserves the relative contribution of each frequency and avoids the introduction of additional parameters such as segment length or overlap, which would affect feature comparability across different states.

The Figure 6.1 presents the overlaid amplitude spectra for each specimen on side B, with the three irradiation states shown together.

Then all the features described in the previous section were calculated for both pipelines. Table A.2 and Table A.3 group all the results for the features and Table 6.1 and Table 6.2 present the damage indices for each feature. To provide a clearer representation of the variations in the damage indices, a set of heat maps was constructed for each extracted feature. Figure 6.2 shows a map of the damage indices values for both pipeline analyses.

The comparison between the two AE analysis pipelines highlights complementary insights in terms of possible material degradation induced by UV irradiation.

Shape pipeline

Shape-based damage indices (DI_{fc}, DI_{BW}, DI_R) primarily reflect modifications in the spectral content of the signals, capturing shifts in the frequency centroid, changes

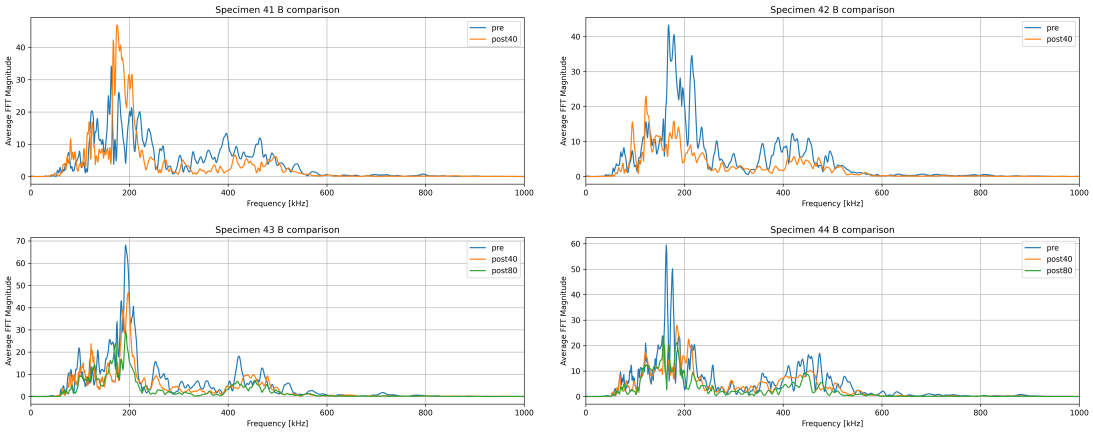

Figure 6.1: PLB test: amplitude spectra of the acoustic waveforms recorded for specimens 41–44 in configuration B, where the acoustic source and the receiving sensor are located on opposite surfaces of the specimen. For each specimen, the pre-irradiation spectrum is compared with the spectra measured after 40 h and, where available, 80 h of UV exposure. The comparison highlights irradiation-induced changes in the transmitted frequency content, especially in the high-frequency region.

Table 6.1: PLB test: waveform analysis results - Shape Damage Indices

Config	$DI_{fc,40}$	$DI_{fc,80}$	$DI_{BW,40}$	$DI_{BW,80}$	$DI_{r,40}$	$DI_{r,80}$
41A	0.92 ± 0.10	–	1.02 ± 0.09	–	0.66 ± 0.34	–
41B	0.80 ± 0.03	–	0.55 ± 0.23	–	0.15 ± 0.06	–
42A	1.05 ± 0.05	–	1.20 ± 0.05	–	1.79 ± 0.53	–
42B	0.89 ± 0.07	–	1.19 ± 0.10	–	0.99 ± 0.49	–
43A	1.05 ± 0.10	0.91 ± 0.12	0.99 ± 0.01	0.89 ± 0.09	1.26 ± 0.63	0.65 ± 0.47
43B	1.00 ± 0.03	0.96 ± 0.03	1.09 ± 0.04	1.04 ± 0.06	1.10 ± 0.24	1.12 ± 0.29
44A	1.24 ± 0.09	1.00 ± 0.09	1.16 ± 0.13	1.05 ± 0.18	3.31 ± 1.36	1.21 ± 0.72
44B	1.03 ± 0.13	0.90 ± 0.05	0.95 ± 0.02	0.94 ± 0.01	1.21 ± 0.73	0.65 ± 0.19

Table 6.2: PLB test: waveform analysis results - Physics Damage Indices

Config	$DI_{E,40}$	$DI_{E,80}$	$DI_{RMS,40}$	$DI_{RMS,80}$	$DI_{RE,40}$	$DI_{RE,80}$
41A	1.08 ± 0.28	–	1.05 ± 0.13	–	0.66 ± 0.34	–
41B	1.30 ± 0.66	–	1.18 ± 0.29	–	0.15 ± 0.06	–
42A	0.32 ± 0.07	–	0.56 ± 0.07	–	1.79 ± 0.53	–
42B	0.26 ± 0.08	–	0.51 ± 0.08	–	0.99 ± 0.49	–
43A	0.94 ± 0.34	0.83 ± 0.35	0.98 ± 0.17	0.91 ± 0.19	1.26 ± 0.63	0.65 ± 0.47
43B	0.45 ± 0.20	0.21 ± 0.11	0.69 ± 0.17	0.47 ± 0.13	1.10 ± 0.24	1.12 ± 0.29
44A	0.44 ± 0.11	0.24 ± 0.06	0.66 ± 0.08	0.50 ± 0.06	3.31 ± 1.36	1.21 ± 0.72
44B	0.51 ± 0.14	0.29 ± 0.06	0.71 ± 0.10	0.54 ± 0.05	1.21 ± 0.73	0.65 ± 0.19

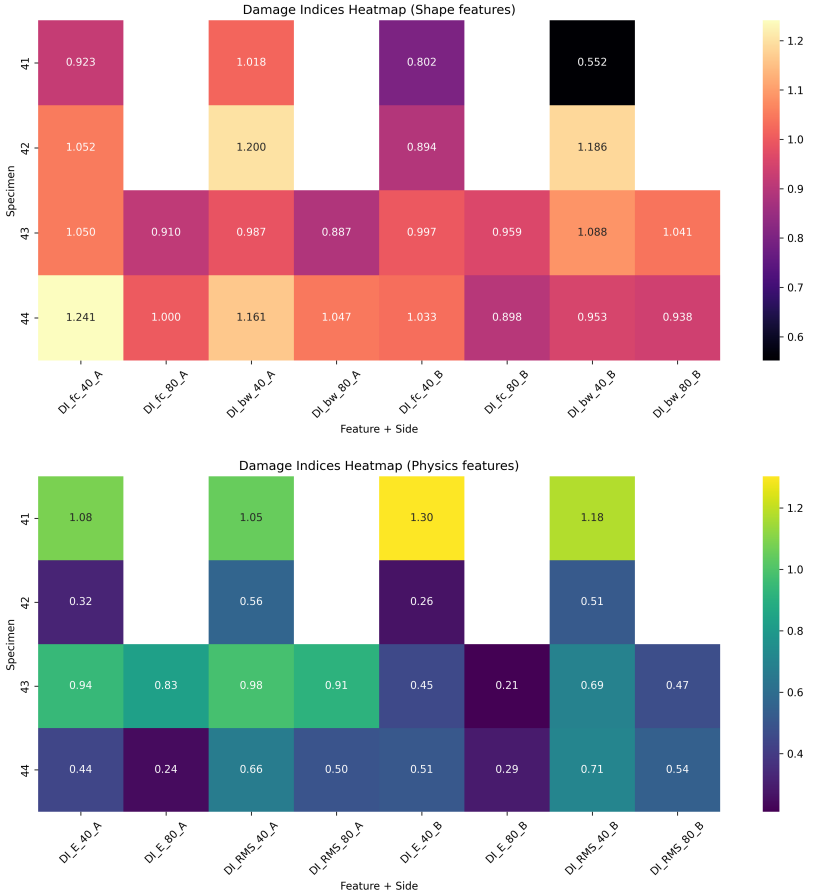

Figure 6.2: PLB test: heat maps of the damage indices extracted from the waveform analysis. The upper panel summarizes the shape pipeline, based on normalized spectral descriptors (f_c, BW and R), while the lower panel summarizes the physics pipeline, based on amplitude-preserving quantities (E, RMS and R_E). Values close to unity indicate little variation with respect to the pre-irradiation state, whereas values significantly above or below unity indicate UV-induced changes in spectral distribution or transmitted acoustic energy.

in bandwidth, and the redistribution of energy across frequencies. Since they are normalized with respect to the pre-state, all variations can be interpreted as pure changes in the spectral shape, independent of the absolute amplitude of the signal.

The frequency centroid f_c represents the center of mass of the amplitude spectrum. Therefore, a shift of f_c towards lower values indicates a relative loss of high-frequency components, which is consistent with a low-pass filtering behaviour of the propagation medium. In our case, from Table 6.1 and more clearly from the Figure 6.2, we can observe that, for samples 41 and 42, the values of f_c in configuration A remain substantially stable, whereas in configuration B a clear decrease is observed, indicating a loss of high-frequency components after irradiation. For samples 43 and 44, no significant differences emerge between configurations A and B; however, the second irradiation cycle appears to systematically promote a further reduction of the high-frequency content, suggesting a cumulative damage effect on the spectral shape.

The bandwidth BW quantifies the spectral dispersion and reflects the effective range of transmitted frequencies. An increase in bandwidth may be associated with enhanced scattering mechanisms or mode conversions induced by microstructural damage, whereas a decrease would suggest selective attenuation of specific frequency bands. In our case study, samples 41 and 42 show a general increase after the first irradiation step, indicating a broader spectral content despite the concurrent reduction of the high-frequency centroid. This suggests that the spectral energy is redistributed toward lower and intermediate frequencies rather than being uniformly attenuated. In contrast, samples 43 and 44 exhibit a more stable behavior, with limited variations in bandwidth between configurations A and B, although a slight narrowing is observed after the second irradiation cycle.

The high-to-low frequency ratio R provides a more direct quantification of the relative contribution of high-frequency components with respect to low-frequency ones, thereby complementing the information provided by the frequency centroid by isolating spectral redistribution effects. So the samples 41 and 42 display a marked decrease in configuration B, consistently with the loss of high-frequency components, while samples 43 and 44 show smaller and less systematic variations, pointing to a more moderate impact of irradiation on the overall spectral balance. Overall, the ratio emerges as a more sensitive indicator of high-frequency degradation, whereas the bandwidth reflects a more global reshaping of the spectral distribution.

Physics pipeline

Focusing on the physics pipeline, the extracted features highlight clear specimen-dependent behaviors. For specimen 41, both energy and RMS increase after irradiation in configuration B, with damage indices larger than unity ($DI_{E,40} \approx 1.30$, $DI_{RMS,40} \approx 1.18$), indicating an enhancement of acoustic activity. In configuration A, variations are more moderate, suggesting a weaker irradiation effect.

Specimen 42 shows an opposite trend: both energy and RMS decrease significantly after irradiation for both configurations, with damage indices well below one ($DI_{E,40} \approx 0.3$, $DI_{RMS,40} \approx 0.5$). This behavior is consistent with a global attenuation of signal amplitude, possibly due to increased damping or loss of efficient stress wave transmission.

Specimen 43 exhibits intermediate behavior. In configuration A, energy and RMS remain close to the reference state ($DI \approx 1$), while in configuration B both features decrease, especially after the second irradiation cycle. This suggests that damage effects are configuration-dependent and not uniformly distributed across the specimen.

Finally, specimen 44 shows a systematic reduction of both energy and RMS after irradiation for both configurations, with damage indices between 0.4 and 0.7. This indicates a strong attenuation of the acoustic emission response, compatible with a progressive degradation of the material's ability to generate or transmit elastic waves.

Overall, the physics pipeline reveals that irradiation does not induce a universal trend but rather a specimen-specific response, ranging from signal amplification (specimen 41) to strong attenuation (specimens 42 and 44). Energy and RMS thus act as sensitive indicators of global amplitude changes, but their interpretation must account for local material conditions and configuration effects.

6.3.4 Conclusion of PLB test

The comparison between the shape and physics pipelines highlights a significant specimen-dependent behaviour. While a general trend toward a reduction of high-frequency components is observed in several configurations, the magnitude and direction of these changes vary across samples. In particular, specimens 41 and 42 show more pronounced and systematic spectral shifts, especially in configuration B, suggesting a clearer sensitivity to irradiation. In contrast, specimens 43 and 44 exhibit a more stable behaviour, with smaller variations between configurations and a less marked response to the irradiation cycles.

From the physics pipeline, the differences are even more evident: some samples display a strong attenuation of energy and RMS after irradiation, whereas others remain close to the pre-irradiation level or show non-monotonic trends. This confirms that the acoustic response is strongly influenced by local material conditions and the initial state of the specimens.

The combination of both approaches supports the interpretation that irradiation affects not only the magnitude of the acoustic emission but also the underlying physical processes responsible for signal propagation.

Overall, the comparison between the AEWin features and the two proposed pipelines highlights a strong physical consistency across all samples, with each specimen exhibiting a distinct damage signature under UV irradiation. Sample 41 mainly shows a spectral modification, where the frequency content shifts towards lower frequencies without a significant loss in emitted energy, suggesting a damage mechanism dominated by viscoelastic aging of the matrix or interface degradation. Sample 42, instead, is characterized by a clear reduction in both energy and RMS, indicating a more severe structural damage where the material progressively loses its ability to release elastic energy through acoustic emissions. Sample 43 represents the most coherent and progressive case, with all pipelines consistently showing a cumulative degradation as a function of irradiation time, pointing to a classical damage evolution from chemical modifications of the matrix to interfacial weakening. Finally,

sample 44 exhibits the most complex and unstable behavior, with strong fluctuations in both spectral shape and energetic features, suggesting the coexistence of multiple damage mechanisms, including matrix cracking and fiber–matrix decohesion. In this framework, the agreement between commercial AE features and the independently derived shape and physics pipelines provides a robust validation of the proposed methodology, confirming that the extracted damage indices are not merely numerical constructs but reflect genuine physical changes in the material response. A summary of the main PLB results are presented in Table 6.3.

Table 6.3: Summary of the main PLB damage signatures observed after UV exposure.

Specimen	Dominant trend	Interpretation
41	Spectral modification with limited or positive energy variation	Possible modification of wave propagation with moderate attenuation; response is strongest in configuration B.
42	Strong reduction of energy and RMS	Increased attenuation and reduced efficiency of elastic-wave transmission after UV exposure.
43	Progressive energy decrease from post40 to post80, especially in configuration B	Cumulative degradation affecting transmission along the through-thickness path.
44	Strong energy reduction and variable spectral response	Significant material evolution with possible contribution from local heterogeneity and multiple damage mechanisms.

6.4 Acousto-Ultrasonic test

The Acousto-Ultrasonic method represents the active counterpart of AE. Instead of relying on spontaneous emission events, elastic waves are actively injected into the material using piezoelectric transducers operating as pulsers [48]. Physically, the AU method probes the dynamic elastic response of the material. The transmitted signal amplitude, energy and frequency content are directly influenced by internal scattering, absorption and mode conversion processes. Radiation-induced microstructural damage modifies these processes by increasing internal heterogeneity and dissipation, leading to measurable changes in the transmitted waveforms.

Unlike conventional ultrasonic testing, which typically focuses on time-of-flight and bulk velocity measurements, the AU approach emphasises global signal characteristics such as energy, spectral distribution and waveform complexity. This makes it particularly sensitive to distributed micro-damage, rather than to isolated macroscopic defects.

The transmitted signals are then recorded by receiving sensor placed at different position. In this configuration, one sensor acts as a transmitter and the other as a receiver, allowing the direct measurement of wave transmission properties across the specimen. By alternating the roles of the sensors, two independent transmission

paths are obtained, enabling the definition of cross-attenuation metrics. The two piezoelectric sensors, labelled S_1 and S_2, were positioned at a distance of 2.5 cm from the smaller edge of the specimen. Two experimental configurations were investigated. In configuration A, both sensors were placed on surface A. In configuration B, sensor S_1 was positioned on surface B, while sensor S_2 remained on surface A.

For each configuration, each sensor alternately acted as transmitter and receiver, generating and acquiring a total of 10 signals with a pulse width of 5 μs and a pulse interval of 100 ms. The recorded waveforms consist of: 10 signals transmitted by S_1 (denoted as $S_{1,sent}$), 10 signals received by S_1 originating from the emission of S_2 ($S_{1,rec}$), 10 signals transmitted by S_2 ($S_{2,sent}$), and 10 signals received by S_2 originating from the emission of S_1 ($S_{2,rec}$).

6.4.1 AU AEwin features

The first level of the analysis concentrates on a hit-level analysis framework aimed at quantifying global transmission variations and UV-induced damage through parametric acoustic emission (AE) descriptors. This approach operates directly on event-level features provided by the acquisition system (AMP, ENERGY, DURATION, COUNTS), thus focusing on the macroscopic propagation response of the specimen. The AEWin software provided a file with the average values of the AE features for the 10 hits sent and received from the two pulsers.

Raw acquisition files are scanned and interpreted according to a pulser–receiver geometry. For each pulser index, corresponding receiver entries are extracted and organized into a tabular format including specimen identifier, configuration, and irradiation stage (pre, post40, post80). Then a symmetric global transmission loss estimator is constructed. For each specimen, configuration, and stage, four ordered measurements are identified: two excitations (sent1, sent2) and two receptions (rec1, rec2). For every feature $S \in \{\mathrm{AMP}, \mathrm{ENERGY}, \mathrm{DURATION}, \mathrm{COUNTS}\}$, a bidirectional loss observable is defined as

$$L_S = \frac{1}{2}\left(\frac{S_{2,rec}}{S_{1,sent}} + \frac{S_{1,rec}}{S_{2,sent}}\right), \tag{6.15}$$

This formulation reduces directional bias and compensates for asymmetries in excitation strength, yielding a geometry-independent propagation metric. Conceptually, L_S represents the effective transmission efficiency of the specimen for a given physical descriptor.

Subsequently, a normalized Damage Index (DI) is introduced, defined as

$$DI_S = \frac{L_S^{\mathrm{post}}}{L_S^{\mathrm{pre}}}, \tag{6.16}$$

isolating structural evolution from absolute scaling factors. By referencing each post-irradiation stage to its pre-irradiation baseline, the analysis suppresses systematic instrumental effects and emphasizes relative modifications induced by UV exposure. Values of DI_L significantly different from unity indicate radiation-induced modifications of the corresponding physical quantity. In particular a DI close to 1 indicates that the signal transmission remains largely unchanged after UV exposure,

suggesting minimal impact on the material or configuration. Values greater than 1 indicate an increase in loss, i.e., the received signal is attenuated more after irradiation, revealing UV-induced degradation or micro-damage. Conversely, DI values below 1 suggest a reduction in loss, which may occur if the material properties or geometry favor signal transmission post-irradiation.

Beyond numerical computation, Heatmaps are generated by pivoting the loss and damage indices over specimen and configuration axes, enabling rapid identification of spatial or configurational trends.

Table 6.4: AU test: damage index based on transmission loss

Specimen	$\text{Config}_{post/pre}$	DI_{AMP}	DI_{ENERGY}	$\text{DI}_{DURATION}$	DI_{COUNTS}
41	$\text{A}_{post40/pre}$	0.978	1.164	2.326	1.708
41	$\text{B}_{post40/pre}$	0.956	1.149	1.708	1.572
42	$\text{A}_{post40/pre}$	1.023	2.325	1.804	1.546
42	$\text{B}_{post40/pre}$	0.954	1.125	2.099	1.881
43	$\text{A}_{post40/pre}$	1.049	1.009	1.566	1.381
43	$\text{A}_{post80/pre}$	1.114	1.572	1.846	1.402
43	$\text{B}_{post40/pre}$	0.963	1.007	1.573	1.512
43	$\text{B}_{post80/pre}$	0.985	1.493	1.600	1.612
44	$\text{A}_{post40/pre}$	1.077	1.772	1.725	1.289
44	$\text{A}_{post80/pre}$	1.038	1.331	2.004	1.412
44	$\text{B}_{post40/pre}$	1.061	2.011	1.771	1.474
44	$\text{B}_{post80/pre}$	1.038	1.879	1.881	1.625

In the appendix it is possible to find the Table A.4 with the values of the transmission loss for each feature.

In the Table 6.4 the values of the damage indices for each feature are presented.

The analysis of transmission loss and DI clearly highlights the effects of UV irradiation on the features of the AE signals. In all specimens and configurations, both **DURATION** and **COUNTS** exhibit a consistent increase after the first irradiation cycle (40 h), with a further increment after the second cycle (80 h, where available). This monotonic behaviour strongly suggests a progressive modification of the signal temporal structure induced by cumulative UV exposure.

On the contrary, the **amplitude** remains on average very close to unity for all samples and conditions, indicating that the peak signal magnitude is only marginally affected by irradiation. This implies that the UV damage does not significantly alter the instantaneous coupling or the maximum transduction efficiency of the sensors.

The **energy** shows a systematic increase after irradiation, coherently with the observed elongation in time and the higher number of threshold crossings. The increase in ENERGY is therefore mainly driven by the temporal broadening of the signals rather than by a change in peak amplitude.

Overall, these results indicate that UV irradiation primarily affects the *temporal dynamics* of acoustic emission signals, producing longer and more structured waveforms, while leaving their maximum amplitude largely unchanged.

6.4.2 AU Waveform-processing strategy

In the second level of the analysis we use the waveform to extract key features (frequency centroid, bandwidth, HF/HL, energy, RMS) through the two pipelines (shape and energy).

The acquisition program records 10 waveforms for each hit, both sent and received by the two pulsers. Raw waveforms are imported, validated, and classified according to specimen, side, state (pre, post40, post80), and acquisition role (sent1, rec1, rec2, sent2). Each signal undergoes deterministic preprocessing consisting of detrending and band-pass filtering in the 200–750 kHz range, ensuring removal of low-frequency drift and out-of-band noise while preserving the physically meaningful AE content. This guarantees spectral consistency across acquisition campaigns.

Two parallel feature-extraction pipelines are implemented. The *shape pipeline* focuses on spectral morphology: after Hann windowing and amplitude normalization, it extracts the spectral centroid (f_c), effective bandwidth (5%–95% cumulative energy), and the high-frequency to low-frequency power ratio (HF/LF). Looking at the Figure 6.3 representing the spectral density, the threshold between low and high frequencies was chosen at 300kHz. These descriptors capture frequency redistribu-

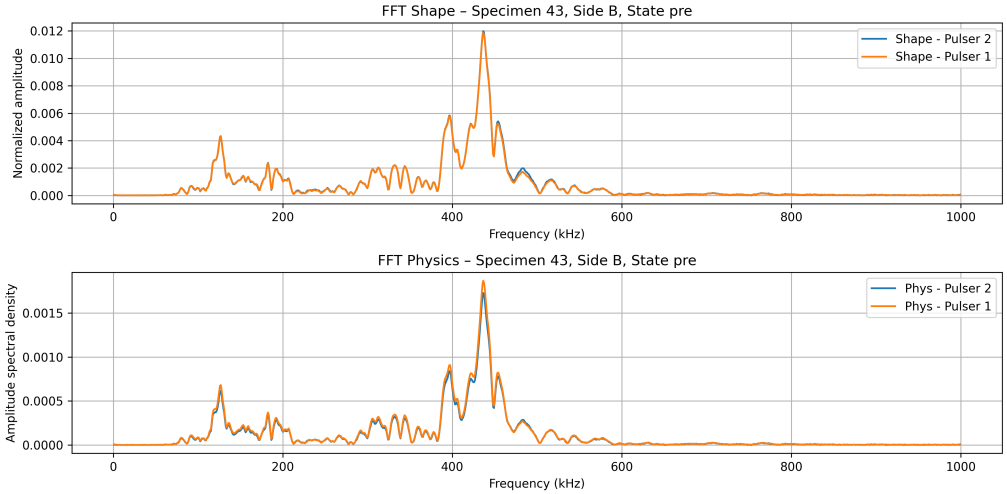

Figure 6.3: AU test: representative frequency spectrum of the pulser excitation used in the active transmission measurements. The observed spectral content motivates the adopted analysis band of 200–750 kHz and the choice of 300 kHz as the threshold separating low- and high-frequency components in the H/L and R_E indicators.

tion effects typically associated with microstructural modifications. On the other hand, the *physics pipeline* preserves amplitude information and computes energetically meaningful quantities, namely total time-domain energy (E), RMS amplitude, and an energy-based HF/LF ratio. This branch is intentionally not normalized in amplitude, as it aims to retain physically interpretable metrics directly related to attenuation and dissipation mechanisms. After aggregating repeated acquisitions and computing mean values and unbiased standard deviations for each sensor role, a symmetric transmission-loss estimator is then constructed as defined in 6.15. Then a dimensionless DI is constructed for each feature.

AU test results

In the appendix it is possible to find Table A.5 and A.6, which show the results obtained from the two pipeline analysis.

Table 6.5: AU test: damage Index on the transmission loss post/pre.

Specimen	$Config_{post/pre}$	DI(f_c)	DI(BW)	DI(H/L)	DI(E)	DI(RMS)	DI(R_E)
41	A_{post40}	0.99	0.99	0.52	0.93	0.99	1.62
41	B_{post40}	1.24	1.12	1.82	0.90	0.98	0.03
42	A_{post40}	1.21	0.67	6.01	3.15	1.79	2.46
42	B_{post40}	1.04	0.93	0.84	0.79	0.90	0.98
43	A_{post40}	0.91	1.03	0.15	0.70	0.88	0.15
43	A_{post80}	1.14	1.47	0.50	2.43	1.64	0.27
43	B_{post40}	0.97	1.09	0.18	0.56	0.79	0.65
43	B_{post80}	1.03	1.12	0.55	1.62	1.34	0.58
44	A_{post40}	1.14	0.85	5.34	2.76	1.69	1.00
44	A_{post80}	0.98	1.08	0.65	1.79	1.36	0.32
44	B_{post40}	1.15	0.88	4.94	2.53	1.60	1.67
44	B_{post80}	1.21	0.62	5.82	2.22	1.52	5.16

Table 6.5 reports the Damage Index computed from the transmission loss, while Figure 6.4 provides a synthetic visualization with heat maps.

For the **shape pipeline**, DI(f_c) remains close to unity for most specimens, indicating that the central spectral frequency is largely preserved after UV exposure. In contrast, DI(BW) and DI(H/L) exhibit larger deviations, reflecting modifications in spectral distribution. In particular, specimens 44 and 42 show pronounced variations in DI(H/L), evidencing a significant alteration of the high-to-low frequency balance. Specimen 43 display a progressive evolution between post40 and post80, consistent with cumulative spectral redistribution.

The **physics pipeline** provides complementary information. DI(E) and DI(RMS) highlight substantial energetic variations in selected configurations, such as 42 post40 and 43 post80. These increases indicate enhanced signal energy transmission or reduced dissipation, while DI values below unity reflect attenuation effects. The energy-based ratio DI(R_E) follows trends consistent with DI(H/L), confirming that spectral redistribution is accompanied by corresponding energetic changes.

Although the Damage Index is computed differently in the waveform pipelines (feature-based) and in the statistical transmission loss analysis (loss-based), the trends remain physically consistent. An increase in transmission loss ($\mathrm{DI}_{ENERGY} > 1$) corresponds to a reduction in effective transmitted energy, while feature-based DI(E) < 1 reflects the same attenuation from a direct waveform perspective. The agreement between these independent estimators confirms the robustness of the methodology.

6.4.3 Conclusion of AU test

The comparison between the waveform-based pipelines (shape and physics) and the hit-based analysis demonstrates strong internal consistency across all specimens

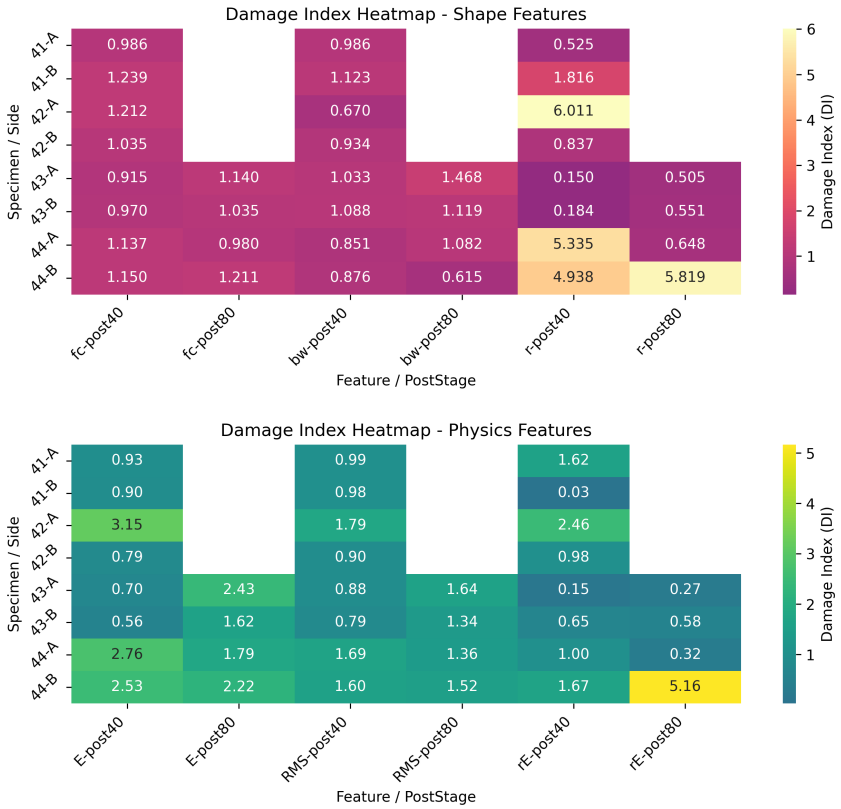

Figure 6.4: AU test: heat maps of the waveform-based damage indices obtained from the active transmission measurements. The upper panel reports the shape-pipeline indices, which describe changes in spectral morphology, while the lower panel reports the physics-pipeline indices, which preserve amplitude information and quantify changes in transmitted energy. The comparison between configurations A and B allows the sensitivity of surface and through-thickness propagation paths to UV-induced degradation to be assessed.

and configurations. Despite their different formulations, all approaches identify configuration B as generally more sensitive to UV-induced degradation. Temporal evolution from post40 to post80 confirms cumulative damage in selected specimens, particularly 43 and 44. The AU test therefore, proves to be a robust non-destructive technique capable of detecting both early spectral modifications and progressive energetic changes associated with microstructural degradation. A summary of the main AU results are presented in Table 6.6.

Table 6.6: Summary of the main AU damage signatures observed after UV exposure.

Specimen	Dominant trend	Interpretation
41	Moderate, configuration-dependent variations	Limited degradation or weak sensitivity of the selected propagation path.
42	Strong post40 variation, especially in configuration A	Localized modification of transmission properties after the first exposure cycle.
43	Clear evolution between post40 and post80	Progressive material evolution with cumulative UV exposure.
44	Large changes in energy and high-to-low frequency ratio	Strong modification of wave transmission and spectral redistribution.

6.5 Limitations and interpretation of the UV-ageing study

The results of this chapter should be interpreted as a sensitivity study of acoustic diagnostics to controlled UV-induced degradation, rather than as a direct qualification of the material for the complete radiation environment of a future detector or spacecraft. UV irradiation mainly induces surface-dominated photo-oxidation and matrix degradation, whereas high-energy particles and gamma radiation can produce bulk ionization, displacement damage and different dose-depth profiles. Therefore, the observed acoustic signatures cannot be directly extrapolated to ionizing-radiation damage without dedicated irradiation campaigns using representative particles and doses.

Additional limitations arise from the limited number of specimens, the intrinsic variability of composite laminates, possible differences in sensor coupling between pre- and post-irradiation measurements, and the absence of destructive post-mortem validation such as microscopy, interlaminar shear tests or chemical spectroscopy. The proposed damage indices should therefore be considered diagnostic indicators of material evolution, not absolute measures of residual mechanical strength.

6.6 Summary

This chapter investigated the use of acoustic-based non-destructive methods to detect UV-induced degradation in Carbon/Benzoxazine composite specimens. The

study was motivated by the need to monitor the long-term stability of lightweight composite structures relevant for drift chambers and other high-performance applications.

The PLB test showed that controlled UV exposure modifies the response to impulsive acoustic excitation. The observed changes affect both spectral shape and signal energy, with a strong dependence on specimen and propagation configuration. The AU test provided complementary information through controlled wave transmission, highlighting variations in duration, counts, energy and high-to-low frequency balance. Configuration B, in which waves propagate through the specimen thickness, was generally more sensitive to the imposed one-sided UV exposure.

The combined PLB and AU analyses indicate that acoustic diagnostics can detect measurable material evolution before visible macroscopic damage is reported. However, the results must be interpreted as a sensitivity study under controlled UV ageing, not as a complete qualification of the material for the full radiation environment of future detectors. The next step should combine acoustic monitoring with representative ionizing-radiation exposure and independent post-mortem validation, in order to establish a quantitative link between acoustic damage indices and residual mechanical performance.

Chapter 7

Cluster Counting for Particle Identification: A Key Feature of the INTREPID Drift Chamber

Particle identification (PID) is one of the most distinctive features of the INTREPID drift chamber and one of the main motivations for the development of this detector concept for future lepton colliders. In particular, the possibility of exploiting the cluster-counting technique in helium-based gas mixtures makes the INTREPID drift chamber a promising solution for combining an ultra-low material budget, precise tracking, and improved particle-identification capabilities. In gaseous trackers, PID has traditionally relied on the measurement of the specific ionization energy loss, $\mathrm{d}E/\mathrm{d}x$, from which information on the particle velocity, and hence on its mass, can be inferred when combined with the momentum measurement provided by the track curvature in a magnetic field. Although this method is robust and widely established, its performance is intrinsically limited by the large fluctuations of the deposited energy, which follow a Landau-like distribution due to primary-ionization statistics, gas-gain fluctuations, and the production of energetic δ-electrons. As a consequence, even after the application of truncated-mean estimators, the achievable separation power remains limited by the sizeable spread of the $\mathrm{d}E/\mathrm{d}x$ distribution [26], [53].

For this reason, the INTREPID drift chamber has been conceived to exploit the full potential of the cluster-counting technique. Rather than measuring the total deposited energy per unit length, this method aims at counting the number of primary ionization clusters per unit length, $\mathrm{d}N/\mathrm{d}x$ [54]. Since the formation of primary clusters is approximately governed by Poisson statistics, $\mathrm{d}N/\mathrm{d}x$ is expected to be less sensitive than $\mathrm{d}E/\mathrm{d}x$ to large ionization outliers and therefore to provide a significantly improved statistical resolution. This makes the technique especially attractive for next-generation lepton-collider experiments, where excellent PID performance must be achieved under stringent material-budget constraints.

The practical implementation of cluster counting in the INTREPID drift chamber, however, requires more than a purely theoretical or simulation-based study. Its performance depends on the possibility of resolving individual ionization peaks in real detector signals under realistic operating conditions and in the presence of effects such as diffusion, signal overlap, attachment, recombination, space charge,

and electronic noise. In helium-based mixtures, the temporal separation between signals generated by different primary ionization clusters can range from a few to a few tens of nanoseconds, but peak separability may be significantly degraded by transport effects and waveform overlap. For this reason, the experimental validation of cluster counting represents a crucial step in assessing the feasibility of the method for a large-scale detector such as the INTREPID drift chamber [26].

This chapter is therefore devoted to the beam-test activities carried out to investigate and validate the cluster-counting technique under conditions representative of the final detector operation. These measurements were aimed at characterizing the detector response to charged particles, studying the waveform structure in helium-based gas mixtures, testing reconstruction algorithms for cluster identification, and comparing the experimental observables with the expectations from analytical models and detailed simulations. In this perspective, the beam tests constitute the central element of the R&D programme, since they provide the essential link between the conceptual design of the INTREPID drift chamber and the demonstration of the potential particle-identification capabilities of the technique.

Before presenting the experimental setup, the data-analysis procedure, and the main beam-test results, a brief overview of the cluster-counting method and of its expected advantages with respect to the conventional $\mathrm{d}E/\mathrm{d}x$ approach is provided.

7.1 From $\mathrm{d}E/\mathrm{d}x$ to $\mathrm{d}N/\mathrm{d}x$: the cluster-counting technique

When a charged particle traverses matter, it undergoes a sequence of inelastic collisions with the atomic electrons of the medium. As a consequence, atoms can be either excited or ionized, while the incident particle loses part of its kinetic energy [18]. The measurement of this energy loss constitutes one of the standard tools for particle identification. In gaseous detectors, as well as in solid-state devices, the signal amplitude is proportional to the number of electron–ion pairs produced along the particle trajectory and therefore, on average, to the energy deposited in the active medium.

The distribution of the deposited energy is not Gaussian, but follows a Landau-like shape, as shown in Fig. 7.1. This characteristic behaviour arises from the non-negligible probability of large energy transfers in single collisions, which generate a pronounced high-energy tail, usually referred to as the *Landau tail*. As a result, the distribution is strongly asymmetric, and its mean value is significantly larger than its most probable value. For this reason, the arithmetic mean does not provide an optimal estimator of the energy deposition, and the truncated-mean method is commonly adopted [55]. In this approach, a fraction of the highest pulse-height samples is discarded in order to suppress the influence of rare but large fluctuations. The optimal truncation fraction depends on the detector configuration, the track length, and the adopted estimator, and is therefore determined empirically in each specific analysis.

The particle-separation power achievable with ionization measurements can be quantified in terms of the number of standard deviations between the response dis-

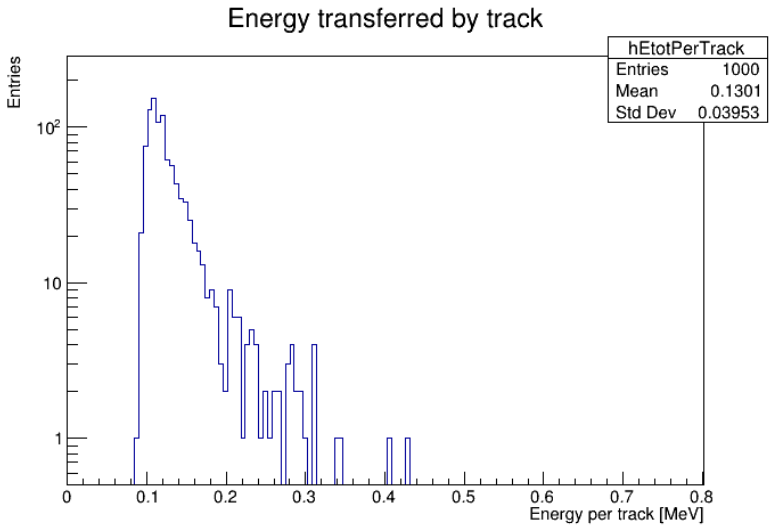

Figure 7.1: Garfield++ simulation of the energy-loss distribution for a muon crossing 200 drift cells of 1 cm length filled with a 90/10 He–iC_4H_{10} gas mixture. The asymmetric Landau-like tail illustrates the intrinsic limitation of charge-based dE/dx estimators and motivates the use of cluster counting.

tributions of two particle species, here denoted as p_1 and p_2, at the same momentum. It is defined as

$$n_\sigma^E = \frac{|\Delta_{p_1} - \Delta_{p_2}|}{\langle \sigma_{p_1,p_2} \rangle}, \tag{7.1}$$

where Δ_{p_1} and Δ_{p_2} represent the mean measured energy loss for the two particle species, and $\langle \sigma_{p_1,p_2} \rangle$ is the average energy-loss resolution, given by

$$\langle \sigma_{p_1,p_2} \rangle = \frac{\sigma_{E,p_1} + \sigma_{E,p_2}}{2}. \tag{7.2}$$

An alternative strategy for particle identification in gaseous detectors is provided by the *cluster-counting* technique. The underlying idea is that the energy-loss process is intrinsically discrete: as a charged particle crosses a gas volume, it produces a sequence of primary-ionization acts, each generating a cluster containing one or more electrons. The number of such primary ionization clusters follows, to a good approximation, Poisson statistics, since it results from the accumulation of a very large number of independent random processes [54].

This statistical property represents the main conceptual advantage of cluster counting. Indeed, the Gaussian limit of a Poisson distribution is already approached when the mean number of counts is of the order of 20, which corresponds to a track length of roughly 1 cm in commonly used gas mixtures. By contrast, the total energy-loss distribution approaches a Gaussian form only in thick and dense absorbers, where the central limit theorem becomes effective. Such a condition is clearly not suitable for ultra-light drift chambers, where minimizing the material budget is a primary requirement.

From an experimental point of view, the cluster-counting technique consists in identifying, within each recorded waveform, the isolated signal structures associated

with the arrival at the anode wire of the electrons produced in a single primary-ionization act. A schematic representation of the method is shown in Fig. 7.2 [56].

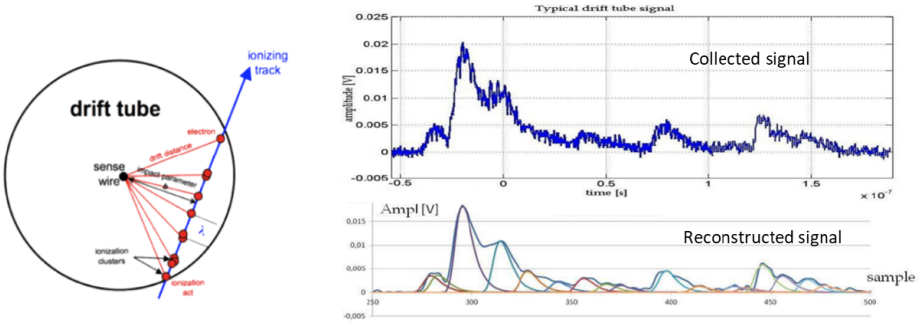

Figure 7.2: Principle of the cluster-counting method in a drift cell. Left: charged-particle track crossing the gas volume and producing discrete primary-ionization clusters. Right: corresponding waveform at the sense wire, where temporally resolved peaks can be associated with individual ionization electrons and grouped into primary clusters.

7.1.1 Analytical expectations for particle identification

The strong motivation for applying cluster counting to particle identification is already evident at the analytical level. Figure 7.3 shows the expected separation power, expressed in units of standard deviations, as a function of momentum for a gas mixture of 90% He and 10% iC_4H_{10} [26], [56]. In the upper panel, the solid curves correspond to the separation power obtained with the cluster-counting method, while the dashed curves refer to the optimal truncated-mean $\mathrm{d}E/\mathrm{d}x$ technique. The calculations assume a cluster-counting efficiency of 80%.

The improvement arises from the more favourable statistical behaviour of the primary-cluster multiplicity with respect to the deposited energy. While the truncated-mean $\mathrm{d}E/\mathrm{d}x$ observable remains affected by the residual influence of the Landau tail, the $\mathrm{d}N/\mathrm{d}x$ observable benefits from a nearly Poissonian scaling of the variance. As a consequence, the analytical expectation is a gain in separation power of about a factor of two over a broad momentum interval of interest for future lepton colliders.

These estimates, however, rely on the assumption that individual ionization clusters can be identified with sufficiently high efficiency and purity in realistic detector signals. Verifying this condition experimentally is the central objective of the beam-test campaign described in the following sections.

7.2 Beam-test campaign for the experimental validation of cluster counting

The experimental validation of the cluster-counting technique was carried out through a dedicated beam-test programme designed to study the method under realistic operating conditions and over the momentum range relevant for particle identification at future lepton colliders. The campaign provided the essential experimental link

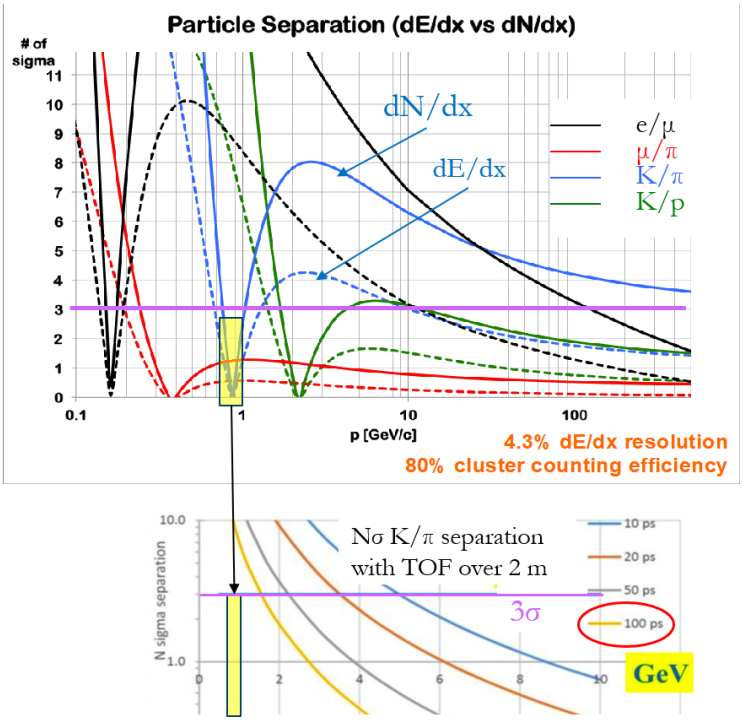

Figure 7.3: Analytical expectation for particle-separation power in a 90/10 He–iC_4H_{10} gas mixture. Top: comparison between cluster-counting separation power (solid curves) and optimized truncated-mean dE/dx separation power (dashed curves). Bottom: ratio between the two methods, showing the expected gain obtained from the more favourable statistics of primary-cluster counting.

between analytical expectations, detailed Garfield++/Geant4 simulations, and real detector signals.

It should be stressed that the beam-test programme does not constitute a direct performance measurement of the full INTREPID drift chamber. Rather, it provides an experimental validation of the cluster-counting method on controlled prototype configurations that reproduce the relevant signal-formation mechanisms and allow the key detector and reconstruction parameters to be scanned systematically. The extrapolation to the full detector therefore relies on the assumption that the physical processes governing peak formation and cluster reconstruction remain the same, while additional large-scale effects such as longer wires, higher capacitances, occupancy, common-mode noise, and system integration must still be addressed separately.

7.2.1 Beam-test campaign and scan strategy

The beam-test programme was conceived not only to compare the particle-identification performance achievable with the conventional $\mathrm{d}E/\mathrm{d}x$ observable and with the cluster-counting quantity $\mathrm{d}N/\mathrm{d}x$, but also to investigate the physical basis of cluster counting and to optimize its practical implementation. In particular, the campaign aimed to verify the Poisson nature of primary-cluster production, study its dependence on the $\beta\gamma$ of the ionizing particle, benchmark peak-finding and clusterization algorithms, and identify the detector and operating parameters that most strongly affect the counting efficiency. Special attention was devoted to potentially limiting effects, such as finite cluster size, signal overlap, space-charge distortions, and electron–ion recombination.

To address these goals, an extensive experimental scan was performed over the main detector and operating parameters. The study included different cell sizes, sense-wire diameters, gas mixtures, gas gains, electric-field configurations, and beam angles with respect to the wire orientation. The dependence of the cluster-counting efficiency on ionization density, ionization path length, and gas gain was investigated explicitly, and two dedicated peak-finding approaches, namely DERIV and RTA, were compared under different operating conditions. The tests also included scans of the RTA pulse-template parameters and configuration-dependent optimizations of the clusterization cuts [15].

The beam tests were carried out at CERN in several stages in order to cover complementary regions of the Bethe–Bloch curve. The first measurements were performed at the SPS H8 beam line in November 2021 and July 2022, using muons with momenta between 40 and 180 GeV/c, corresponding to the Fermi-plateau region. These were followed by campaigns at the PS T10 beam line in July 2023 and July 2024, where muons in the 2–10 GeV/c range were used to probe the relativistic-rise region, which is particularly relevant for particle-identification studies. The CERN measurements were complemented by earlier pioneering studies performed at PSI [57]. Overall, the explored $\beta\gamma$ range covers the momentum intervals of greatest interest for PID applications at future lepton colliders, as shown in Fig. 7.4.

Garfield++ is a powerful tool for describing in detail the physical properties and response of individual drift-chamber cells, but it is not well suited to the simulation

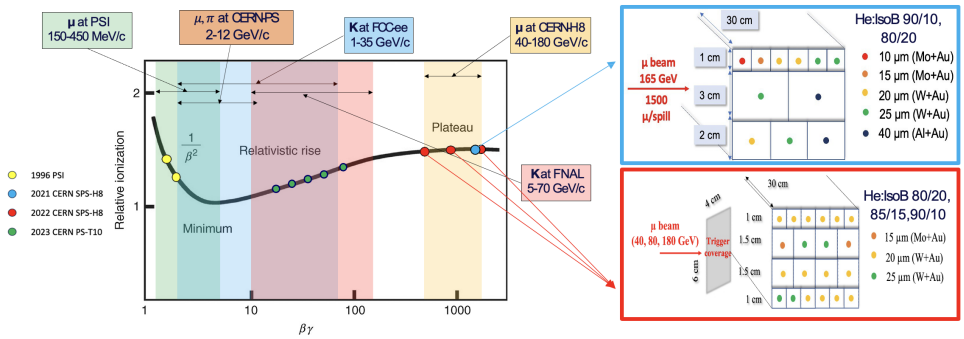

Figure 7.4: Beam-test momentum coverage superimposed on a representative Bethe–Bloch curve. The CERN SPS and PS campaigns probe complementary $\beta\gamma$ regions, including the relativistic-rise and Fermi-plateau domains relevant for validating cluster counting as a particle-identification technique.

of large-scale detectors or full collider events. Geant4, by contrast, is designed to model the interaction of particles with the material of a complete detector and is therefore appropriate for full-event simulations. However, in this framework the response of sensitive detector elements such as drift cells cannot be described from first principles with the same level of detail as in Garfield++, and must instead be parameterized or modeled through dedicated *ad hoc* prescriptions.

In this context, the beam tests represent the central validation step of the R&D programme, since they make it possible to quantify the actual performance of cluster counting, optimize the reconstruction strategy, and define the operating conditions required for its application in the INTREPID drift chamber. Before discussing the detector configuration and the analysis procedure, it is worth summarizing the preparation, installation, and operation activities that were necessary to validate the setup and ensure stable data taking during the beam-test campaign.

7.2.2 Preparation, commissioning, and operation of the beam-test setup

The beam-test activities described in this chapter were carried out within a broader collaborative effort. Within this framework, my direct contribution covered not only the preparation and commissioning of the experimental apparatus, but also its installation, operation during the beam test, and participation in data taking.

A significant part of this work concerned the construction, qualification, and validation of more than 20 drift tubes for the test beam campaign of 2023 and 2024. In particular, the preparation of the tubes required a dedicated wiring procedure based on the crimping of ultra-thin sense wires (see Figure 7.5 - left). The wires consisted of 20 μm gold-plated tungsten and were tensioned to 30 g using a digital dynamometer in order to ensure reproducible mechanical conditions. After wiring, the tubes were sealed with a two-component sealant to guarantee gas tightness and long-term stability. Gas-tightness tests were also performed on each tube before connection to the gas distribution line.

The tubes were integrated into the gas-flow system and operated with a He/iC_4H_{10} 90/10 gas mixture. On one side, the tubes were connected to the high-voltage dis-

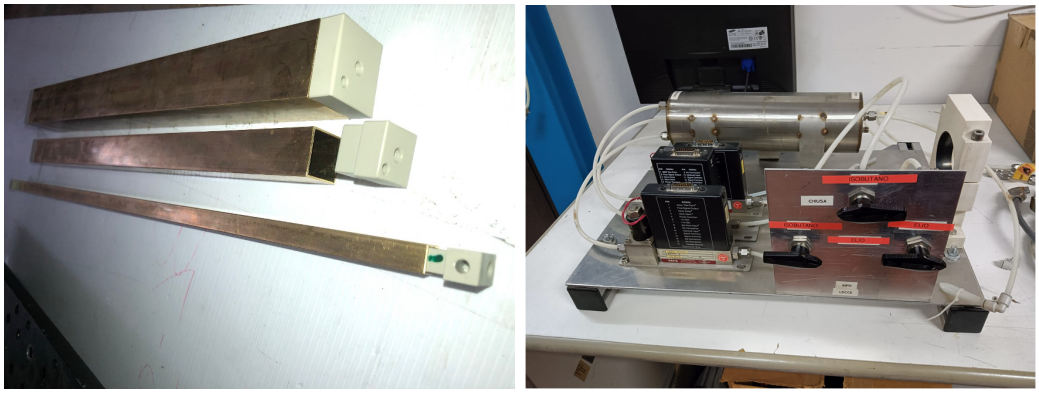

Figure 7.5: Preparation infrastructure for the drift-tube beam-test campaign. Left: set of brass drift tubes with different cell sizes and sense-wire configurations used to scan cluster-counting performance. Right: portable gas system used to monitor and regulate the He–iC_4H_{10} mixture supplied to the tubes during commissioning and data taking.

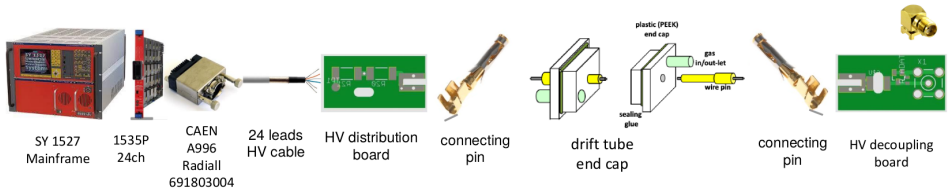

Figure 7.6: Electrical-connection scheme of the beam-test drift tubes. The sense wire is biased through the high-voltage distribution board, while the signal is extracted from the opposite side through a high-voltage decoupling board and transmitted to the waveform digitization chain.

tribution through a specific HV distribution board, while on the opposite side the signal was extracted through a dedicated HV decoupling board, both designed in the electronics workshop of the INFN Lecce Section. The entire chain is represented in Figure 7.6. The tubes were connected to an oscilloscope for waveform inspection and validation. This integration step was essential to ensure the correct operation of the detector, gas, high-voltage, and signal-readout systems before the start of data taking.

Before the beam-test campaign, the detector operating point was preliminarily investigated using cosmic muons. These measurements provided a first validation of the detector response under realistic operating conditions and allowed the stability of the setup, the signal quality, and the high-voltage operating region to be assessed prior to installation at the beam line.

My contribution then continued during the beam-test campaign itself, including the installation and commissioning of the setup at the experimental area, the verification of detector operation under beam conditions, and participation in data taking. This activity involved the monitoring of the detector response, the validation of the readout and high-voltage channels, and the handling of the setup during the running periods, in order to ensure stable and reliable data acquisition.

Overall, this work provided the experimental basis for the detector operation and for the data quality required for the beam-test studies and performance results discussed in the remainder of this chapter.

The quantitative cluster-counting performance results discussed in the following sections were obtained within the broader collaboration analysis framework. They are included here because they provide the detector-performance motivation and validation context for the mechanical and technological developments presented in this thesis.

7.2.3 Experimental setup and readout system

The experimental setup was designed as a compact, fully integrated system for the study of cluster counting in helium-based drift tubes. The configuration first implemented in the 2021 beam test was retained, with minor adaptations, in the subsequent campaigns. The detectors consisted of square-cross-section brass drift tubes with cell sizes ranging from 1.0 to 3.0 cm, equipped with sense wires of different diameters, from 10 to 40 μm. The tubes were operated with He–iC_4H_{10} gas mixtures of 90/10, 85/15, and 80/20, and with gas gains in the range $(1–5) \times 10^5$. This broad set of configurations was chosen to investigate the dependence of cluster-counting performance on geometry, gas composition, and amplification conditions. The setup used in the 2023 campaign is shown in Fig. 7.7.

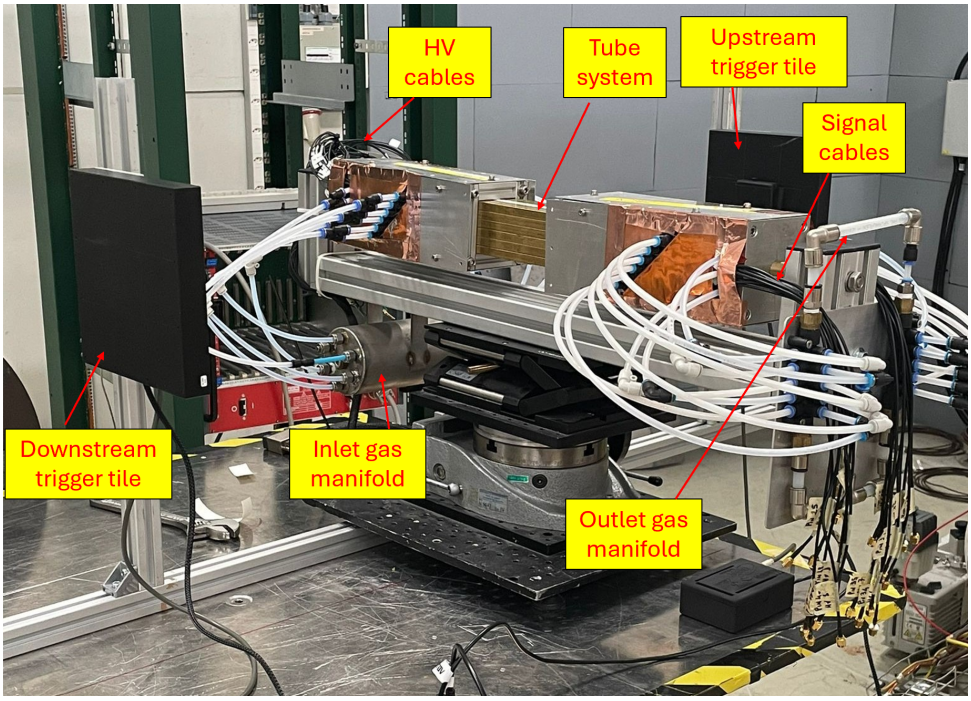

Figure 7.7: Experimental setup used for the cluster-counting beam-test campaign, viewed from the downstream side. The main components include the drift-tube array, trigger scintillators, gas distribution, high-voltage connections and waveform readout system used to acquire the fast signals required for peak and cluster reconstruction.

For each detector configuration, a preliminary gain calibration was performed as a function of the applied high voltage in order to identify a working region in which single-electron peaks were sufficiently visible while maintaining stable detector operation. The nominal operating point adopted in the subsequent scans corresponds to the voltage region where the reconstructed peak and cluster yields were found to

be stable and consistent with expectations. In this sense, the quoted gain interval should be regarded as an experimentally optimized window rather than as a purely nominal detector setting.

The sense wires were connected on one side to the high-voltage supply, while the opposite side was connected to a high-voltage decoupling termination card with a 330 Ω impedance, chosen to match the characteristic impedance of the drift tubes. Despite the relatively long coaxial cables, about 40 cm in the 2021 setup and 60 cm in the 2023 configuration, no preamplifiers were employed. The trigger was based on the coincidence of scintillators read out by silicon photomultipliers, while the gas system was regulated by mass-flow controllers under standard temperature and pressure conditions to ensure stable operation throughout the measurements.

Waveform acquisition was performed with the Wave Dream Board (WDB), used as the primary data-acquisition unit. The board provides 16 channels, variable-gain amplification, programmable pole-zero cancellation, FPGA-based trigger logic, and autonomous data readout via Gigabit Ethernet. Two onboard DRS4 chips, each coupled to an 8-channel ADC with 12-bit resolution, were operated in transparent mode, allowing continuous waveform sampling at rates up to 5 GSa/s through an analog ring buffer. This architecture was essential for direct access to the full time structure of the signals and, therefore, for the identification of individual electron peaks and primary ionization clusters.

A major advantage of this setup is that it isolates the cluster-counting problem from the additional complications associated with full tracking reconstruction. Since the drift path inside each tube is well defined and the beam conditions are externally controlled, the analysis can focus directly on the waveform time structure without requiring an internal tracking system. In this way, issues related to t_0 calibration, alignment, and time-to-distance conversion are largely avoided, and the study can concentrate on the reconstruction of ionization clusters in the time domain. This controlled configuration is particularly useful because it decouples the validation of the cluster-counting observable from the additional complexities of global track reconstruction. The price to pay is that the measured performance must be interpreted as an intrinsic single-cell or few-cell validation of the method, rather than as the final detector-level performance that will ultimately depend on large-scale integration effects.

7.2.4 Signal conditioning and gas-gain calibration

Before any peak-finding procedure was applied, the waveforms were baseline-corrected by subtracting the mean pulse height computed over an early time interval selected outside the signal acceptance window, typically the first ~ 30 ns of the trace. The residual waveform noise was quantified through the corresponding r.m.s. and was typically of the order of 1 mV. These quantities enter directly into the threshold definitions used for electron-peak selection.

A preliminary and essential step of the analysis was the determination of the gas gain as a function of the anode high voltage for each detector configuration. This calibration was performed by fitting the single-electron pulse-height distribution and extracting its most probable value. The extracted value was then corrected for

the amplifier gain, the mismatch between the characteristic impedance of the tube and the termination resistor, and the current-divider effect between the termination resistor and the ADC input impedance. The outcome of these scans showed that effective cluster counting requires operation in a gain window between 1×10^5 and 5×10^5, largely independent of the drift-tube geometry, wire diameter, and gas mixture [15].

7.2.5 Peak-finding algorithms and clusterization

Two complementary approaches were developed and validated to identify individual electron peaks in the drift-signal waveforms. The first, referred to as DERIV, is a derivative-based algorithm that uses the first and second discrete derivatives of the waveform to identify candidate peaks through a rising–falling pattern combined with noise-scaled thresholds and additional quality cuts. The second, referred to as RTA, is a running-template algorithm that iteratively matches the waveform to a predefined single-electron pulse template parameterized by the characteristic rise and fall times T_{rise} and T_{fall}.

In the present implementation, T_{rise} and T_{fall} are internal shape parameters of the template pulse, determined from calibration data at the nominal operating point and expressed in the same discrete units used by the waveform-sampling and template-matching procedure. Whenever the agreement metric exceeds a predefined threshold, a peak is identified, stored, and subtracted from the waveform before continuing the search.

A dedicated scan over different template shapes showed that the RTA performance is generally robust, with variations typically confined to the $\mathcal{O}(10\%)$ level when operating away from the nominal high-voltage point for which the parameters were optimized. A representative choice, $T_{\mathrm{rise}} = 0.5$ and $T_{\mathrm{fall}} = 1.3$, provided good agreement with the expected number of clusters over the explored operating conditions and was therefore adopted as the nominal configuration. A direct comparison between this RTA configuration and the DERIV algorithm yielded consistent results over the full high-voltage scan, confirming that both approaches are suitable for the reconstruction of electron peaks when properly tuned.

Peak finding yields a set of electron peaks, whereas cluster counting requires grouping peaks that originate from the same primary ionization act. For this purpose, a dedicated clusterization procedure was applied, in which temporally contiguous peaks with time separations compatible with diffusion-induced broadening were associated with the same primary cluster. For each cluster, the drift time and amplitude were assigned from the electron peak with the largest amplitude within the group, while the number of electrons per cluster was obtained from the multiplicity of peaks assigned to that cluster.

A representative consistency check was carried out for a 1.0 cm drift tube with drift length 0.8 cm and a track crossing angle of 45°, corresponding to an effective ionization length of 1.13 cm. Under these conditions, the expected number of primary ionization clusters can be estimated from the cluster density and from the appropriate $\beta\gamma$-dependent correction, while the expected number of reconstructed electron peaks depends additionally on the average number of electrons released per

primary cluster and on the peak-finding efficiency. In the considered configuration, the expected electron-peak multiplicity was estimated to be $N_{\text{peaks}} \approx 29.4$. After the subsequent clusterization stage, the reconstructed primary-cluster distributions were found to be compatible with Poisson statistics. This result is important because it shows that, although the measured waveform first yields electron peaks rather than primary clusters directly, the full reconstruction chain preserves the expected statistical behaviour of the primary-ionization process.

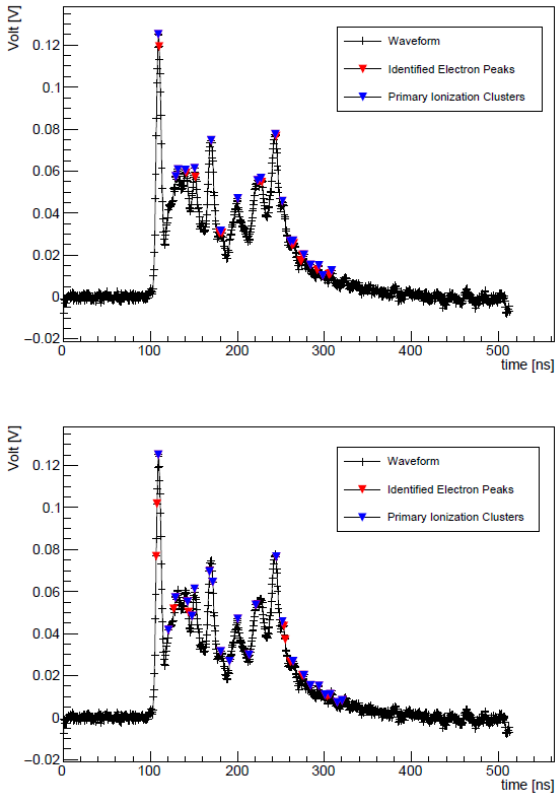

Figure 7.8: Example of electron-peak and cluster identification in a recorded drift-tube waveform for a 1 cm cell with a 20 μm sense wire, a 45° track angle, a 90/10 He–iC_4H_{10} gas mixture and a sampling rate of 2 GSa/s. The top panel shows the Running Template Algorithm (RTA), while the bottom panel shows the derivative-based algorithm (DERIV); red arrows indicate individual electron peaks and blue arrows indicate reconstructed clusters [15].

7.2.6 Dependence on operating parameters

The dependence of the cluster-counting performance on the main detector and operating parameters was investigated through dedicated scans. Since the gas mixture affects both the ionization density and the drift properties, the clusterization cuts were optimized separately for each mixture. The measured cluster densities confirmed that gas composition has a direct impact on the counting efficiency and must therefore be explicitly taken into account in the reconstruction tuning. For the two mixtures explicitly compared in the analysis, namely 90/10 and 80/20 He–iC_4H_{10}, the measured cluster densities were approximately 12.5 and 18 clusters/cm

per minimum-ionizing particle, respectively, in agreement with expectations.

The scaling of the reconstructed cluster count with ionization length was studied by varying the track angle with respect to the wire direction. A deficit in cluster counting was observed at normal incidence for the denser 80/20 mixture, a behaviour plausibly attributable to the onset of space-charge effects at higher ionization densities, which distort the electron drift and degrade the counting accuracy. At larger angles, performance deviations indicated that the reconstruction parameters must be retuned away from the nominal optimization point. The cluster-counting efficiency also showed a mild dependence on gas gain, with small under- or over-counting trends appearing when operating away from the nominal high-voltage point. This observation reinforces the need for gain-dependent calibrations and configuration-dependent parameterizations in a full detector environment.

7.2.7 Comparison between $\mathrm{d}E/\mathrm{d}x$ and $\mathrm{d}N/\mathrm{d}x$

A direct comparison between the conventional $\mathrm{d}E/\mathrm{d}x$ measurement and the cluster-counting observable $\mathrm{d}N/\mathrm{d}x$ was performed using identical tracks built from the same hits, corresponding to an effective track length of 2 m. More precisely, these tracks were not measured as continuous 2 m trajectories in the beam-test apparatus, but were constructed by combining statistically equivalent hits acquired under the same detector conditions so as to reproduce the ionization information expected for a longer effective path length. This procedure makes it possible to compare $\mathrm{d}E/\mathrm{d}x$ and $\mathrm{d}N/\mathrm{d}x$ on identical underlying hit samples, while avoiding geometrical ambiguities related to the compact prototype setup.

For the $\mathrm{d}E/\mathrm{d}x$ analysis, the charge deposited in the cells was processed using a truncated mean, in which the highest-charge samples, typically the top $\sim 20\%$, were discarded in order to suppress the Landau tail. For $\mathrm{d}N/\mathrm{d}x$, the RTA plus clusterization procedure was used to reconstruct the number of primary ionization clusters along the same tracks.

The comparison showed that the conventional $\mathrm{d}E/\mathrm{d}x$ observable achieves a resolution of about

$$\sigma(\mathrm{d}E/\mathrm{d}x) \simeq 5.7\%,$$

whereas the cluster-counting quantity yields

$$\sigma(\mathrm{d}N/\mathrm{d}x) \simeq 3.0\%.$$

Therefore, $\mathrm{d}N/\mathrm{d}x$ provides a resolution nearly twice as good as that obtained with $\mathrm{d}E/\mathrm{d}x$, in agreement with analytical expectations and simulation studies. The dependence on the track length L further highlights the more favourable statistical properties of cluster counting:

$$\sigma_{\mathrm{d}E/\mathrm{d}x} \propto L^{-0.37}, \qquad \sigma_{\mathrm{d}N/\mathrm{d}x} \propto L^{-1/2}.$$

The first scaling is consistent with the well-known Lehraus behaviour of truncated-mean ionization measurements [58], while the second reflects the expected Poisson-like scaling of the primary-cluster count. The resolution is evaluated for different track lengths, as shown in Figure 7.9, for both dE/dx and dN/dx methods.

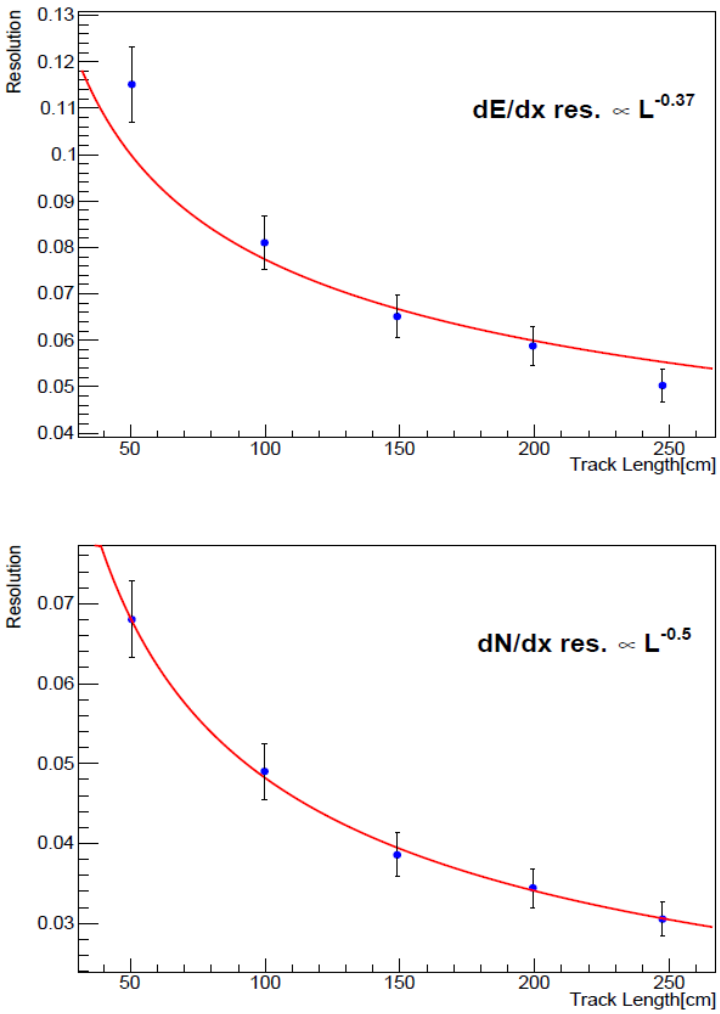

Figure 7.9: Ionization-resolution scaling with effective track length for conventional charge-based dE/dx and cluster-counting dN/dx estimators. The fitted trends follow approximately $L^{-0.37}$ for the truncated-mean dE/dx method and $L^{-1/2}$ for dN/dx, confirming the more favourable Poisson-like statistical behaviour of primary-cluster counting.

7.2.8 Resolution improvements: waveform cleaning and time-dependent corrections

Beyond the baseline implementation, two additional procedures were introduced to improve the $\mathrm{d}N/\mathrm{d}x$ resolution. The first was a waveform-cleaning step aimed at rejecting distorted, incomplete, or abnormally noisy signals, as well as events with unphysical cluster time spans. This selection reduced the contribution of spurious peaks and improved the $\mathrm{d}N/\mathrm{d}x$ resolution for 2 m tracks from approximately 3.0% to approximately 2.37%.

The second refinement addressed drift-time-dependent losses in the observed cluster yield, primarily attributable to electron attachment and, more generally, to transport or amplification effects that reduce the visibility of late-arriving ionization electrons. Since the observed number of clusters decreases with increasing drift time, a time-dependent correction was derived for each detector configuration by studying the average cluster yield as a function of an event drift-time estimator, such as the drift time of the earliest reconstructed cluster. The trend was parameterized with a first-order polynomial,

$$f(t) = a + b\,t, \tag{7.3}$$

from which the event-by-event correction factor was obtained as

$$\mathrm{cor}(t) = \frac{a}{a + b\,t_{\mathrm{evt}}}. \tag{7.4}$$

The corrected number of clusters was then defined as

$$N_{\mathrm{cl,corr}} = N_{\mathrm{cl}} \times \mathrm{cor}(t_{\mathrm{evt}}). \tag{7.5}$$

After applying both waveform cleaning and the time-dependent correction, the final $\mathrm{d}N/\mathrm{d}x$ resolution, evaluated over an effective track length of 2 m, improved further to about 2.28%. This corresponds to an overall gain of roughly a factor of 2.5 with respect to the conventional $\mathrm{d}E/\mathrm{d}x$ measurement for the same effective track length.

7.3 Implications for the INTREPID drift chamber

The results presented in this chapter provide a strong experimental validation of the cluster-counting technique in helium-based drift chambers and represent an important milestone for the INTREPID R&D programme. The study has shown that cluster counting is not only physically well founded, but also practically implementable with realistic detector configurations, modern waveform digitization, and dedicated reconstruction algorithms.

After discussing the physical motivation for replacing the conventional $\mathrm{d}E/\mathrm{d}x$ observable with the cluster-counting quantity $\mathrm{d}N/\mathrm{d}x$, the chapter examined the analytical expectations for the gain in particle-identification power and described the dedicated beam-test campaign carried out at CERN. The experimental setup, signal-conditioning procedure, and reconstruction strategy for electron-peak and cluster identification were presented in detail, together with the comparative use of the DERIV and RTA algorithms.

Note that the beam tests do not directly measure particle-separation power for different hadron species in the final detector configuration. Rather, they provide an experimental validation of the key ingredient underlying the expected PID improvement, namely the substantially better statistical resolution of $\mathrm{d}N/\mathrm{d}x$ with respect to $\mathrm{d}E/\mathrm{d}x$. The corresponding gain in separation power then follows from the analytical and simulation-based framework discussed in the first part of the chapter.

The experimental results validate both the statistical basis and the practical performance of the method. The reconstructed cluster distributions were found to be compatible with Poisson expectations, while the two peak-finding algorithms provided consistent and reliable results under different operating conditions. The dependence of the cluster-counting performance on gas composition, ionization density, track angle, and gas gain was also quantified, showing that the technique is robust but requires careful tuning of the reconstruction and operating parameters.

Most importantly, the comparison performed on identical tracks demonstrated that $\mathrm{d}N/\mathrm{d}x$ achieves a resolution of about 3.0%, significantly better than the 5.7% obtained with the conventional $\mathrm{d}E/\mathrm{d}x$ method. After the application of waveform-cleaning procedures and time-dependent corrections, the $\mathrm{d}N/\mathrm{d}x$ resolution improved further to about 2.28%. When interpreted within the analytical framework introduced at the beginning of the chapter, the measured $\mathrm{d}N/\mathrm{d}x$ resolution at the level of about 2.3% supports the expectation of a substantially enhanced separation power with respect to conventional $\mathrm{d}E/\mathrm{d}x$ over the momentum region of interest for future lepton-collider experiments.

From an instrumentation perspective, the beam tests also highlight an essential point: the performance of cluster counting depends on the optimization of the full signal chain, including front-end bandwidth, sampling strategy, impedance matching, gain calibration, peak finding, and clusterization. Preserving the fast signal components is crucial to maintain time-domain separability between nearby ionization electrons. When extrapolating the method to a large-scale detector such as the INTREPID drift chamber, the main challenge will be to preserve this separability in the presence of longer wires, larger capacitances, more complex grounding and noise conditions, and higher occupancies.

The observed sensitivity to gas gain and ionization density, including indications of possible space-charge-related counting deficits in denser mixtures, further suggests that a full detector implementation will require configuration-dependent calibrations and robust, possibly adaptive, peak-finding strategies. In addition, the improvements obtained through waveform cleaning and time-dependent corrections show that controlling detector effects can be as important as maximizing the raw peak-finding efficiency. In a full-scale drift chamber, analogous corrections are expected to depend on drift distance, local electric-field conditions, and environmental stability, thus motivating dedicated monitoring and calibration procedures.

The results of this chapter demonstrate that cluster counting provides a strong experimental basis for adoption in the INTREPID drift chamber. They support the use of $\mathrm{d}N/\mathrm{d}x$ as one of the key particle-identification observables of the detector and confirm that helium-based ultra-light drift chambers can combine excellent tracking capabilities with significantly enhanced particle-identification performance for future lepton-collider experiments.

A full detector implementation will require additional validation under conditions not reproduced by the beam-test tubes, including full-length wires, realistic input capacitance, final front-end electronics, grounding and shielding at detector scale, channel-to-channel cross talk, occupancy, and calibration stability over large numbers of cells.

Conclusions

This doctoral thesis investigated the design of ultralight drift chambers for future lepton colliders through an integrative strategy combining detector physics, mechanical design, finite element modeling, characterization of wires and composite materials, and experimental validation. Within the framework of the FCC-ee and CEPC programs, and with particular reference to the IDEA/INTREPID drift chamber concept, the work addressed a central problem for future tracking systems: combining low material consumption, mechanical stability, precise tracking, and particle identification capabilities within the same detection technology. Particular attention was paid to the role of lightweight composite materials as enabling structural elements for high-energy physics detectors and, more generally, for aerospace applications where low mass, dimensional stability, and resistance to hostile environments are simultaneous requirements.

A first major contribution concerned the mechanical design of the INTREPID drift-chamber endplate. The studies showed that the endplate cannot be treated as a purely structural component, because its deformation directly affects wire tension, wire positioning, electrostatic stability and, ultimately, tracking calibration. The refined single-spoke FEM model proved the efficiency of the stay-based tension-recovery concept: without stays the spoke deformation is mechanically unacceptable, whereas with 15 stays the maximum axial deformation is reduced to approximately 0.19 mm, compatible with the design-level target of about 0.2 mm. This result supports the feasibility of the proposed load-transfer concept, although it should still be regarded as a local design validation. A complete assessment will require full-endcap and full-chamber models including ring compliance, PCB and spacer stiffness, joints, barrel panels, realistic boundary conditions and manufacturing tolerances.

The CEPC-related studies provided a complementary design case based on a more conventional aluminum-endcap architecture. The thickness optimization indicated that, for the stepped geometry considered, a thickness of about 20 mm represents a reasonable compromise between stiffness and material budget, since further increases provide only limited mechanical benefit. A new concave endcap geometry was also investigated and showed improved stress and strain response in the simplified FEM model, even at a reduced thickness of 15 mm. However, this solution remains preliminary: the complete hole pattern, local feed-through details, machining feasibility, sealing interfaces and assembly constraints must be included before it can be considered a mature design option.

The mechanical characterization of ultra-thin wires provided experimental input for the definition of safe operating margins in drift-chamber construction. Tensile tests on 20 μm W–Au and Mo–Au wires and on carbon monofilaments allowed

the extraction of ultimate tensile strength, Young's modulus and proof-stress yield values. W–Au showed the highest strength and stiffness, confirming its suitability for sense-wire applications, while Mo–Au remains a mechanically viable alternative. The carbon monofilament showed a brittle-like response and significantly lower stiffness and strength, making it interesting as a low-mass field-wire candidate but not yet a detector-ready solution. Further studies on coated carbon wires, long-term creep, fatigue, humidity and corrosion are required before final adoption.

A further part of the thesis addressed the problem of radiation-tolerant composite materials, which is directly connected with the scope of this work. In an ultra-light drift chamber, composite structures are not only passive supports: they determine the material budget, dimensional stability and long-term reliability of the detector. Similar requirements are found in aerospace applications, where composite components must preserve their mechanical properties under severe environmental conditions. For this reason, non-destructive acoustic methods were investigated as diagnostic tools for detecting early degradation in lightweight composite materials.

Pencil Lead Break and Acousto-Ultrasonic tests were applied to UV-aged Carbon/Benzoxazine specimens, showing that acoustic waveforms are sensitive to changes in energy transmission, duration and spectral content after controlled exposure. These results indicate that acoustic diagnostics can detect early material evolution before visible macroscopic damage is observed. However, this study should be interpreted as a first diagnostic step toward the qualification of radiation-tolerant composite materials, not as a complete demonstration of radiation hardness. UV exposure does not reproduce the full ionizing-radiation environment expected in future detectors or space systems. Dedicated irradiation tests with representative particles, doses and dose rates, combined with microscopy and mechanical post-mortem validation, will be necessary to establish a quantitative link between acoustic damage indices and residual structural performance.

Finally, the thesis connected the mechanical and technological studies to the particle-identification motivation of the INTREPID drift chamber through the cluster-counting beam-test programme. Within this collaborative activity, my contribution concerned the preparation, commissioning and operation of drift-tube prototypes used in the experimental campaigns. The results obtained by the collaboration demonstrate that dN/dx can achieve a significantly better resolution than conventional charge-based dE/dx: for an effective track length of 2 m, the measured resolution improves from about 5.7% for dE/dx to about 3.0% for dN/dx, and further to approximately 2.28% after waveform cleaning and time-dependent corrections. These results provide experimental support for the use of cluster counting as a key PID observable in helium-based ultra-light drift chambers. Nevertheless, extrapolation to the full detector will require validation with full-length wires, realistic capacitances, final front-end electronics, grounding and shielding at detector scale, channel cross talk, occupancy and long-term calibration stability.

In conclusion, the work demonstrates that the design of next-generation drift chambers requires an integrated strategy in which detector requirements, structural mechanics, wire technology, composite-material durability and signal reconstruction are treated as coupled aspects of the same problem. The main contribution of this thesis lies in connecting these domains within a coherent R&D path. From

the high-energy-physics perspective, the results support the feasibility of ultra-light drift chambers as promising tracking and particle-identification systems for future precision experiments. From the materials and aerospace-engineering perspective, the acoustic characterization of UV-aged Carbon/Benzoxazine composites provides a methodological basis for monitoring early degradation in lightweight structural materials intended for harsh operating environments. The critical steps still required before a full detector implementation are complete mechanical modelling, prototype validation, coated-wire qualification, representative irradiation testing of composite materials and detector-scale validation of cluster-counting readout.

Appendix A

Detailed Acoustic and Acousto-Ultrasonic Data

This appendix reports the complete numerical datasets used for the acoustic analysis discussed in Chapter 6. The main chapter focuses on damage indices and physical interpretation, while the full AEwin and waveform-derived quantities are collected here for completeness and traceability.

Table A.1: PLB test: AEWin features for each configuration.

Specimen	Side	Counts	Energy (au)	Duration (μs)	Amplitude (dB)	FreqCentroid (kHz)	FreqPeak (kHz)
41	A_{pre}	98.00 ± 6.08	127.33 ± 17.62	696.67 ± 49.24	91.33 ± 3.06	291.67 ± 26.86	207.67 ± 5.86
41	A_{post40}	96.00 ± 9.00	132.00 ± 7.00	684.33 ± 58.31	90.33 ± 1.53	291.00 ± 9.85	191.00 ± 12.17
41	B_{pre}	104.33 ± 13.28	112.00 ± 35.59	702.33 ± 150.05	88.00 ± 2.65	294.00 ± 13.08	162.00 ± 0.00
41	B_{post40}	150.67 ± 3.06	129.67 ± 3.21	2536.00 ± 0.00	89.00 ± 0.00	247.00 ± 15.87	175.00 ± 0.00
42	A_{pre}	99.67 ± 3.79	157.00 ± 16.09	593.00 ± 17.06	89.00 ± 1.73	294.00 ± 7.21	190.00 ± 20.81
42	A_{post40}	107.00 ± 11.27	93.00 ± 9.54	1421.67 ± 106.45	86.67 ± 1.53	288.67 ± 11.15	263.67 ± 144.92
42	B_{pre}	102.00 ± 16.09	133.67 ± 24.99	732.00 ± 167.54	88.33 ± 1.53	277.33 ± 16.26	185.33 ± 23.29
42	B_{post40}	108.33 ± 22.50	76.67 ± 9.61	1484.67 ± 388.50	81.67 ± 1.53	261.67 ± 24.03	123.00 ± 2.00
43	A_{pre}	107.67 ± 2.52	126.67 ± 17.95	703.67 ± 28.04	87.00 ± 1.00	302.67 ± 13.87	187.00 ± 8.72
43	A_{post40}	103.00 ± 12.17	119.00 ± 10.58	1542.67 ± 233.23	87.67 ± 0.58	302.33 ± 10.02	169.67 ± 38.80
43	A_{post80}	101.00 ± 3.46	103.00 ± 18.52	562.67 ± 56.05	86.33 ± 1.15	281.67 ± 30.73	185.00 ± 5.29
43	B_{pre}	103.67 ± 5.03	165.33 ± 50.12	642.00 ± 57.56	91.00 ± 2.65	273.33 ± 6.35	193.00 ± 0.00
43	B_{post40}	138.67 ± 3.79	122.67 ± 10.69	1663.67 ± 127.69	87.33 ± 0.58	270.00 ± 10.82	196.33 ± 1.15
43	B_{post80}	77.33 ± 2.08	69.33 ± 10.12	430.00 ± 23.43	83.67 ± 1.15	264.33 ± 11.02	192.33 ± 1.15
44	A_{pre}	125.33 ± 7.51	205.00 ± 26.51	835.00 ± 75.32	89.33 ± 1.53	281.33 ± 15.31	175.00 ± 0.00
44	A_{post40}	107.00 ± 3.61	118.33 ± 9.45	775.33 ± 29.19	88.00 ± 0.00	308.00 ± 8.19	188.33 ± 1.15
44	A_{post80}	119.33 ± 2.08	86.67 ± 6.11	670.00 ± 31.75	84.33 ± 0.58	271.00 ± 20.81	156.00 ± 0.00
44	B_{pre}	120.00 ± 5.57	164.00 ± 11.53	774.67 ± 23.07	89.00 ± 1.00	309.33 ± 2.89	175.00 ± 0.00
44	B_{post40}	90.67 ± 5.51	96.67 ± 12.66	709.33 ± 114.12	87.00 ± 2.00	291.33 ± 25.17	201.00 ± 12.12
44	B_{post80}	105.00 ± 7.21	69.67 ± 5.03	637.00 ± 43.30	83.33 ± 0.58	264.67 ± 7.77	179.00 ± 10.39

Table A.2: PLB test: waveform analysis results - AE Shape features

Specimen	Side	f_c (kHz)	BW (kHz)	R
41	A_{pre}	241.45 ± 24.64	324.38 ± 22.51	0.331 ± 0.156
41	A_{post40}	222.79 ± 8.47	330.24 ± 19.49	0.217 ± 0.046
41	B_{pre}	239.08 ± 2.23	340.34 ± 10.13	0.331 ± 0.022
41	B_{post40}	191.67 ± 5.97	187.92 ± 78.21	0.050 ± 0.019
42	A_{pre}	220.62 ± 7.83	286.60 ± 5.31	0.169 ± 0.042
42	A_{post40}	232.11 ± 7.88	343.92 ± 11.81	0.302 ± 0.048
42	B_{pre}	214.94 ± 11.87	294.09 ± 15.94	0.152 ± 0.054
42	B_{post40}	192.12 ± 9.50	348.80 ± 23.18	0.150 ± 0.052
43	A_{pre}	239.21 ± 18.81	376.49 ± 2.44	0.320 ± 0.134
43	A_{post40}	251.19 ± 13.48	371.60 ± 4.67	0.405 ± 0.110
43	A_{post80}	217.71 ± 23.69	333.82 ± 35.33	0.208 ± 0.125
43	B_{pre}	208.50 ± 2.08	312.33 ± 11.40	0.104 ± 0.007
43	B_{post40}	207.78 ± 6.61	339.68 ± 6.45	0.115 ± 0.024
43	B_{post80}	200.02 ± 5.54	325.03 ± 15.48	0.117 ± 0.029
44	A_{pre}	197.43 ± 8.93	296.69 ± 34.24	0.117 ± 0.038
44	A_{post40}	245.04 ± 12.72	344.57 ± 3.94	0.389 ± 0.097
44	A_{post80}	197.42 ± 15.77	310.70 ± 38.32	0.142 ± 0.070
44	B_{pre}	226.28 ± 4.98	350.76 ± 2.88	0.259 ± 0.040
44	B_{post40}	233.75 ± 29.71	334.15 ± 4.79	0.313 ± 0.182
44	B_{post80}	203.09 ± 9.30	328.94 ± 2.56	0.168 ± 0.042

Table A.3: PLB test: waveform analysis results - AE Physics features

Specimen	Side	E (a.u.)	RMS	R_E
41	A_{pre}	63.20 ± 15.47	0.17 ± 0.02	0.331 ± 0.156
41	A_{post40}	68.36 ± 5.20	0.18 ± 0.01	0.217 ± 0.046
41	B_{pre}	48.47 ± 24.54	0.15 ± 0.04	0.331 ± 0.022
41	B_{post40}	63.14 ± 2.49	0.18 ± 0.00	0.050 ± 0.019
42	A_{pre}	93.57 ± 10.62	0.21 ± 0.01	0.169 ± 0.042
42	A_{post40}	29.73 ± 6.04	0.12 ± 0.01	0.302 ± 0.048
42	B_{pre}	73.22 ± 18.45	0.19 ± 0.02	0.152 ± 0.054
42	B_{post40}	19.26 ± 3.81	0.10 ± 0.01	0.150 ± 0.052
43	A_{pre}	57.14 ± 18.23	0.17 ± 0.03	0.320 ± 0.134
43	A_{post40}	53.91 ± 9.42	0.16 ± 0.01	0.405 ± 0.110
43	A_{post80}	47.22 ± 13.19	0.15 ± 0.02	0.208 ± 0.125
43	B_{pre}	116.25 ± 50.39	0.23 ± 0.06	0.104 ± 0.007
43	B_{post40}	52.32 ± 1.15	0.16 ± 0.00	0.115 ± 0.024
43	B_{post80}	24.48 ± 6.20	0.11 ± 0.01	0.117 ± 0.029
44	A_{pre}	115.26 ± 24.97	0.24 ± 0.03	0.117 ± 0.038
44	A_{post40}	50.48 ± 6.06	0.16 ± 0.01	0.389 ± 0.097
44	A_{post80}	28.20 ± 3.67	0.12 ± 0.01	0.142 ± 0.070
44	B_{pre}	71.10 ± 12.26	0.19 ± 0.02	0.259 ± 0.040
44	B_{post40}	35.98 ± 8.16	0.13 ± 0.02	0.313 ± 0.182
44	B_{post80}	20.69 ± 2.21	0.10 ± 0.01	0.168 ± 0.042

Table A.4: AU test: global transmission loss for each feature.

Specimen	Config_{stage}	Loss_{AMP}	Loss_{ENERGY}	$\text{Loss}_{DURATION}$	Loss_{COUNTS}
41	A_{post40}	0.667	0.049	0.918	0.800
41	A_{pre}	0.682	0.042	0.395	0.469
41	B_{post40}	0.657	0.062	0.739	0.737
41	B_{pre}	0.687	0.054	0.433	0.469
42	A_{post40}	0.667	0.066	0.808	0.766
42	A_{pre}	0.652	0.028	0.448	0.496
42	B_{post40}	0.626	0.043	0.953	0.773
42	B_{pre}	0.657	0.039	0.454	0.411
43	A_{post40}	0.652	0.041	0.864	0.827
43	A_{post80}	0.692	0.065	1.019	0.840
43	A_{pre}	0.621	0.041	0.552	0.599
43	B_{post40}	0.652	0.045	0.856	0.773
43	B_{post80}	0.667	0.067	0.871	0.824
43	B_{pre}	0.677	0.045	0.544	0.511
44	A_{post40}	0.707	0.071	0.795	0.688
44	A_{post80}	0.682	0.054	0.923	0.753
44	A_{pre}	0.657	0.040	0.461	0.534
44	B_{post40}	0.707	0.088	0.868	0.804
44	B_{post80}	0.692	0.082	0.922	0.887
44	B_{pre}	0.667	0.044	0.490	0.545

Table A.5: AU test: shape pipeline AE Loss features.

Specimen	$Config_{stage}$	$L(f_c)$	L(BW)	L(H/L)
41	A_{pre}	0.81 ± 0.01	0.44 ± 0.06	0.67 ± 0.22
41	A_{post40}	0.80 ± 0.02	0.43 ± 0.02	0.35 ± 0.04
41	B_{pre}	0.72 ± 0.01	0.48 ± 0.01	0.38 ± 0.05
41	B_{post40}	0.89 ± 0.01	0.54 ± 0.02	0.70 ± 0.07
42	A_{pre}	0.65 ± 0.02	0.60 ± 0.11	0.09 ± 0.03
42	A_{post40}	0.79 ± 0.02	0.40 ± 0.01	0.52 ± 0.04
42	B_{pre}	0.69 ± 0.01	0.60 ± 0.06	0.15 ± 0.02
42	B_{post40}	0.72 ± 0.01	0.56 ± 0.30	0.13 ± 0.03
43	A_{pre}	0.79 ± 0.01	0.48 ± 0.06	0.75 ± 0.21
43	A_{post40}	0.73 ± 0.01	0.50 ± 0.13	0.11 ± 0.04
43	A_{post80}	0.91 ± 0.00	0.70 ± 0.30	0.38 ± 0.13
43	B_{pre}	0.81 ± 0.02	0.44 ± 0.05	1.23 ± 0.37
43	B_{post40}	0.79 ± 0.00	0.48 ± 0.02	0.23 ± 0.02
43	B_{post80}	0.84 ± 0.00	0.49 ± 0.00	0.68 ± 0.01
44	A_{pre}	0.79 ± 0.02	0.48 ± 0.07	0.32 ± 0.09
44	A_{post40}	0.90 ± 0.00	0.41 ± 0.01	1.71 ± 0.57
44	A_{post80}	0.77 ± 0.01	0.52 ± 0.04	0.21 ± 0.04
44	B_{pre}	0.77 ± 0.01	0.51 ± 0.07	0.24 ± 0.06
44	B_{post40}	0.89 ± 0.01	0.45 ± 0.04	1.18 ± 0.12
44	B_{post80}	0.93 ± 0.00	0.31 ± 0.03	1.39 ± 0.39

Table A.6: AU test: physics pipeline AE Loss features.

Specimen	$Config_{stage}$	L(E)	L(RMS)	$L(R_E)$
41	A_{pre}	9.2e-04 ± 5.4e-06	2.9e-02 ± 8.0e-05	0.29 ± 0.02
41	A_{post40}	8.5e-04 ± 8.0e-06	2.9e-02 ± 1.3e-04	0.46 ± 0.02
41	B_{pre}	1.4e-03 ± 1.8e-05	3.6e-02 ± 2.7e-04	10.70 ± 0.17
41	B_{post40}	1.3e-03 ± 1.2e-05	3.5e-02 ± 1.9e-04	0.32 ± 0.01
42	A_{pre}	4.6e-04 ± 3.0e-06	2.1e-02 ± 6.4e-05	0.22 ± 0.02
42	A_{post40}	1.5e-03 ± 1.3e-05	3.8e-02 ± 1.8e-04	0.55 ± 0.02
42	B_{pre}	7.6e-04 ± 7.2e-06	2.7e-02 ± 1.1e-04	0.27 ± 0.01
42	B_{post40}	6.0e-04 ± 6.9e-06	2.4e-02 ± 1.4e-04	0.27 ± 0.04
43	A_{pre}	9.3e-04 ± 5.5e-06	2.9e-02 ± 8.2e-05	1.54 ± 0.01
43	A_{post40}	6.5e-04 ± 1.2e-05	2.6e-02 ± 2.4e-04	0.24 ± 0.00
43	A_{post80}	2.3e-03 ± 1.8e-05	4.7e-02 ± 1.8e-04	0.41 ± 0.02
43	B_{pre}	1.3e-03 ± 6.7e-06	3.4e-02 ± 8.8e-05	0.49 ± 0.01
43	B_{post40}	7.4e-04 ± 9.8e-06	2.7e-02 ± 1.8e-04	0.32 ± 0.02
43	B_{post80}	2.1e-03 ± 1.9e-05	4.6e-02 ± 1.9e-04	0.29 ± 0.01
44	A_{pre}	7.6e-04 ± 6.7e-06	2.7e-02 ± 1.2e-04	0.50 ± 0.03
44	A_{post40}	2.1e-03 ± 1.4e-05	4.6e-02 ± 1.5e-04	0.50 ± 0.02
44	A_{post80}	1.4e-03 ± 6.5e-06	3.7e-02 ± 8.4e-05	0.16 ± 0.01
44	B_{pre}	1.1e-03 ± 3.3e-06	3.3e-02 ± 5.1e-05	0.28 ± 0.02
44	B_{post40}	2.8e-03 ± 1.7e-05	5.2e-02 ± 1.5e-04	0.46 ± 0.01
44	B_{post80}	2.4e-03 ± 3.7e-05	4.9e-02 ± 3.6e-04	1.42 ± 0.06

List of Publications

The research activity carried out during the PhD has contributed to the production of the following publications.

A. Publications indexed in Web of Science and Scopus

1. Elmetenawee, W., Abbrescia, M., Anwar, M., Corvaglia, A., D'Anzi, B., De Filippis, N., De Santis, F., Gorini, E., Grancagnolo, F., Gravili, F., Louka, M., Miccoli, A., Panareo, M., Primavera, M., Procacci, F., Ventura, A., *Enhancing Particle Identification in Helium-Based Drift Chambers Using Cluster Counting: Insights from Beam Test Studies*, *Journal of Instrumentation* **20** (2025), P11019. DOI: 10.1088/1748-0221/20/11/P11019. WoSUID: WOS:001629006600001.

2. Elmetenawee, W., Abbrescia, M., Anwar, M., Corvaglia, A., D'Anzi, B., De Filippis, N., De Santis, F., Gorini, E., Grancagnolo, F., Gravili, F., Louka, M., Miccoli, A., Panareo, M., Primavera, M., Procacci, F., Ventura, A., *Advancing Particle Identification in Helium-Based Drift Chambers: A Cluster Counting Technique Study through Beam Tests*, *Proceedings of Science* **476** (2025), 1067. Scopus EID: 2-s2.0-105004823495.

3. Benedikt, M., Zimmermann, F., Auchmann, B., et al., *Future Circular Collider Feasibility Study Report: Volume 1 Physics, Experiments, Detectors*, *European Physical Journal C* **85** (2025), 1468. DOI: 10.1140/epjc/s10052-025-15077-x. Scopus EID: 2-s2.0-105027262408. Author list includes Francesco Massimiliano Procacci.

4. Benedikt, M., Zimmermann, F., Auchmann, B., et al., *Future Circular Collider Feasibility Study Report: Volume 2 Accelerators, Technical Infrastructure and Safety*, *European Physical Journal: Special Topics* **234** (2025), 5713–6197. DOI: 10.1140/epjs/s11734-025-01967-4. Scopus EID: 2-s2.0-105031762732. Author list includes Francesco Massimiliano Procacci.

5. Benedikt, M., Zimmermann, F., Auchmann, B., et al., *Future Circular Collider Feasibility Study Report: Volume 3 Civil Engineering, Implementation and Sustainability*, *European Physical Journal: Special Topics* (2025), article in press. DOI: 10.1140/epjs/s11734-025-01958-5. Scopus EID: 2-s2.0-105018825483. Author list includes Francesco Massimiliano Procacci.

6. Abbrescia, M., Anwar, M., Corvaglia, A., D'Anzi, B., De Filippis, N., De Santis, F., Elmetenawee, W., Gorini, E., Grancagnolo, F., Gravili, F., Louka, M., Miccoli, A., Panareo, M., Primavera, M., Procacci, F., Ventura, A., *Advancements in Tracking Techniques for Future Circular Collider Experiments*, *Proceedings of Science* **476** (2025), 1104. Scopus EID: 2-s2.0-105004801889.

B. Monographs and Technical Reports

7. Altmann, J., Skands, P., Desai, A., Mitaroff, W., Plätzer, S., Dobur, D., Skovpen, K., Drewes, M., Durieux, G., Georis, Y., et al., *ECFA Higgs, Electroweak, and Top Factory Study*, *CERN Yellow Reports: Monographs* **5** (2025), ISBN 978-92-9083-700-8, eISBN 978-92-9083-701-5, DOI: 10.23731/CYRM-2025-005. Author list includes Francesco Massimiliano Procacci.

8. IDEA Study Group, *The IDEA Detector Concept for FCC-ee*, FERMILAB-PUB-25-0189-PPD (2025), DOI: 10.48550/arXiv.2502.21223. Author list includes Francesco Massimiliano Procacci.

9. CEPC Study Group, *CEPC Technical Design Report - Reference Detector*, Technical Design Report, IHEP-CEPC-DR-2025-01 and IHEP-EP-2025-01, Institute of High Energy Physics (2025). Author list includes Francesco Massimiliano Procacci.

C. Submitted Manuscripts (not related to the PhD thesis work)

10. CMS Collaboration, *Search for a New Resonance Decaying to a Higgs Boson and a Scalar Boson in Events with Two b Jets and Two Z Bosons in Proton-Proton Collisions at* $\sqrt{s} = 13$ *TeV*, CMS-B2G-24-022, CERN-EP-2026-020, submitted to *Physical Review D* (2026). Author list includes Francesco Massimiliano Procacci.

11. CMS Collaboration, *Observation of the Jet Diffusion Wake Using Dijets in Heavy Ion Collisions*, CMS-HIN-25-012, CERN-EP-2026-017, submitted to *Physical Review Letters* (2026). Author list includes Francesco Massimiliano Procacci.

12. CMS Collaboration, *System-Size Dependence of Charged-Particle Suppression in Ultrarelativistic Nucleus-Nucleus Collisions*, CMS-HIN-25-014, CERN-EP-2026-032, submitted to *Physics Letters B* (2026). Author list includes Francesco Massimiliano Procacci.

Bibliography

[1] A. Mazumdar, "The origin of dark matter, matter-anti-matter asymmetry, and inflation," *arXiv preprint arXiv:1106.5408*, 2011.

[2] S. F. King, A. Merle, S. Morisi, Y. Shimizu, and M. Tanimoto, "Neutrino mass and mixing: From theory to experiment," *New Journal of Physics*, vol. 16, no. 4, p. 045 018, 2014.

[3] J. Ellis, "Outstanding questions: Physics beyond the standard model," *Philosophical Transactions of the Royal Society A: Mathematical, Physical and Engineering Sciences*, vol. 370, no. 1961, pp. 818–830, 2012.

[4] A. Abada, M. Abbrescia, H. Abdolmaleki, et al., "Future Circular Collider Feasibility Study Report Volume 2," *Eur. Phys. J. Spec. Top.*, vol. 234, no. 19, pp. 5713–6197, 2025. DOI: 10.17181/CERN.EBAY.7W4X. arXiv: 2505.00274. [Online]. Available: https://cds.cern.ch/record/2928793.

[5] J. Gao, "Cepc project status," *arXiv preprint arXiv:2505.04663*, 2025.

[6] I. Agapov et al., "Future circular lepton collider fcc-ee: Overview and status," *arXiv preprint arXiv:2203.08310*, 2022.

[7] Y. Li and J. Gao, "Cepc accelerator status overview," *Journal of Instrumentation*, vol. 19, no. 02, T02009, 2024.

[8] I. S. Group et al., "The idea detector concept for fcc-ee," *arXiv preprint arXiv:2502.21223*, 2025.

[9] T. C. S. Group, *Cepc technical design report – reference detector*, 2025. arXiv: 2510.05260 [hep-ex]. [Online]. Available: https://arxiv.org/abs/2510.05260.

[10] M. Antonello, "Italian physical society: Idea: A detector concept for future leptonic colliders," *Nuovo Cimento C*, vol. 43, p. 27, 2020.

[11] M. T. Lucchini et al., "New perspectives on segmented crystal calorimeters for future colliders," *Journal of Instrumentation*, vol. 15, no. 11, P11005–P11005, 2020.

[12] M. T. Lucchini, L. Pezzotti, G. Polesello, and C. G. Tully, "Particle flow with a hybrid segmented crystal and fiber dual-readout calorimeter," *Journal of Instrumentation*, vol. 17, no. 06, P06008, 2022.

[13] S. Braibant and P. Giacomelli, "Muon detection at fcc-ee," *The European Physical Journal Plus*, vol. 136, no. 11, p. 1143, 2021.

[14] W. Elmetenawee et al., "The tracking performance for the idea drift chamber," *arXiv preprint arXiv:2211.12568*, 2022.

[15] W. Elmetenawee et al., "Enhancing particle identification in helium-based drift chambers using cluster counting: Insights from beam test studies," *Journal of Instrumentation*, vol. 20, no. 11, P11019, 2025.

[16] G. Chiarello, F. Cuna, B. D'Anzi, et al., "Implementation of the cluster counting and timing technique on fpga for the reduction of transferred data and stored information," *Nucl. Instrum. Meth. A*, vol. 1046, p. 167 734, 2023. DOI: 10.1016/j.nima.2022.167734.

[17] P. D. Group et al., "Review of particle physics," *Progress of theoretical and experimental physics*, vol. 2022, no. 8, p. 083C01, 2022.

[18] G. F. Knoll, *Radiation detection and measurement*. John Wiley & Sons, 2010.

[19] W. Blum, W. Riegler, and L. Rolandi, *Particle detection with drift chambers*. Springer Science & Business Media, 2008.

[20] J. H. Parker Jr and J. J. Lowke, "Theory of electron diffusion parallel to electric fields. i. theory," *Physical Review*, vol. 181, no. 1, p. 290, 1969.

[21] G. Charpak and F. Sauli, "Multiwire proportional chambers and drift chambers," *Nuclear Instruments and Methods*, vol. 162, no. 1-3, pp. 405–428, 1979.

[22] F. Sauli, "Principles of operation of multiwire proportional and drift chambers," CERN, Tech. Rep. CERN-77-09, 1977.

[23] M. Adinolfi et al., "The kloe drift chamber," *Nuclear Instruments and Methods in Physics Research Section A: Accelerators, Spectrometers, Detectors and Associated Equipment*, vol. 461, no. 1-3, pp. 25–28, 2001.

[24] A. Baldini et al., "Performances of a new generation tracking detector: The meg ii cylindrical drift chamber," *The European Physical Journal C*, vol. 84, no. 5, p. 473, 2024.

[25] K. Afanaciev et al., "A search for $\mu+\rightarrow$ e+ γ with the first dataset of the meg ii experiment," *The European Physical Journal C*, vol. 84, no. 3, p. 216, 2024.

[26] C. Caputo et al., "Particle identification with the cluster counting technique for the idea drift chamber," *Nuclear Instruments and Methods in Physics Research Section A: Accelerators, Spectrometers, Detectors and Associated Equipment*, vol. 1048, p. 167 969, 2023.

[27] Z. Drasal and W. Riegler, "An extension of the gluckstern formulae for multiple scattering: Analytic expressions for track parameter resolution using optimum weights," *Nuclear Instruments and Methods in Physics Research Section A: Accelerators, Spectrometers, Detectors and Associated Equipment*, vol. 910, pp. 127–132, 2018.

[28] F. Sauli, *Gaseous radiation detectors: fundamentals and applications*. Cambridge University Press, 2015.

[29] G. F. Tassielli and I. Collaboration, "A proposal of a drift chamber for the idea detector concept for a future e+e- collider," *PoS*, vol. ICHEP2020, p. 877, 2021. DOI: 10.22323/1.390.0877.

[30] G. Chiarello et al., "The construction technique of the high granularity and high transparency drift chamber of meg ii," *JINST*, vol. 12, p. C07022, 2017. DOI: 10.1088/1748-0221/12/07/C07022.

[31] A. M. Baldini et al., "The design of the meg ii experiment," *Eur. Phys. J. C*, vol. 78, p. 380, 2018. DOI: 10.1140/epjc/s10052-018-5845-6.

[32] Ansys, Inc., *Acp user's guide, release 2025 r1*, Ansys Composite PrepPost documentation, 2025.

[33] Ansys, Inc., *Ansys composite preppost (acp) for developers*, Official Ansys developer documentation, 2025.

[34] M. Dong, *R&D Progress of Drift Chamber for CEPC*, Slides presented at the 2024 European Edition of the International Workshop on the Circular Electron-Positron Collider, Accessed: 2026-03-07, Marseille, France, Apr. 2024. [Online]. Available: https://indico.in2p3.fr/event/20053/contributions/137839/attachments/83978/125152/R&D%20Progress%20of%20drift%20chamber%20for%20CEPC.pdf.

[35] W. Fang et al., "Refined drift chamber simulation in the cepc experiment," in *EPJ Web of Conferences*, EDP Sciences, vol. 295, 2024, p. 03 034.

[36] M. Dong, *Drift chamber with cluster counting technique for cepc*, Talk at ICHEP 2024, Prague, Czech Republic, Parallel session talk, "Detectors for Future Facilities, R&D, Novel Techniques". Indico contribution by Mingyi Dong (Institute of High Energy Physics, Chinese Academy of Sciences), Jul. 2024. [Online]. Available: https://indico.cern.ch/event/1291157/contributions/5892394/attachments/2900114/5085562/Drift%20chamber%20with%20cluster%20counting%20technique%20for%20CEPC.pdf.

[37] W. Pan et al., *Study of primary ionization counting method in drift chamber*, Talk presented at the 2025 International Workshop on the High Energy Circular Electron Positron Collider, Presentation, 6–10 November 2025, Guangzhou, China, Nov. 2025.

[38] A. M. Baldini et al., "Detailed analysis of chemical corrosion of ultra-thin wires used in drift chamber detectors," 2021, arXiv:2108.13948.

[39] ASTM International, *ASTM D3379 – standard test method for tensile strength and young's modulus for high-modulus single-filament materials*, Reapproved 1989; ASTM International, 1975.

[40] I.-L. Velicu et al., "Energy-enhanced deposition of copper thin films by bipolar high power impulse magnetron sputtering," *Surface and Coatings Technology*, vol. 359, pp. 97–107, 2019.

[41] G. Charles et al., "Carbon wire chamber at sub-atmospheric pressure," *Nuclear Instruments and Methods in Physics Research Section A: Accelerators, Spectrometers, Detectors and Associated Equipment*, vol. 855, pp. 154–158, 2017.

[42] C. Barile, C. Casavola, and F. De Cillis, "Mechanical comparison of new composite materials for aerospace applications," *Composites Part B: Engineering*, vol. 162, pp. 122–128, 2019.

[43] C. U. Grosse, M. Ohtsu, D. G. Aggelis, and T. Shiotani, *Acoustic emission testing: Basics for research–applications in engineering*. Springer Nature, 2021.

[44] D. Balageas, C.-P. Fritzen, and A. Güemes, *Structural health monitoring*. John Wiley & Sons, 2010, vol. 90.

[45] M. G. Sause, "Investigation of pencil-lead breaks as acoustic emission sources," 2011.

[46] B. G. Lopes, F. A. Alexandre, W. N. Lopes, P. R. de Aguiar, E. C. Bianchi, and M. A. A. Viera, "Study on the effect of the temperature in acoustic emission sensor by the pencil lead break test," in *2018 13th IEEE International Conference on Industry Applications (INDUSCON)*, Ieee, 2018, pp. 1226–1229.

[47] A. Vary, "Acousto-ultrasonic characterization of fiber reinforced composites," in *Office of Naval Res. Conf. A Critical Rev: Tech. for the Characterization of Composite Mater.*, 1981.

[48] W. H. Prosser, "Advanced ae techniques in composite materials research," *Journal of Acoustic Emission*, vol. 14, no. 3-4, 1996.

[49] N. Saha, P. Roy, and P. Topdar, "Damage detection in composites using non-destructive testing aided by ann technique: A review," *Journal of Thermoplastic Composite Materials*, vol. 36, no. 12, pp. 4997–5033, 2023.

[50] *Plastics – methods of exposure to laboratory light sources*, ISO 4892-3, 2016.

[51] *Standard practice for operating fluorescent uv lamp apparatus*, ASTM G154, 2020.

[52] N. Sazali, H. Ibrahim, A. Jamaludin, M. Mohamed, W. Salleh, and M. Abidin, "Degradation and stability of polymer: A mini review," in *IOP Conference Series: Materials Science and Engineering*, IOP Publishing, vol. 788, 2020, p. 012 048.

[53] P. Rehak and A. Walenta, "Relativistic rise measurement by cluster counting method in time expansion chamber," *IEEE Transactions on Nuclear Science*, vol. 27, no. 1, pp. 54–58, 2007.

[54] G. Cataldi, F. Grancagnolo, and S. Spagnolo, "Cluster counting in helium based gas mixtures," *Nuclear Instruments and Methods in Physics Research Section A: Accelerators, Spectrometers, Detectors and Associated Equipment*, vol. 386, no. 2-3, pp. 458–469, 1997.

[55] C. Lippmann, "Particle identification," *Nuclear Instruments and Methods in Physics Research Section A: Accelerators, Spectrometers, Detectors and Associated Equipment*, vol. 666, pp. 148–172, 2012.

[56] F. Cuna, N. De Filippis, F. Grancagnolo, and G. F. Tassielli, "Simulation of particle identification with the cluster counting technique," *arXiv preprint arXiv:2105.07064*, 2021.

[57] L. Cerrito, M. Gatta, L. Paoluzi, and E. Santovetti, "Particle identification using cluster counting in a large drift chamber at normal conditions," *Nuclear Instruments and Methods in Physics Research Section A: Accelerators, Spectrometers, Detectors and Associated Equipment*, vol. 434, no. 2-3, pp. 261–270, 1999.

[58] I. Lehraus, R. Matthewson, and W. Tejessy, "Particle identification by de/dx sampling in high pressure drift detectors," *Nuclear Instruments and Methods in Physics Research*, vol. 196, no. 2-3, pp. 361–379, 1982.